Surface Science Reports 72 (2017) 1–58

Contents lists available at ScienceDirect

Surface Science Reports

journal homepage: www.elsevier.com/locate/surfrep

Nanoparticle decoration with surfactants: Molecular interactions, assembly, and applications

Hendrik Heinz [a,*], Chandrani Pramanik [a], Ozge Heinz [b], Yifu Ding [b], Ratan K. Mishra [c], Delphine Marchon [c], Robert J. Flatt [c], Irina Estrela-Lopis [e], Jordi Llop [f], Sergio Moya [f], Ronald F. Ziolo [a,d]

[a] Department of Chemical and Biological Engineering, University of Colorado at Boulder, Boulder, CO 80309, USA
[b] Department of Mechanical Engineering, University of Colorado at Boulder, Boulder, CO 80309, USA
[c] Department of Civil, Environmental and Geomatic Engineering, ETH Zurich, CH-8093 Zürich, Switzerland
[d] Centro de Investigación en Química Aplicada (CIQA), Department of Advanced Materials, 25294 Saltillo, Coahuila, Mexico
[e] Institute for Physics and Biophysics, University of Leipzig, D-04107 Leipzig, Germany
[f] Centro de Investigación Cooperativa en Biomateriales (CIC BiomaGUNE), 20009 Donostia-San Sebastián, Guipúzcoa, Spain

ARTICLE INFO

Article history:
Received 27 September 2016
Received in revised form
2 January 2017
Accepted 11 January 2017
Available online 15 February 2017

Keywords:
Nanoparticles
Surfactants
Biological ligands
Self-assembled monolayers
Polymers
Oxides
Layered materials
Cement

ABSTRACT

Nanostructures of diverse chemical nature are used as biomarkers, therapeutics, catalysts, and structural reinforcements. The decoration with surfactants has a long history and is essential to introduce specific functions. The definition of surfactants in this review is very broad, following its lexical meaning "surface active agents", and therefore includes traditional alkyl modifiers, biological ligands, polymers, and other surface active molecules. The review systematically covers covalent and non-covalent interactions of such surfactants with various types of nanomaterials, including metals, oxides, layered materials, and polymers as well as their applications. The major themes are (i) molecular recognition and noncovalent assembly mechanisms of surfactants on the nanoparticle and nanocrystal surfaces, (ii) covalent grafting techniques and multi-step surface modification, (iii) dispersion properties and surface reactions, (iv) the use of surfactants to influence crystal growth, as well as (v) the incorporation of biorecognition and other material-targeting functionality. For the diverse materials classes, similarities and differences in surfactant assembly, function, as well as materials performance in specific applications are described in a comparative way. Major factors that lead to differentiation are the surface energy, surface chemistry and pH sensitivity, as well as the degree of surface regularity and defects in the nanoparticle cores and in the surfactant shell. The review covers a broad range of surface modifications and applications in biological recognition and therapeutics, sensors, nanomaterials for catalysis, energy conversion and storage, the dispersion properties of nanoparticles in structural composites and cement, as well as purification systems and classical detergents. Design principles for surfactants to optimize the performance of specific nanostructures are discussed. The review concludes with challenges and opportunities.

Contents

1. Introduction . . . 2
1.1. Definitions . . . 3
1.2. Historical perspective . . . 3
1.2.1. Detergents . . . 3
1.2.2. Water purification and chromatography . . . 3
1.2.3. Soil and the surface modification of clay minerals . . . 4
1.2.4. Self-assembled monolayers and functionalized nanoparticles . . . 4

* Corresponding author.
E-mail address: hendrik.heinz@colorado.edu (H. Heinz).

http://dx.doi.org/10.1016/j.surfrep.2017.02.001

1.2.5. In-vivo interaction of nanostructures with surfactants and cells . . . 4
1.3. Outline of this review . . . 4
1.3.1. Systems and aims . . . 4
1.3.2. Organization . . . 5
2. General concepts of nanoparticle decoration with surfactants . . . 5
2.1. Early studies . . . 5
2.2. Structure, tilt angle, and thermal properties of surfactant layers . . . 5
2.3. Influence of nanoparticle curvature . . . 6
2.4. Rigid surfactants for particle ordering . . . 7
2.5. Grafting mechanisms . . . 8
2.6. Colloidal stability and dispersion . . . 9
2.7. Imaging, tracking, and dosimetry of nanoparticles . . . 10
2.8. Enthalpy versus entropy of surfactant adsorption . . . 11
3. Modification of metallic nanostructures with surfactants . . . 13
3.1. Noncovalent binding of ligands via soft epitaxy . . . 13
3.2. Relationship between facet-specific ligand binding and nanocrystal growth . . . 15
3.3. Nanoparticle superlattices from densely grafted rigid thiol surfactants . . . 16
3.4. Applications in catalysis . . . 16
3.5. Applications in diagnostics and therapeutics . . . 19
4. Modification of oxide and chalcogenide nanostructures with surfactants . . . 19
4.1. Surface chemistry and noncovalent binding mechanisms of surfactants . . . 19
4.1.1. Surface chemistry . . . 19
4.1.2. Noncovalent binding mechanisms of surfactants . . . 21
4.2. pH-specific contributions to ligand adsorption . . . 22
4.3. Covalent modification of oxide surfaces . . . 23
4.4. Surfactant-directed growth of oxide nanoparticles, nanowires, and porous nanostructures . . . 26
4.5. Optical and electronic properties of surfactant-modified oxide nanoparticles, quantum dots, and applications . . . 27
4.6. Applications as therapeutics and diagnostics . . . 29
5. Surface modification of 2D layered nanostructures . . . 31
5.1. Graphene-based nanomaterials . . . 31
5.2. Transition metal chalcogenides . . . 33
5.3. Layered transition metal oxides . . . 34
5.4. Clay minerals . . . 35
5.4.1. Ion exchange, structure and dynamics of alkyl-modified clay minerals . . . 35
5.4.2. Cohesion between layers . . . 38
5.4.3. Dispersion in a host matrix . . . 39
5.5. Layered double hydroxides and applications . . . 39
6. Surface modification of cement minerals and other inorganic nanostructures . . . 41
6.1. Nanoparticle-organic interfaces in cementitious materials . . . 41
6.1.1. Polymer effects on the nanostructure of calcium silicate hydrates . . . 42
6.1.2. Modification of the formation of calcium sulfo-aluminates . . . 42
6.1.3. Polymeric dispersants at the cement-water interface . . . 43
6.1.4. Molecular modelling of interfacial properties . . . 43
6.2. Other inorganic nanostructures . . . 44
7. Modification of polymer nanoparticles with surfactants . . . 46
7.1. Surface modification of polymer nanoparticles for drug delivery . . . 46
7.1.1. Types of polymers, particle size, shape, and cell targeting properties . . . 46
7.1.2. Tuning surface properties by surfactants . . . 49
7.1.3. Release mechanism of drugs . . . 49
7.1.4. Synthesis and assembly for specific surface properties . . . 50
7.1.5. Surfactant modification and blood brain barrier . . . 51
7.2. Polymeric nanoparticles in protective coatings . . . 52
8. Summary, challenges, and opportunities . . . 53
Acknowledgements . . . 53
References . . . 53

1. Introduction

Nanomaterials with specific surface functionality are ubiquitous in nature. Soils, seashells, bone, and teeth contain inorganic/organic nanostructures [1–3]. Small cells like mycoplasma (~200 nm) and cell organelles can be regarded, according to size, as living polymeric nanoparticles [4]. The term surfactant-decorated nanoparticles, as used in the chemical sciences and in this review, is typically associated with manmade nanostructures for applications in imaging, drug delivery, composites, catalysis, energy conversion devices, purification systems, and other technologies (Fig. 1) [5,6]. The terminology "surfactant" is used here for a broad array of surface active agents, according to its true definition (see Section 1.1), and includes classic alkyl-based surfactants, peptides, lipids, DNA, molecular ligands, bioconjugates, and polymers covalently grafted to or non-covalently assembled on nanomaterial surfaces, thereby changing their properties. The term nanoparticles encompasses a broad range of nanostructures of different chemical composition, shape, and size in the 1–1000 nm range. Details of the definitions, a historical perspective, and a full outline of this review follow in the subsections below. The main part of the review consists of general concepts in Section 2, the discussion

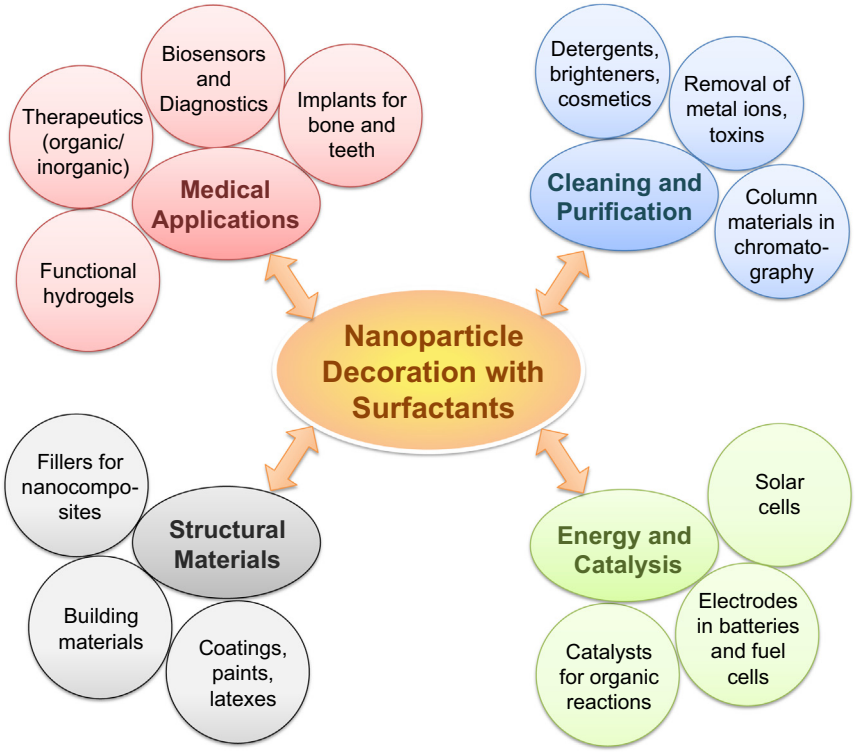

Fig. 1. Applications of surface-modified nanoparticles and, more broadly, nanostructures. Functional nanoparticle-surfactant combinations are involved in medical applications, structural materials, energy conversion processes, catalysts, as well as in cleaning and purification systems.

of different types of nanoparticles modified with surfactants in Sections 3–7, and a summary in Section 8.

1.1. Definitions

The origin of surfactants dates back to man-made products from plant oils and animal fat such as soap and detergents that have been used for millennia as cleaning, hygiene, and foaming agents [7]. Surfactants often lower the interfacial tension between two or more components in a material system, thereby increasing miscibility, colloidal stability, dispersion, and enabling a wider property portfolio of the multicomponent material. The word "surfactant" was coined in the 1940s and is a lexeme derived from the words "surface active agent (-ant)" [8,9]. The term "surfactant"="surface active agent" is used as an umbrella term in this review for all types of surface modifiers, far beyond detergents (cleaning agents). It covers compounds that alter the compatibility (miscibility) between otherwise incompatible phases, such as the classic water and oil example, between nanoparticles and polymers, nanoparticles and analytes. Surface-modifying compounds that control the association of nanoparticles, cell targeting properties, catalytic activity, charge transfer, and other surface-related properties are also termed "surfactants" in this extended definition, and common terms such as "detergents", "ligands", "molecular linkers", and "surface modifiers" can be used as appropriate for the given examples. The range of surfactants therefore encompasses classic alkyl-based surfactants, peptides, lipids, DNA, polymers, molecular ligands, and bioconjugates that modify surface properties. The terms "ligands" and "surface modifiers" will also be used in parallel with "surfactant", as is common in the literature. The authors understand that the use and development of terminology in current research areas may depend on individual preferences and is a dynamic process.

Nanoparticles are defined as solid compounds of any chemical composition, shape, and size in the range 1–1000 nm.

1.2. Historical perspective

1.2.1. Detergents

Without knowing chemical details, detergents have been used to remove stains in clothing for millennia. Soap-like materials with preparation instructions were found in Babylon dating back to 2800 BCE [7]. Stains often consist of clay minerals and organic matter adsorbed onto cellulosic fibers. Mechanical agitation of the textile fibers containing the adsorbed clay platelets and organic material from soil, aided by competitive binding of detergents to the clay surface and encapsulating organic stains, assists in detachment and stain removal. The result are clean clothes and suds consisting of a solution of dispersed clay particles and organic stains.

1.2.2. Water purification and chromatography

Without knowing chemical details, certain types of wood and charcoal have been used for thousands of years to remove harmful bacteria and metal ions from natural water sources, or to improve taste [10,11]. In this process, cellulosic nanostructures, or polyphenols in the wood, retain bacteria, form complexes with metal ions and adsorb organic compounds. Water purification today relies on ion exchange on nanoparticles and membranes that can be surface-modified to enhance performance.

Similar concepts are at work in chromatography and column materials to separate mixtures, reaction products, and polymers [12,13]. Silica gels, for example, have become a standard column material and consist of nanoparticles of customized size, porosity, and surface modification. The nanoparticles interact selectively with organic molecules depending on molecular size, pH, and chemistry, leading to fractionation and different retention times [12,14,15]. Apatites and other bioinspired solid phases have also been employed in the separation of proteins and virions [13,16,17].

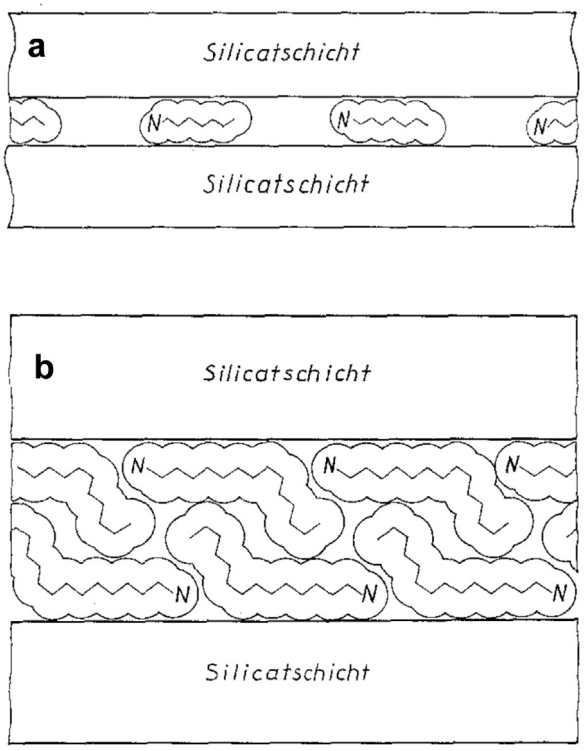

Fig. 2. Alkylammonium surfactants between layered silicates of low cation exchange capacity. (a) Short chain length. (b) Longer chain length. Pseudo-multilayers and molecular "kinks" (gauche conformations) can be seen. Thermal transitions at higher surface coverage can arise from rotations and translations of kinks and chains. (Adapted with permission from [25].)

1.2.3. Soil and the surface modification of clay minerals

Soil is made of natural nanostructures with surface modifications, especially soils rich in clay and carbonate minerals. The minerals are the final products of weathering of rocks and contain exchangeable ions on their surface that aid in the adsorption of humic substances and nutrients for plants [18–20]. Adsorption-desorption equilibria and surface reactions at the inorganic-organic interfaces play a major role for the function of the ecosystem. Early systematic investigations of nanoparticle decoration with surfactants about a century ago involved the compositional analysis, ion exchange, and organic surface modification of clay minerals, graphite, quartz, and other readily available compounds, aided by advances in microscopy, imaging, and spectroscopy [21,22]. Improvements in X-ray methods for increasingly precise structure determinations over the next few decades lead to insight into elemental compositions, stoichiometry, and surfactant assembly [23–28]. First models of alkylammonium surfactant conformations in interlayer spaces consistent with X-ray data were proposed in the 1950s (Fig. 2) [25,29–31]. At the same time, theories of solid-liquid phase transitions of surfactants and polymers attached to nanoparticles were developed [27,32,33]. The models explain the positioning and approximate tilt angle of the surfactants in near-atomic resolution. The details and rigor of the analyses and theoretical models continue to be state of the art from today's viewpoint of near-atomically resolving instrumentation [27,32–34]. In the late 1980s, similar systems of alkyl surfactants grafted to metals were termed "self-assembled monolayers" (SAMs) [35,36]. Similarities and differences of alkyl thiols grafted to metals with self-assembled monolayers on clay minerals will be described in Section 2.

1.2.4. Self-assembled monolayers and functionalized nanoparticles

Current capabilities of high resolution imaging and detection techniques (TEM, AFM, SEM, electron tomography, neutron reflectometry and scattering), advanced spectroscopy (IR, SFG, XPS, multidimensional NMR), and computer simulations have greatly expanded the toolkit to understand interfacial properties and assembly in near-atomic resolution [37–48]. Specific conformational changes in surfactants, the amount of gauche versus anti-conformations, cohesive energies, and dispersion properties in polymers have been studied. Thiol modification of metal and alloy nanostructures, including functionalization with a wide range of ligands, layer-by-layer assembly protocols, and bioconjugation have become widely accepted techniques in nanoscience [49–52]. In addition, polymer-based nanoparticles are broadly used for drug delivery, paints, and anti-corrosion coatings [53–55].

1.2.5. In-vivo interaction of nanostructures with surfactants and cells

Decoration of nanostructures with surfactants and nanoparticle-matrix interactions are also omnipresent in-vivo. Bone, teeth, and calcium mineral deposits in arteries consist of inorganic nanocrystals in contact with structural and functional proteins, lipids, and other components in cellular and extracellular fluids [56–60]. The assembly and function of these interfaces, as well as control over associated diseases remains yet hardly understood and is perhaps one of the greatest challenges in nanobioscience [3,61–64]. Cell organelles and some cell types below micrometer size can also be considered as complex living nanoparticles.

In-vivo roles of surface modified nanoparticles include also a broad range of diagnostics and therapeutics, such as nanoparticles composed of silica, iron oxide, polymers, such as polylactic-co-glycolic acid (PLGA), and core-shell nanoparticles for drug delivery. The nanostructures are filled with active molecules for controlled release and surface-modified with cell-targeting ligands that can be critical for the performance [53,65–67]. An increasing branch of recent research is also the study of the toxicity of nanoparticles including encapsulation and cellular uptake mechanisms [52,68,69].

1.3. Outline of this review

This review covers nanoparticle interactions with surfactants, focusing on molecular interactions, assembly, and a broad range of applications (Fig. 1). The relationships between the surface chemistry of the nanostructures, binding and grafting mechanisms of the surfactants, interfacial properties, and function of the nanostructures are emphasized.

1.3.1. Systems and aims

Commonly used surfactants and ligands include alkylammonium halides such as cetyl trimethylammonium bromide (CTAB, n-$C_{16}H_{33}$–$N(CH_3)_3^+$ Br^-), sodium dodecyl sulfate (SDS, n-$C_{12}H_{25}$–OSO_3^- Na^+) [70,71], and lipid-derived compounds (stearic acid, linoleic acid, and linolenic acid). Many surfactants, like the examples above, are amphiphiles with hydrophilic and hydrophobic groups [72]. Ligands, which are also considered surfactants in this review (the ones less similar to detergents), also comprise alkane thiols bound to metal and sulfide nanoparticles, peptides, DNA, tailor-made synthetic molecules, surface-adsorbed buffers, block copolymers, and other additives modifying interfacial behavior. The surfactants may exhibit selective binding to metals, alloys, oxides, sulfides, silicates, layered minerals, or polymeric nanoparticles [73–76], often as a function of (h k l) crystal facet and monomer sequence (e.g. in peptide and polymer surfactants).

Selectively protected metal and alloy nanostructures have found broad application in sensors, catalysts, and electrode materials for batteries and fuel cells, as well as for cell targeting therapeutics [49,77–81]. Ligand binding to oxides, sulfides, layered materials, and other inorganic nanostructures enables similar

applications in medicine, structural materials, optical, and electronic devices [82–84]. Understanding the surface modification of nanoparticles and nanostructures therefore plays a major role to advance diverse applications from therapeutics to advanced energy conversion materials, automotive and aerospace parts, building materials, commodities, catalysts, and electronics. Therefore, this review also aims to bridge understanding across different scientific communities and explain less connected topics from a uniform perspective. Exciting recent advances in imaging and spectroscopy in near-atomic resolution, in combination with powerful computational tools, are also included in this review as they have the potential to facilitate breakthrough discoveries of functional nanostructures [77,85–89].

1.3.2. Organization

General principles of nanoparticle-surfactant structure and dynamics are laid out in Section 2. Sections 3–7 focus on the relationship between nanoparticle decoration with surfactants and achieving specific materials properties, taking into account specific surface chemistry, surfactant assembly, and explaining parameters for functionality and performance. In more detail, in Section 2, we explain conceptual models of surfactant assembly that have emerged in various areas of nanoparticle modification and assembly. Criteria to predict surfactant tilt angles, conformations, and trends in nanoparticle assembly are described. In Section 3, we discuss the surface modification and crystal growth of metal and alloy nanostructures. Section 4 details the surface modification of oxides and sulfides. Section 5 explores the surface modification of 2D materials including graphitic structures, layered transition metal chalcogenides, clay minerals, and layered double hydroxides. Section 6 describes the surface modification of cement in building materials and other inorganic nanostructures less covered in this review. Section 7 reviews the surface modification of polymeric nanoparticles with applications in drug delivery and coatings. A summary along with discussion of challenges and opportunities follows in Section 8.

2. General concepts of nanoparticle decoration with surfactants

2.1. Early studies

The study of the adsorption of gases on surfaces laid the groundwork for the understanding of surfactant adsorption on surfaces and nanoparticles. Notable experiments of gas adsorption on plane surfaces of glass, mica, and platinum date back to Irving Langmuir [90], followed by investigations of the adsorption of gases in multimolecular layers by Brunauer, Emmett, and Teller (BET) [91]. The measurement and interpretation of adsorption isotherms resulted in the BET method, which remains today's standard to determine the specific surface area of nanomaterials. The chosen materials in early studies include bulk solids and porous materials such as charcoal, oxides, and silica gel. Also mica and clay minerals were employed due to their ability to form atomically flat surfaces that extend over micrometers and possible exfoliation into nanometer-thick layers [41]. Understanding from the deposition of gases using the theory of Freundlich, Langmuir, and BET adsorption, could then be extended to surfactants, chain molecules and other, charged molecular ligands, leading to the first models of surfactant adsorption and assembly. New questions concerned the orientation of the adsorbed molecules relative to the surface, their relative orientation towards each other, and their interactions [29,30,33].

2.2. Structure, tilt angle, and thermal properties of surfactant layers

The use of atomically flat surfaces such as mica, glass, and metals helped explore the arrangement and properties of surfactants since the effects of irregular, curved, stepped, porous, and otherwise deformed nanoparticle surfaces can be largely excluded. Lagaly and Weiss, for example, proposed models for the arrangement of alkylammonium surfactants grafted to clay mineral surfaces by ion exchange in accordance with the layer spacing from

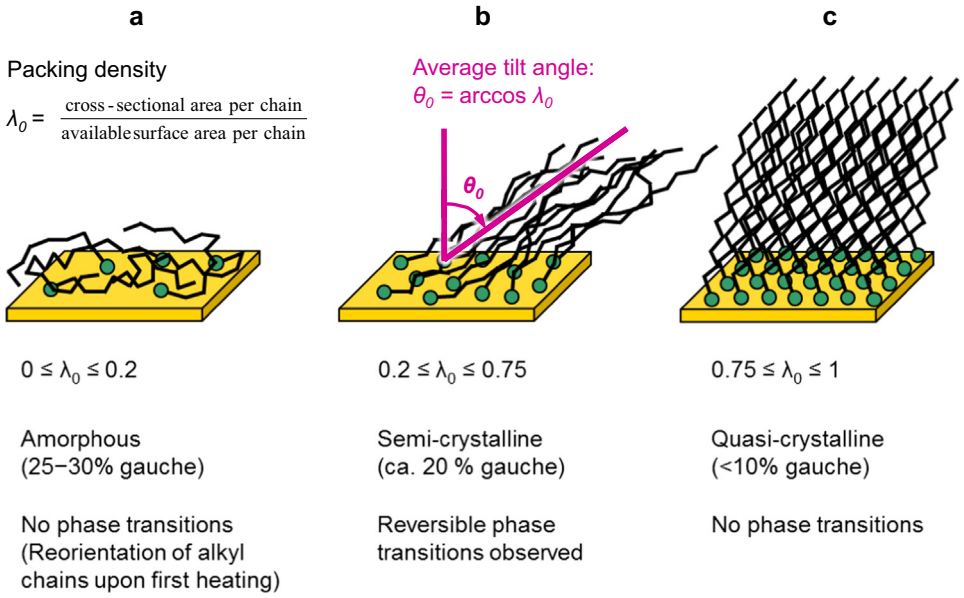

Fig. 3. Range of homogeneous alkyl layers (chain length > C_{10}) grafted to even surfaces and associated properties. (a) At low packing density ($\lambda_0 < 0.20$), alkyl chains are oriented parallel to the surface and disordered. (b) At intermediate packing density ($0.20 < \lambda_0 < 0.75$), alkyl chains are oriented with an intermediate collective tilt angle and partially ordered, able to undergo reversible melting transitions upon heating. (c) At high packing density ($\lambda_0 > 0.75$), alkyl chains are oriented upwards (up to nearly vertically) and predominantly anti configured. Significant reversible thermal transitions are only found in case (b). (Adapted with permission from Ref. [95].)

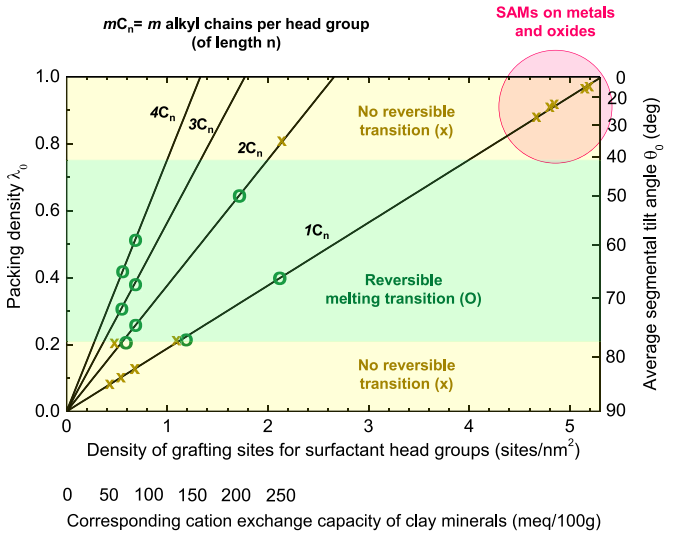

Fig. 4. Diagram showing the packing density, average segmental tilt angle, and occurrence of thermal transition for a given type of surfactant and the area density of grafting sites on the surface (one alkyl chain per head group, $m=1$; two alkyl chains per head group, $m=2$, etc.). Data on the type of surfactant and density of grafting sites are often available and allow estimates of these properties. A chain length $n > 10$ is required to observe notable tilt angles and melting transitions. In case of clay minerals (mica-type), the density of grafting sites scales directly with the effective cation exchange capacity (CEC), which is also indicated. Area densities of grafting sites on clay minerals are at the lower end (0–2 per nm^2) while grafting densities of alkyl surfactants on metal and oxide surfaces can reach the high end of 4.6–5.2 per nm^2, given that stoichiometric or excess amounts of surfactant are available during synthesis. Examples for metal and oxide surfaces include Ag, Au, Cu, Pd, Pt, TiO_2, Al_2O_3, CuO, and Ag_2O. (Adapted with permission from Ref. [95].)

X-ray data (Fig. 2) [25]. The subsequent introduction of the surface force apparatus by Israelachvili helped quantify surface forces between organically modified mineral layers [92,93] and also laid the groundwork to understand driving forces of micelle formation and surfactant assembly in solution [72]. Along with advances in IR and NMR spectroscopy as well in molecular simulation [38,94], a more quantitative picture of the conformations and dynamics of alkylammonium surfactants grafted to surfaces has evolved (Fig. 3) [95]. A central role is played by the packing density of the surfactants, λ_0 , which is given by the ratio of the cross-sectional area of the surfactant chains (A_C) to the available surface area per chain, or per head group, on the substrate (A_S):

$$\lambda_0 = \frac{A_C}{A_S}. \quad (1)$$

These parameters are often known by chemical characterization. A_C corresponds to the van-der-Waals cross-sectional area of a surfactant chain, for example, $A_C = 0.188$ nm^2 for an all-anti configured alkyl chain, and the available surface area per head group A_S can be obtained from surface characterization. Knowing these parameters yields the packing density λ_0, the average segmental tilt angle θ_0 of the chains, and thermal phase transitions become predictable (Fig. 4) [95]. The tilt angle is (by convention) defined relative to the surface normal (e.g., $\theta_0 = 0°$ in vertical orientation) and given by the correlation:

$$\lambda_0 = \cos\theta_0. \quad (2)$$

In case of common alkyl surfactants grafted to surfaces such as alkylammonium ions, alkylphosphonium ions, alkane sulfonic acids, alkane carboxylic acids, and alkane thiols, reversible order-disorder can be observed in DSC upon heating between 40 and 70 °C, however, they occur only at intermediate packing density between $\lambda_0 \sim 0.20$ and $\lambda_0 \sim 0.75$. Otherwise, alkyl-type hydrocarbon surfactants are found in a liquid-like state or in solid-like state in a temperature range from 0 to 100 °C, respectively (see more details in Section 5.4) [38,39,96,97]. The use of multiple alkyl arms attached to a head group in the surfactant, for example, using trialkylammonium halides ($3C_n$, $NH^+(C_nH_{2n+1})_3$) versus monoalkylammonium halides ($1C_n$, $NH_3{}^+(C_nH_{2n+1})$) on clay minerals, allows tuning of the packing density, tilt angles, and thermal behavior of the surfactants over a range of multiples on a given substrate (Fig. 4). The same considerations are valid for self-assembled alkane thiol monolayers on metal surfaces (e.g. Ag, Au, Cu, Pd, Pt), which were discovered in the 1980s and are widely used for surface functionalization [49,98]. The thiol ligands are chemically bonded to the metal surface by coordination of the sulfur atom with epitaxial (hollow) surface sites (Au, Pd) [95]. Binding energies of the thiols to gold (111) and other facets have been reported between 4 and 60 kcal/mol by DFT calculations [99,100], with common values and experimental estimates around 20 to 60 kcal/mol [49,101]. In excess of surfactant, the packing density is typically high (0.85–0.98) and corresponds to quasi-crystalline structures (Fig. 3c). Assembly of alkanoic acids and alkane phosphates on oxide surfaces has also been reported at similarly high packing density with quasi-crystalline structures, for example, on TiO_2, Al_2O_3, CuO, and Ag_2O [36,102,103].

On gold, in particular, well-ordered dense phases with packing densities of 0.87 and tilt angles near 30° have been observed, as well as sub-stoichiometric flat-on ("striped") phases when the exchange is sub-stoichiometric (Fig. 5a and b) [49]. Island formation and striped phases upon incomplete ion exchange were also observed on clay minerals at high packing density [104,105]. In dense, well ordered structures of thiol-saturated metal surfaces and of clay minerals with multi-arm surfactants, the tilt angle θ_0 (sometimes called α) (Fig. 3b) and an additional twist angle β of the chain with respect to the plane established by the chain axis can be defined (Fig. 5c). In case of thiolates on gold, it was found that $\theta_0 = 28 \pm 2°$ and $\beta = 53 \pm 2°$ [36,106]. Typical experimental techniques to determine the conformation and thermal behavior of surfactant chains include X-ray diffraction, IR and Raman spectroscopy, NMR spectroscopy, sum frequency generation (SFG), near-edge X-ray adsorption fine structure (NEXAFS), low energy electron diffraction (LEED), transmission electron microscopy (TEM), differential scanning calorimetry (DSC), and thermogravimetric analysis (TGA).

2.3. Influence of nanoparticle curvature

The relationships described above refer to locally flat surfaces without significant curvature. The structure-property relationships for surfactants on flat surfaces can also be applied to nanoparticles of weak curvature. However, changes become visible for stronger curvature, i.e., when the nanoparticle diameter is less than 20 times the length of the surfactants in their extended conformation. For example, the length of a C_{18} alkylammonium ion or a C_{18} thiol is about 3 nm, and then the nanoparticle diameter ($2r$) should be at least 60 nm for curvature effects to be marginal.

When the size of the nanoparticles ($2r$) is below this threshold in comparison to the length of the extended surfactant l, particle curvature affects the packing density and the total layer thickness (Fig. 6) [95]. The packing density of the surfactant $\lambda_0(d)$ decreases further away from the surface as a function of the distance d as the surfactants gain more surface area per head group. As a result, the surfactants assume a higher tilt angle further outwards from the nanoparticle surface and the total layer thickness on the curved nanoparticle h decreases relative to a flat surface (Fig. 6a).

The contraction of the surfactant shell exceeds 5% when $l/r > 0.1$, i.e., when the particle diameter is less than 20 times the surfactant length. The conformation at the outer end of the surfactants at large distance changes toward a parallel orientation relative to the surface, unless immersion in a good solvent fills the

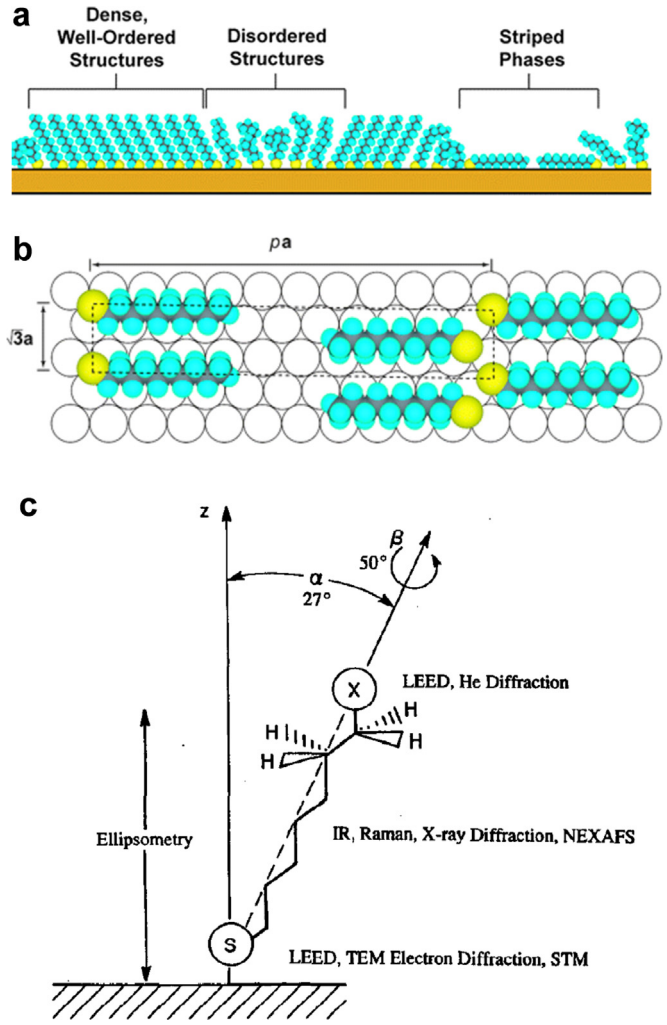

Fig. 5. Structure of thiol surfactants on gold. (a) Schematic view that illustrates the variety of structural arrangements found in SAMs prepared by microcontact printing (μCP) when the stamp is wetted with a 1–10 mM solution and applied to the substrate for 1–10 s. (b) Schematic diagram depicting a representative striped phase that can form at sub-monolayer coverage of thiol on Au(111) (a=2.88 Å). In this example, the periodicity of the rectangular unit cell (p) is 11.5. (c) Details of the possible orientation of a single, long-chain alkyl thiol molecule bound to a gold surface in side view. The tilt angle relative to the surface normal (here designated as α) as well as the twist angle β of the chain with respect to the plane established by the chain axis fully characterize the orientation of a chain in quasi-crystalline monolayers. The twist angle β is only meaningful at high packing density when chains assume almost exclusively all-anti conformations. Ellipsometry provides insight into the thickness of the molecular film. The experimental techniques listed to the right are those used to determine the structure of that portion of the molecule. (Reproduced with permission from Refs. [49,98].)

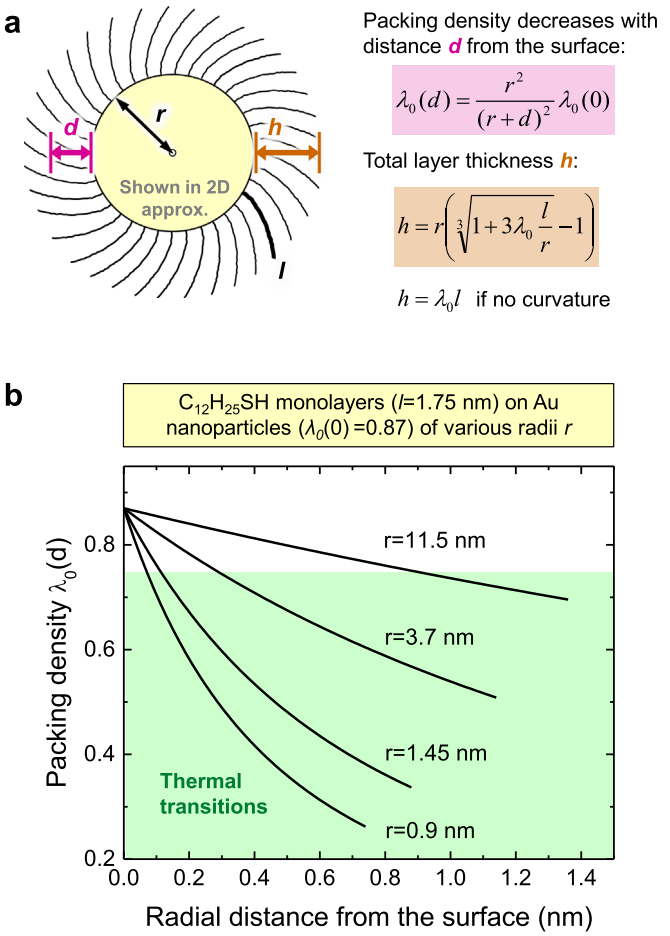

Fig. 6. Effect of particle curvature on packing density, layer thickness, and thermal transitions. (a) Schematic of ligand packing on a curved surface (nanoparticle or local curved area). The packing density decreases as a function of distance from the surface. The layer thickness is also affected, even when $l/r < 0.1$. (b) Example of the reduction of the packing density as a function of distance from the surface, reduction of the layer thickness, and of the onset of thermal transitions for dodecanethiol surfactants on gold nanoparticles of various size (green shaded area). Chain disorder and thermal transitions originate at the outer C-terminus and affect major portions of the surfactant according to IR spectroscopy, SFG, NMR spectroscopy of deuterated surfactants, and DSC data. The packing model quantitatively explains experimental observations of chain tilt angle and phase transitions, and is consistent with molecular dynamics simulations (curves follow the equations in (a)). (Fig. 6b adapted with corrections from Ref. [95].) (For interpretation of the references to color in this figure legend, the reader is referred to the web version of this article.)

extra surface area. The decrease in packing density in the outer regions of the surfactant layer leads to higher chain disorder and causes the occurrence of thermal transitions in parts of the alkyl chains, once $\lambda_0(d)$ falls below 0.75, starting at the outer C terminus (Fig. 6b). Evidence for such phase transitions excluding the region near the head group of the alkyl chains was reported for thiol-gold nanoparticles of diameters in the 1.8 nm to 25 nm range by IR, Raman, SFG, NMR, and DSC data [95,106–108].

The nanoparticle size ($2r$) required to induce notable changes in packing density $\lambda_0(d)$ and phase transitions is also about twenty times or less the surfactant length. The changes in packing density are small near the surface while the decrease in packing density is noticeable near the middle portions of and the outer ends of the surfactant layer. Very significant changes in packing density $\lambda_0(d)$ are seen when the nanoparticles are of about the same size as the surfactants, or smaller ($l/r \sim 1$) (Fig. 6b). The packing density may then drop from 0.87 near the surface to below 0.30 in the outer layer, increasing the tilt angle from 30° to over 70°. Therefore, both the packing density $\lambda_0(d)$ and the decrease in layer thickness h are strongly affected by the curvature of nanoparticles and locally curved surfaces. The equations in Fig. 6a describe the changes in packing density $\lambda_0(d)$ and layer thickness h as a function of particle radius r and surfactant length l.

2.4. Rigid surfactants for particle ordering

Rigid surfactants such as DNA or hybridized DNA enable the controlled organization of nanoparticles into superlattices (Fig. 7) [51,77,109–111]. To direct the assembly of surfactant-covered nanoparticles into regular lattices, surfactants of high stiffness at high packing density must be grafted onto the surface, and thiol-DNA conjugate ligands have been extensively tested for this purpose (Fig. 7a). It has also been necessary to hybridize the DNA

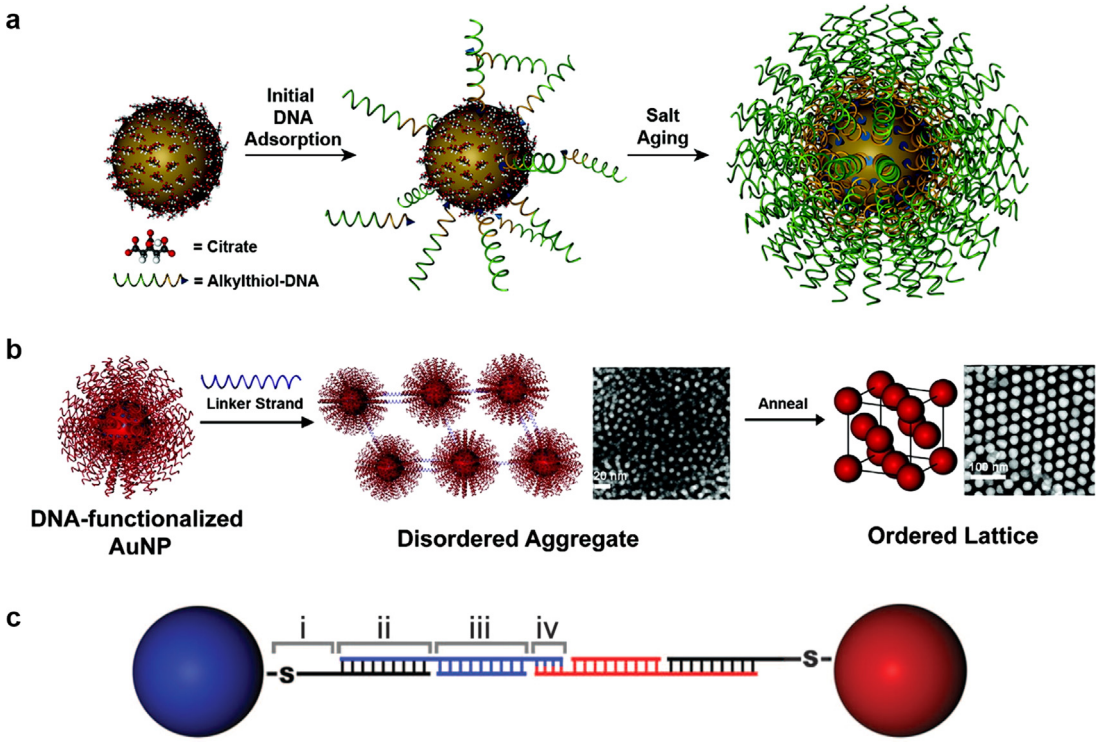

Fig. 7. Assembly of rigid thiol-DNA surfactants on gold nanoparticles and the organization of the modified nanoparticles into regular superlattices. (a) Synthesis of spherical nucleic acids-gold nanoparticle conjugates. Citrate-stabilized particles are incubated with alkylthiol-functionalized oligonucleotides in water to form a low-density monolayer. By incubating the nanoparticles in aqueous solutions with successively higher concentrations of salt (typically 0.15–1.0 M) and surfactants over ~12 h, a high-density spherical nucleic acid shell is formed. (b) Schematic illustration of DNA-programmable nanoparticle assembly into ordered superlattices (fcc lattice shown). TEM images show the transition from disordered aggregate (10 nm Au NPs depicted) to ordered lattices (30 nm Au NPs depicted) after annealing at a temperature slightly below the melting temperature of the aggregate. (c) The DNA strands that assemble the nanoparticle superlattices consist of (i) an alkylthiol moiety and 10-base nonbinding region, (ii) a recognition sequence that binds to a DNA linker, (iii) a spacer sequence of programmable length to control interparticle distances, and (iv) a "sticky end" sequence that drives nanoparticle assembly via DNA hybridization interactions. Although only a single linkage is shown schematically here, DNA-NPs typically contain tens to hundreds of DNA linkers per particle. (Adapted with permission from Refs. [110,111].)

strands and reduce the solvent concentration in the ligand shell by salting out to achieve sufficient stability of the outward-pointing DNA ligands (Fig. 7b and c). The rigidity of the DNA is then sufficiently high to control the spacing between nanoparticles and design different nanoparticle patterns based on chain length, particle size, and cooling conditions [77,112,113].

2.5. *Grafting mechanisms*

Grafting mechanisms of surfactants to nanoparticles can be divided into methods for covalent assembly and noncovalent adsorption. Covalent grafting of surfactants can be achieved in different ways. Common techniques include the attachment of surfactants with thiol end groups to metals under elimination of hydrogen, resulting in an approximate metal-sulfur bond energy of 20–60 kcal/mol (Fig. 5) [49,99,100]. Ether linkages can be introduced onto oxide and functionalized nanoparticles with terminal OH groups using silane halides and ethers, phosphonates, carboxylates, catechols, alkenes, and amines (Fig. 8a) [114,115]. Multistep functionalization of terminal OH groups (oxides, polymers) to introduce reactive amine groups and esters is also common (Fig. 8b). These methods can be combined with click chemistry to introduce a menu of functional surfactant end groups [116,117]. Combinations of covalent functionalization with subsequent layer-by-layer assembly have also been explored [50,118]. In principle, any feasible chemical reaction at the nanoparticle surface can be exploited to graft and modify surfactants.

Non-covalent adsorption mechanisms include ion exchange, ion pairing, and hydrogen bonds (Fig. 9) [12,28,119,120]. Common interactions also include soft epitaxial interactions on metal surfaces [121–123], cation-π and surfactant-π and interactions on aromatic substrates [124,125], dispersion interactions, depletion forces, and conformation effects (see following chapters) [126,127]. Ion exchange often occurs on surfaces containing acidic or basic groups and is not accompanied by changes in zeta potential. Ion pairing occurs on the same substrates and is accompanied by changes in (reduction of) the zeta potential; the two mechanisms can occur together (magnitude ~10 kcal/mol). The overall system remains typically charge neutral in the process with a shift in zeta potential while the average positions of dissolved cations and anions relative to the surface are changing. Hydrogen bonding is also a common contribution to adsorption, generally weaker compared to ion exchange, ion pairing, soft epitaxial interactions, and ion-π interactions (magnitude 1–6 kcal/mol). On specific substrates such as (non-oxidized) metals, soft epitaxial adsorption plays an important role, and involves coordination of polarizable atoms in the solutes and in the solvent with epitaxial sites on the metal surface (magnitude ~10 kcal/mol for a benzene ring) [122,123]. On substrates with π electron density, such as graphite or π-conjugated polymers, interactions of cationic groups in surfactants with π-electron clouds can make significant contributions (magnitude up to 10 kcal/mol for small ions in solution) [124,125]. Interactions are also caused by dispersion forces between individual groups in a surfactant chain (e.g. CH_2 groups) that can direct the assembly of alkyl surfactants on substrates if present in large numbers (magnitude ~0.07 kcal/mol for CH_2/CH_2 interaction) [128,129]. Depletion forces are related to disruptions in intermolecular forces between solvent molecules due to the presence of the solute. For example, the adsorption of a protein onto a noncharged and otherwise

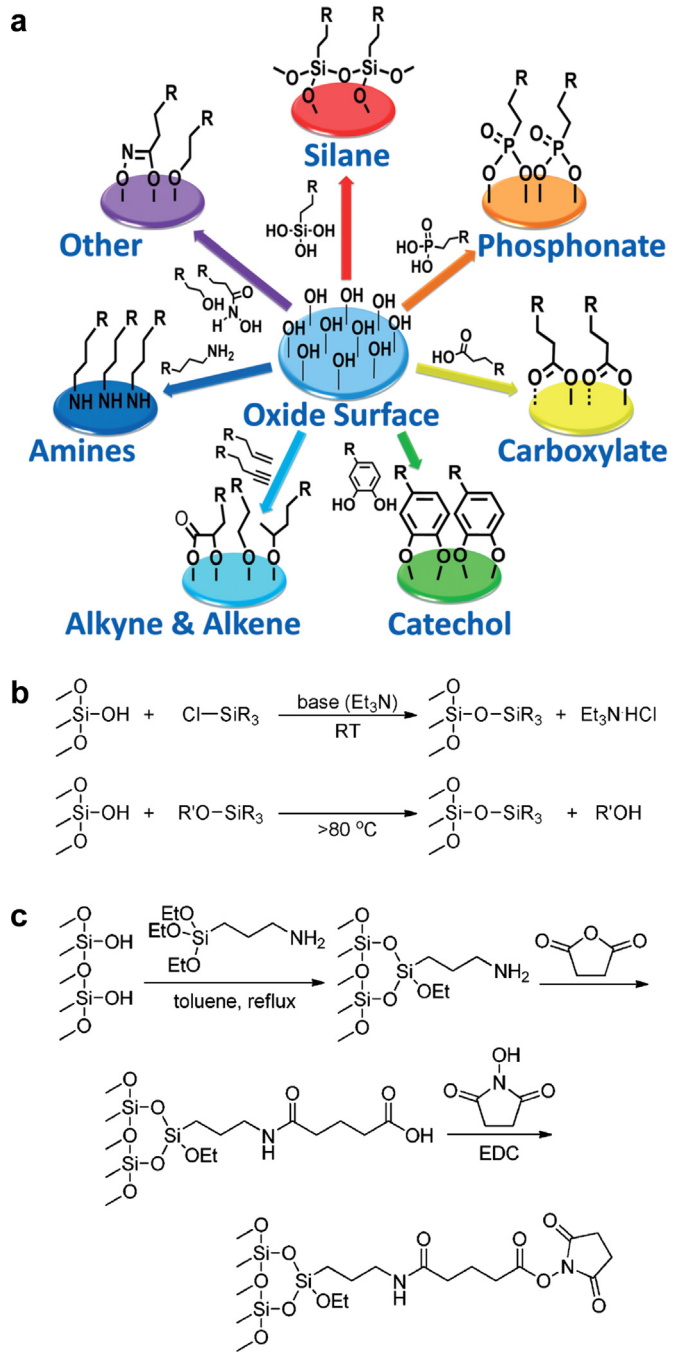

Fig. 8. Covalent grafting of surfactants to oxide surfaces. (a) Overview of methods that lead to stable monolayers. (b) Post-grafting of silane halides and silane ethers to a silica surface. (c) Post-grafting of amine, acid, and ester functionality to a silica surface (N-hydroxysuccinimide ester shown). (Reproduced with permission from Refs. [114,115].)

inert substrate may be caused by depletion forces, which eliminate disruptions in the network of hydrogen bonds in the aqueous solvent if the protein was to remain dissolved. Depletion interactions, therefore, typically involve a balance of other interactions. Moreover, conformation preferences of ligands can affect the binding strength, especially for chain molecules such as longer surfactants, proteins, and carbohydrates. It is common that several non-covalent binding mechanisms contribute to overall adsorption in a given case [130]. Individual contributions to noncovalent adsorption can be identified using existing chemical knowledge, zeta potential measurements, substitutions of

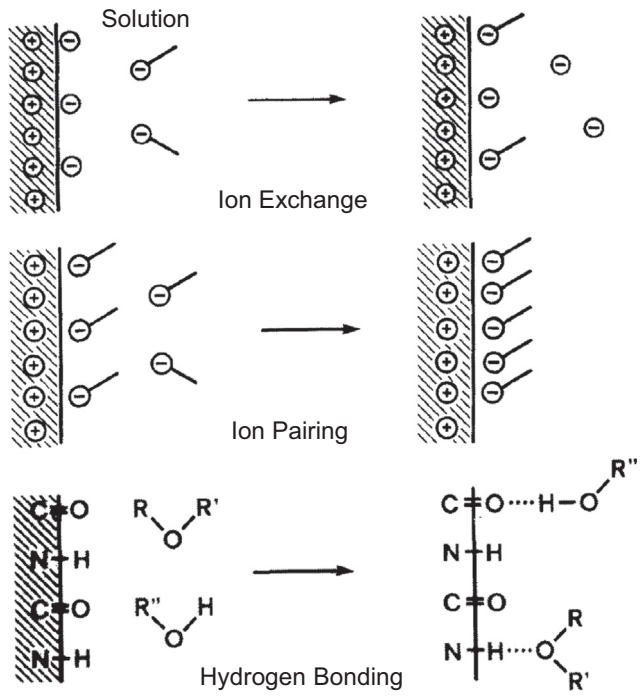

Fig. 9. Common non-covalent adsorption mechanisms of surfactants onto substrates in solution. (Adapted with permission from Ref. [119].) Other significant noncovalent interactions include cation-π interactions, soft epitaxy on metal substrates, as well as weak dispersion interactions.

functional groups in the surfactants, change of surface type and surface chemistry, use of different solvents, as well as often more quickly by molecular simulations [130].

2.6. Colloidal stability and dispersion

One of the major function provided by surfactants is colloidal stability and the ability to disperse the nanoparticles in specific solvents [131]. Metal nanoparticles form amorphous precipitates such as palladium black when no surfactants are attached [132,133], and oxide nanostructures, mineral nanoparticles, as well as quantum dots may agglomerate due to polar and ionic surface forces without surface modification (see Section 4) [131,134]. Therefore, surfactants endow the nanoparticles with specific superficial hydrophobic or hydrophilic properties, enabling the dispersion in a targeted medium such as water, alcohol, or octane. Surfactants, or modification of the outer surfactant shell in multilayer/multishell nanoparticles can also reverse the superficial polarity. Surface functionalization of hydrophobic graphene and graphitic nanostructures, for example, is essential to achieve dispersion in polar solvents and in aqueous solution (see Section 5.1) [135,136]. Vice versa, hydrophilic layered double hydroxides (LDHs) and clay minerals can be bestowed with a hydrophobic surfactant shell for dispersion in aromatic solvents and hydrophobic polymers (see Sections 5.4 and 5.5) [41,137,138]. Dispersion of hydrophobic polymer nanoparticles such as polystyrene in water can be achieved by surface functionalization with polyethylene glycol, and precipitation can be achieved by salting out (see Section 7.1) [67,139]. The stability of the colloidal nanoparticles is system-specific yet tends to be higher in comparison to traditional micelles and vesicles [72] since the solid nanoparticle cores are less affected by chemical stimuli such as changes in concentration and pH.

Beyond traditional dispersion and colloidal stability, targeting ligands can be used to direct nanoparticles to specific cell

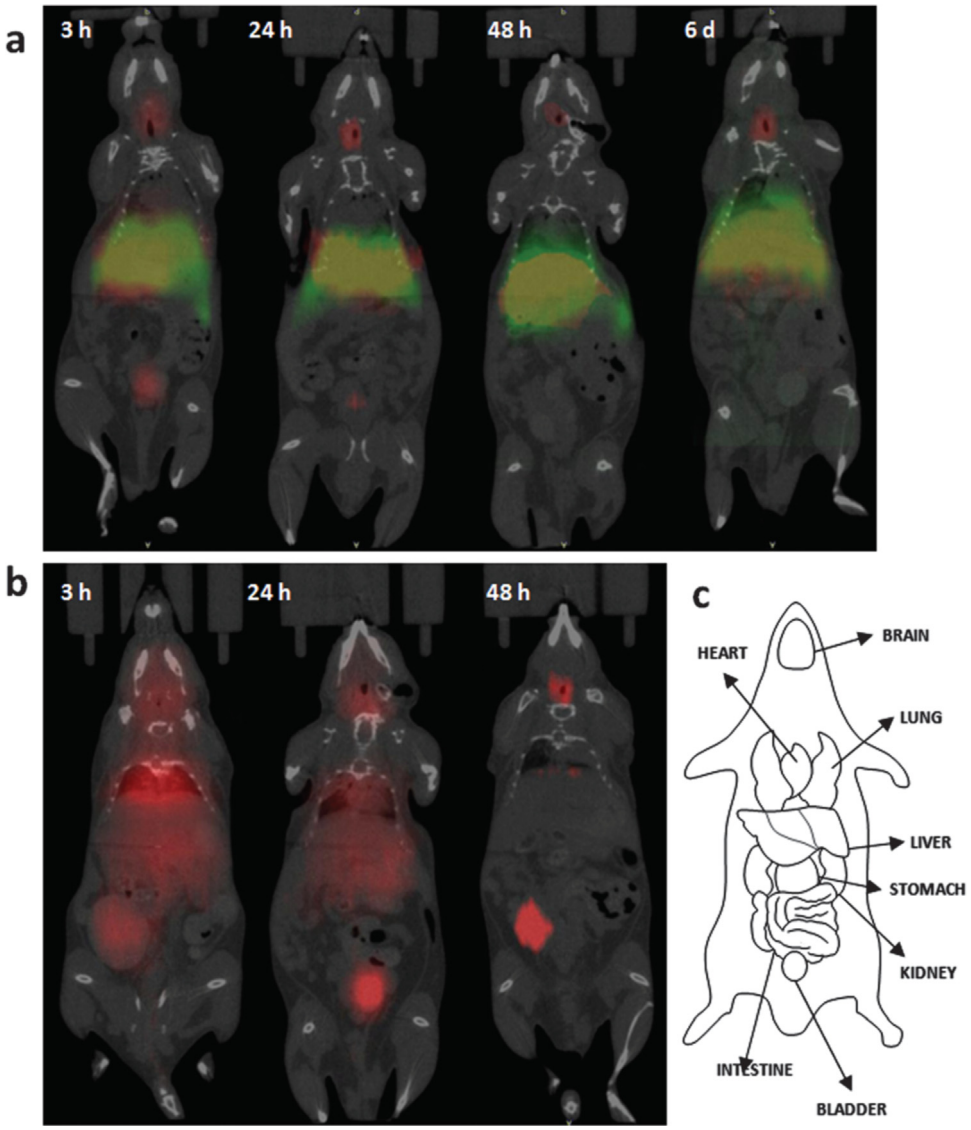

Fig. 10. Distribution of dually radiolabelled nanoparticles in a living mouse as a function of time. The nanoparticles consist of an iron oxide/^{111}In oxide core stabilized with PLGA surfactant and a BSA shell (surface stabilizer) containing ^{125}I labeled tryptophane. (a) Coronal single-photon emission computerized tomography (SPECT) images of the distribution of ^{111}In in the particle core (green). (b) Coronal SPECT images of the distribution of ^{125}I in the particle shell (red). (c) Schematic of the different organs. Different distributions of the core and shell labels are seen, indicating disintegration of the BSA from the nanoparticle core. The particle cores (^{111}In) remain mostly in the liver and lungs, while ^{125}I from the BSA shell travels from the liver and lung to the intestine and thyroid. (Reproduced with permission from Ref. [149].) (For interpretation of the references to color in this figure legend, the reader is referred to the web version of this article.)

receptors, proteins [52,140], and implement sensor functions for specific analytes [5,141–145]. Examples will be described in Sections 3 to 7.

2.7. *Imaging, tracking, and dosimetry of nanoparticles*

Static imaging of nanoparticles is possible directly using TEM, SEM, AFM, and indirectly by spectroscopic methods such as X-ray photoelectron spectroscopy (XPS), IR, Raman, and NMR spectroscopy. Often it is also relevant to monitor the location and fate of nanoparticles within a cell, tissue, or organism, or to identify the distribution within a multiphase material. Such tracking of nanoparticles can be achieved using fluorescent and radiochemical labels [146–149]. For example, to assess the therapeutic performance and potential toxicity of iron oxide-polylactic-co-glycolic acid nanoparticles stabilized with bovine serum albumin (BSA), the core-shell nanoparticles were dually radiolabeled with gamma emitters of a different energy spectrum (Fig. 10). The iron oxide core was modified to contain a small amount of radioactive ^{111}In oxide, and tyrosine residues in BSA on the nanoparticle surface contained small amounts of radioactive ^{125}I introduced by electrophilic substitution. Upon injection into mice under anesthesia, in-vivo tracing of the distribution of ^{111}In in the core (Fig. 10a) and ^{125}I in the shell (Fig. 10b) by single-photon emission computerized tomography (SPECT) showed the disassembly of the core-shell nanoparticles and preferences of accumulation in different organs (Fig. 10c). Imaging and labeling techniques offer a pathway to systematically reveal the distribution, function, and toxicity of nanomaterials.

Labeling of NPs can, however, have effects on the cellular distribution and uptake. As an alternative, label-free high-resolution visualization and dosimetry techniques have been developed, which allow to follow the path and quantify the uptake of NPs at single cell level [150–152]. These methods utilize ion beam microscopy (IBM) techniques such as micro-proton-induced X-ray emission (μPIXE) and micro-Rutherford backscattering (μRBS) for spatially resolved elemental imaging and quantitative analysis. A proton beam is used for scanning the sample in the *xy*-plane at a resolution of about

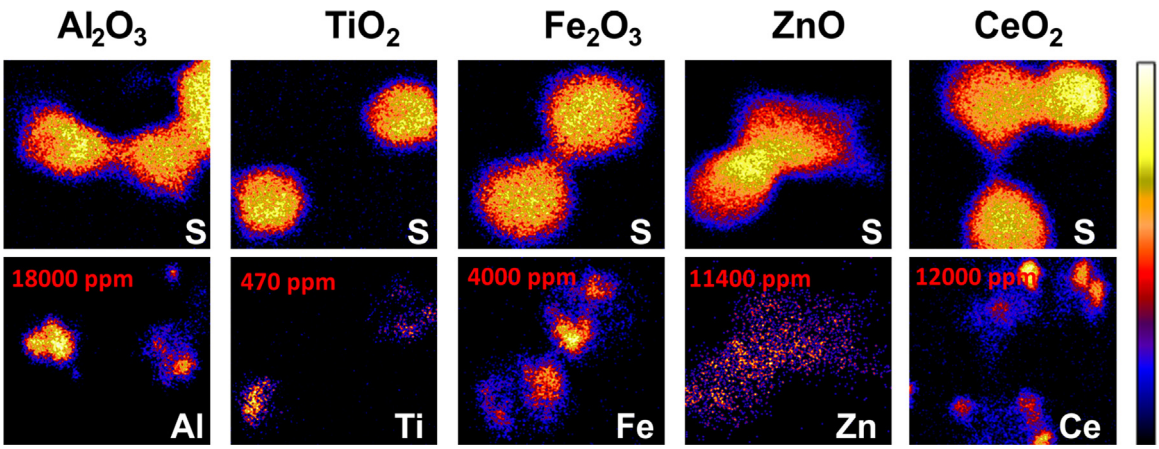

Fig. 11. Micro-proton-induced X-ray emission (μPIXE) elemental mapping of A549 cells exposed to different metal oxide NPs at a concentration of 30 μg/ml for 48 h. Top and bottom images demonstrate S and NP related element distributions, respectively. The color code is as follows: yellow is the maximum, black represents the minimum. The size of all images is 50 × 50 μm. (Reproduced with permission from Ref. [152].) (For interpretation of the references to color in this figure legend, the reader is referred to the web version of this article.)

1 μm. The simultaneous application of μRBS and μPIXE methods delivers unique information on the concentration and distribution of NPs down to the single cell level. IBM allows visualization and quantification of a wide range of NPs in tissues and cells (Fig. 11). Moreover, μRBS can reveal the distribution of NPs in the z-direction with an accuracy of about 100 nm.

Molecule-based imaging techniques such as confocal Raman microspectroscopy (CRM) allow the simultaneous 3D visualization of NPs and their biological environment at a sub-cellular level. CRM provides 3D chemical composition images with a resolution of about 250 nm at tissue and cellular levels. The utility of CRM for cell imaging, subsequent analysis of biochemical and cell physiological processes as well as diagnostic insights has been demonstrated. Examples include label-free imaging of cell organelles [153,154], uptake and intracellular fate of drug carriers [155–157], and nanomaterials inside individual cells [158–160].

2.8. Enthalpy versus entropy of surfactant adsorption

Binding of surfactants is accompanied by changes in enthalpy and entropy. Enthalpies are often the dominant contribution unless long polymer chains are involved. However, it is necessary to distinguish (1) adsorption in the gas phase, (2) adsorption in solution, (3) and whether binding occurs via covalent or non-covalent interactions [121,122,161–170]. Enthalpy contributions to adsorption can usually be obtained in a straightforward manner in experiment, for example, using isothermal titration calorimetry (microcalorimetry), temperature-programmed desorption, or from the determination of binding constants via concentration measurements at different temperatures [76,126,127,171–175]. The computation of enthalpies of adsorption is also straightforward, using a two-state model with simulations boxes of the molecule in adsorbed and desorbed state, respectively, and analysis of the thermodynamic averages of the equilibrium trajectories [99,100,176–180]. In contrast, entropies of adsorption require knowledge of both binding constants and enthalpies, or measurements at different temperatures (temperature programmed desorption, binding constants) to extract the entropy changes from an Arrhenius plot. Similarly, computations require more expensive free energy calculations using umbrella sampling, thermodynamic integration, or steered molecular dynamics in combination with enthalpy calculations to extract entropy changes using the Gibbs relation $\Delta G = \Delta H - T\Delta S$ [164,181,182].

In light of the technical challenges and time requirements to obtain accurate values, it is often helpful to obtain a first estimate of the entropy change by simply using the entropy of freezing or condensation, respectively, which define an upper boundary of the entropy change upon binding. These values correspond to the tabulated enthalpy of fusion, or enthalpy of vaporization of the surfactant normalized by temperature, e.g., $\Delta S_{freeze} = -\Delta H_{melt}/T_{melt}$, $\Delta S_{cond} = -\Delta H_{vap}/T_{vap}$, and can simply be obtained from a reference such as the CRC handbook or thermodynamic tables [183]. The true entropy changes upon adsorption are then just a fraction of this hypothetical maximum since no surfactant entirely freezes upon adsorption [121,122]. This approach is valid for temperatures somewhat off the melting points as well. If the enthalpy of binding amounts to a multiple of this estimated entropy contribution, it can often already be concluded that entropy contributions to adsorption are secondary. Only if the enthalpy and entropy contributions are about equal, entropic factors necessitate further consideration.

Campbell and Sellers have shown that non-covalently bound molecules from the gas phase onto solid substrates retain approximately 2/3 of their gas phase entropy [184]. This relationship was demonstrated for the adsorption of small molecules and hydrocarbons onto Pt, TiO_2, MgO and graphite surfaces. In the gas phase, therefore, the entropy of adsorption equals about 1/3 of the entropy of freezing. If bonding is covalent, rather than non-covalent, surface mobility is more restricted, although measurements and modeling have shown that even physisorbed monolayers of surfactants and gases exhibit limited diffusion. Especially for longer surfactants (> 5 monomers) that are covalently tethered at one end, the entropy difference between chemisorption and physisorption can be regarded negligible. Therefore, entropies of adsorption from the gas phase are typically 1/3 of the entropy of freezing and might be larger for strongly immobilized, chemisorbed surfactants, for example, in case of multiple tethering sites [184].

A helpful consideration for chain molecules, such as polymers and polypeptides, is further the rotational entropy of the chains, which equals the maximum entropy loss upon adsorption [121,185]. A hydrocarbon chain of N monomers and possible anti, (+)gauche, and (−)gauche conformations would possess 3 possible rotational states per monomer, given the temperature is sufficiently high, and $W = 3^N$ states, leading to a maximum enthalpy of "freezing" (adsorption) of $\Delta S = -k \ln W = -Nk \ln 3$. Similarly, a polypeptide with N amino acids can have approximately two choices for the Φ and Ψ angles for each peptide bond and several further rotatable bonds depending on the side chains. On average, these are about 50 rotational states per amino acid and a

maximum number of $W = 50^N$ rotational states and a maximum rotational entropy of $\Delta S = Nk \ln 50$ per polypeptide.

While adsorption in the gas phase is a one-way process and the net entropy change is solely determined by the ligand, adsorption in solution is a two-way process where surfactant molecules arrive at the surface and solvent molecules leave the surface. This equilibrium, or competition, affects both the enthalpy and entropy balance. While enthalpy changes are comparatively easy to measure and rationalize (see Sections 3–7), entropy changes are often left to interpretation. In case of water as a solvent, studies on metal, oxide, and other mineral surfaces consistently indicate that the entropy loss of an adsorbate is fully compensated, or slightly overcompensated by the entropy gain of previously surface-bound water [121,122,186,187].

For example, the free energy of binding of a 7-peptide (KLPGWSG) to different silica surfaces in water was compared with the enthalpy of binding, leading to a comparison 0 vs −1 kcal/mol, −1 vs. −1 kcal/mol, −6 vs. −3 kcal/mol, and −8 vs. −7 kcal/mol with uncertainties of about ±1 kcal/mol (see Section 4.2) [164]. The values are essentially equal, with a tendency of the free energy towards larger negative values, which results from a net gain in entropy upon peptide adsorption due to release of surface-bound water according to $\Delta G = \Delta H - T\Delta S$. The enthalpic contribution remains the major contribution to adsorption within uncertainty. Qualitative comparisons on metal surfaces worked out similarly. A flat-on adsorbing 12-peptide (A3) on the Au (111) surface in water has a binding enthalpy of −40 kcal/mol [121,177]. Nevertheless, the peptide loses up to $-T\Delta S = 12RT \ln 50 = +28$ kcal/mol in entropic contributions upon binding (see discussion above), and the melting enthalpy for water is 1.43 kcal/mol [183]. The 12-peptide replaces ~30 water molecules and loses most of its conformational freedom (+25 kcal/mol) whereas the water molecules gain about two thirds of their original mobility upon being released (−30 kcal/mol). As a result, the two entropy contributions are

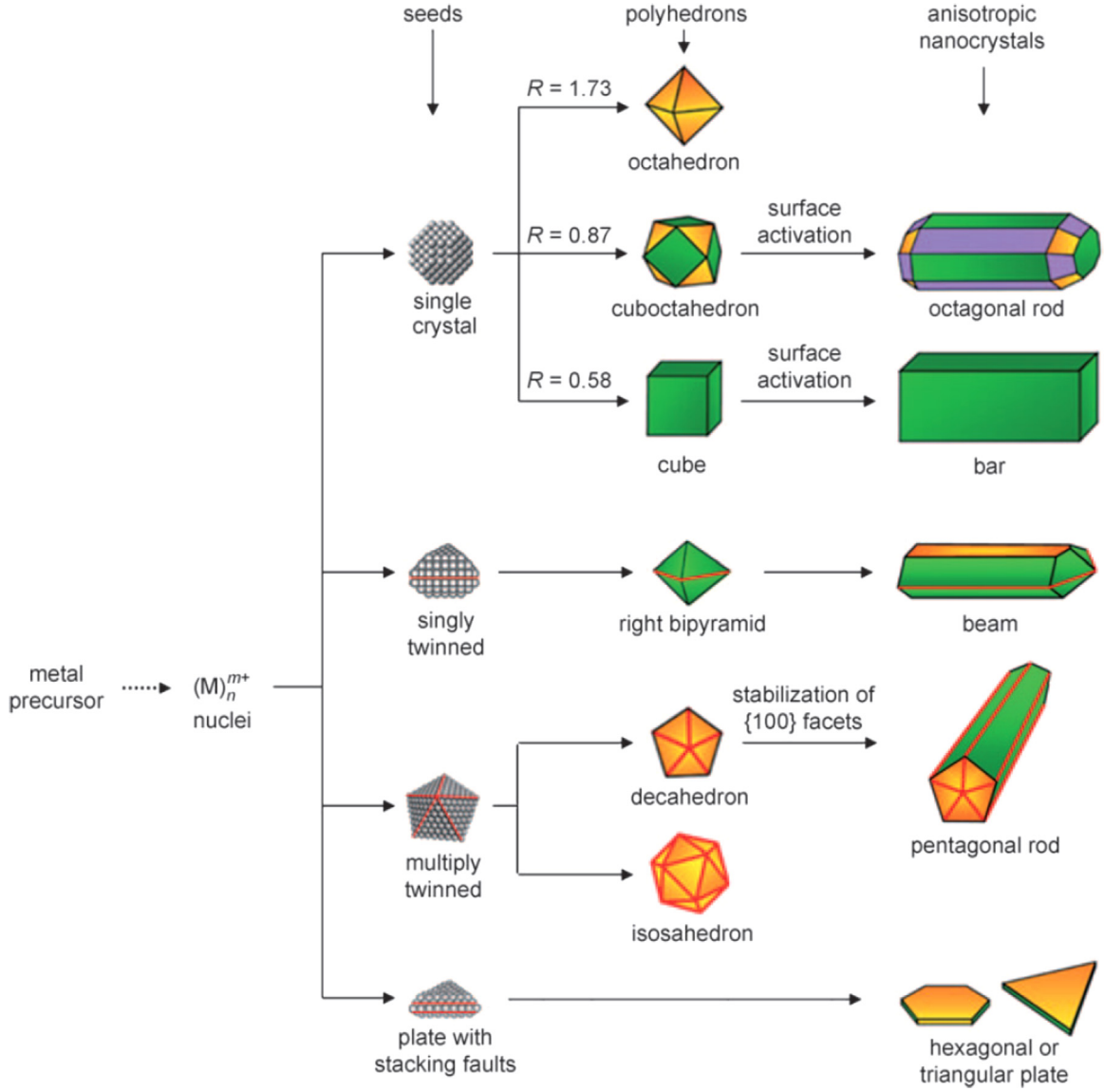

Fig. 12. Reaction pathways that lead to fcc metal nanocrystals of different shapes. First, a soluble precursor is reduced with a strong reducing agent, or decomposed, to form the nuclei (small clusters). Once the nuclei have grown past a certain size, they become seeds with a single-crystal, singly twinned, or multiply twinned structure. If stacking faults are introduced, then plate-like seeds will be formed. Growth from seeds into nanocrystals involves a weaker reducing agent along with specific ligands and capping agents that direct the shape (organic molecules, polymers, surfactants, and ions). The outcomes can also be adjusted by kinetic parameters and added redox equilibria such as underpotential deposition. The green, orange, and purple colors represent (100), (111), and (110) facets, respectively. Twin planes are delineated in the drawing with red lines. The parameter R is defined as the ratio between the growth rates along the $<100>$ and $<111>$ directions. (Reproduced with permission from Ref. [78].) (For interpretation of the references to color in this figure legend, the reader is referred to the web version of this article.)

similar, perhaps with a small negative balance ($+\sim25$ to ~30 kcal/mol ≈ -5 kcal/mol). The exact result depends on chemical details of the peptide side chains (degrees of freedom) and the mobility loss upon binding. The enthalpy contribution to adsorption (-40 kcal/mol) is clearly dominant in this case, too.

When ligands are covalently grafted, enthalpy dominance is similarly observed as bond energies typically range from 50 to 100 kcal/mol. Covalent and noncovalent binding of large proteins and folded macromolecules to nanoparticle surfaces, however, can be notably affected by entropy and kinetic effects [188,189]. To-date, quantitative data on enthalpy versus entropy contributions to surfactant and ligand binding to nanoparticles are limited and more insights would greatly enrich fundamental understanding.

3. Modification of metallic nanostructures with surfactants

Metals comprise more than two thirds of the periodic table of the elements. Nanostructures composed of metals and alloys find broad applications as catalysts, sensors, therapeutics and diagnostics (theranostics), as well as in electrode materials and electronic applications [89,168,177,190–205]. Widely used metal nanostructures to-date consist of precious and other chemically inert metals, for which numerous syntheses have been developed (Fig. 12) [78]. Common synthetic protocols start with a solution of metals salts as a precursor, to which reducing agents such as sodium borohydride (for fast nucleation) and ascorbic acid (for slower growth) are added. Additional surfactants such as cetyl trimethyl ammonium bromide (CTAB), organic ligands (PVP), peptides, as well as buffers (sodium citrate) act as shape-directing agents and modify the surface properties. A major role of the precursors, reducing agents, and shape directing agents is control over nanocrystal shape. Single crystals, single and multiply twinned structures, stars, and plates with stacking faults have been obtained (Fig. 12). The mechanisms vary widely, from diffusion and surfactant controlled adatom deposition to kinetically delayed processes of cluster attachment [203], oxidative etching [206], and underpotential deposition using a secondary metal with a different redox potential [168,207]. The ligands or buffer molecules are typically non-covalently bound to the surface of the metal during synthesis, however, they can subsequently be exchanged for covalently grafted thiols when chemically robust modification is desired (Fig. 5) [49,98,208]. In the following, molecular recognition mechanisms, nanocrystal growth, the preparation and assembly of covalent thiol-modified metal nanoparticles, as well as applications in catalysis and therapeutics are described.

3.1. Noncovalent binding of ligands via soft epitaxy

A major role in shape control is played by the binding characteristics of organic ligands to the metal surface in solution (Fig. 13) [121–123,177]. The mechanism involves soft epitaxial interactions, which can be described as a coordination of polarizable atoms in the backbone (C, N, O, S) with epitaxial sites on the metal surface. To understand this concept, it is helpful to recall that the common face centered cubic (fcc) structure found in many precious metals is a repeating sequence of three atomic layers · · · A-B-C-A-B-C · · · on the (111) surface. The top atomic layer on the metal surface (e.g. the A layer) is on average avoided by the organic ligands while the two similar sublayers (e.g. the B and C layers) provide coordination sites to achieve denser packing to which polarizable atoms preferentially coordinate. Thereby, the solvent and the solute compete with each other for a better fit, and the goodness of soft epitaxial fit decides upon occurrence of a negative or a positive (free) energy of adsorption of the solute. On

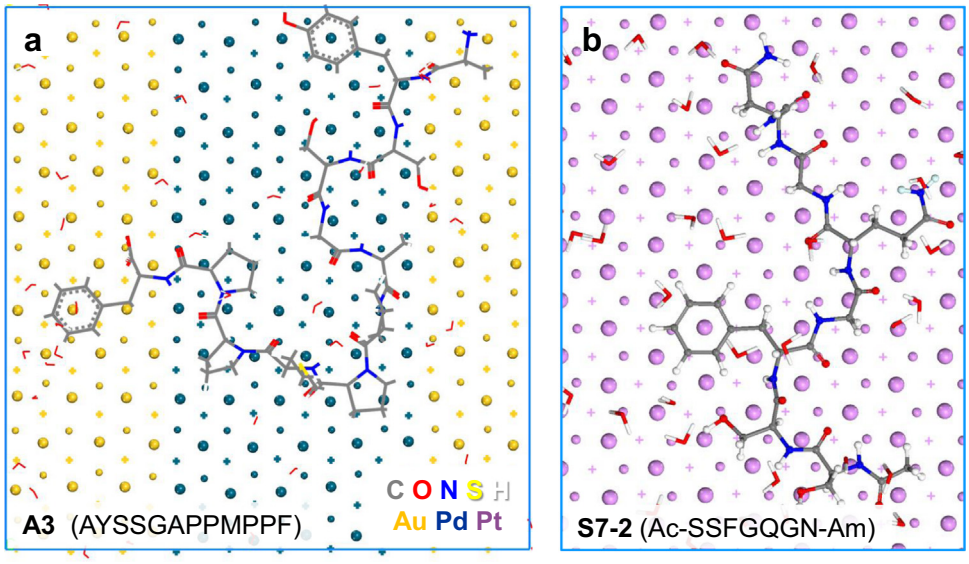

Fig. 13. Representative snapshots of the adsorption of peptides on even fcc metal surfaces in aqueous solution. Polarizable atoms (C, N, O, S) preferentially coordinate epitaxial sites, as illustrated for (111) surfaces of gold-palladium and platinum metal. The peptides A3 and S7-2 were identified by phage display and tested in experiment for specific binding. The time-average number of close contacts of polarizable atoms in each peptide with epitaxial sites, top sites, and of atoms detached from the surface (>4 Å distance from the top layer atoms) is shown. (a) A 4:1 preference for epitaxial sites over top sites is seen on an Au-Pd surface using the CVFF-INTERFACE force field. (b) An approximate 5:1 preference for epitaxial sites versus top sites was found on a Pt surface using the CHARMM-INTERFACE force field, related to higher surface energy of Pt in comparison to Au and Pd. Metal atoms are depicted as large spheres, small spheres, and crosses that distinguish top layer atoms from atoms in subjacent layers (epitaxial sites). (Reproduced with permission from Ref. [123].)

a

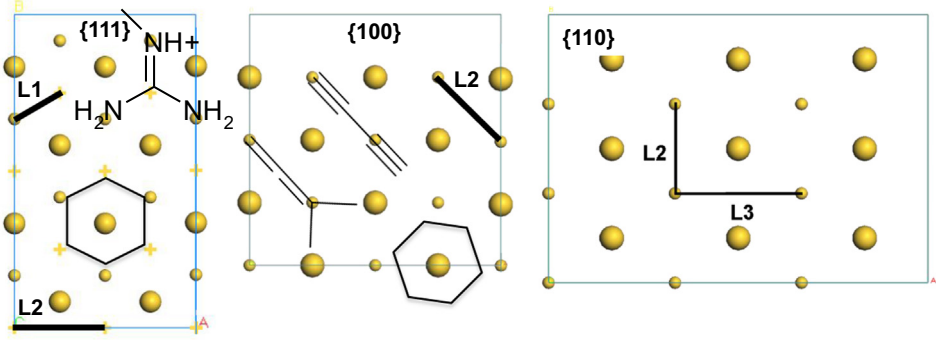

b

	Pb	Ag	Au	Al	Pt	Pd	Cu	Ni
L1 (Å)	2.021	1.668	1.665	1.653	1.602	1.588	1.476	1.439
L2 (Å)	3.5	2.889	2.884	2.863	2.774	2.751	2.556	2.492
L3 (Å)	4.95	4.086	4.078	4.05	3.924	3.89	3.615	3.524

Fig. 14. Concept of soft molecular epitaxy for non-covalent adsorption of organic molecules in solution to metal surfaces. (a) The hexagonal symmetry of the (111) surface provides epitaxial sites (fcc and hcp) that match the common geometry of sp^2 and sp^3 hybridized molecules such as benzene and guanidinium groups. In contrast, (100) surfaces exhibit a square geometry of 2.88 Å spacing (for Au) that is incommensurate with typical chain molecules, yet suitable for allenes and polyynes. The competition between solvent (water) and solutes is then in favor of water and no significant attraction of the organic molecule may be achieved. (110) surfaces possess small and wide grooves that can be further enlarged by surface reconstruction. Due to the wide L3 spacing, adsorption on (110) surfaces becomes less molecule-specific. (b) The similarity in characteristic spacing of epitaxial sites (L1, L2, L3) leads to similar attraction of molecules and polymers to different noble metals. Differences in attraction mostly arise from unique surface energies and characteristic lattice spacing of individual metals. Matching molecules can be designed according to the surface pattern of epitaxial sites, aided by simulation to quantify binding strengths. (Adapted with permission from Ref. [122].)

time average, epitaxial as well as some top sites remain in close contact with polarizable atoms of the ligands; some atoms of the ligand detach from the surface in favor of solvent molecules (Fig. 13). The major share of contact remains of epitaxial nature. This mechanism of adsorption of chain molecules is similar to that of the epitaxial deposition of metal atoms in vacuum onto a given metal surface, only with lesser precision, solvent-solute competition, and lower energy barriers for rearrangement on the surface [121,177,209]. The non-covalently bound surfactants retain significant mobility, allowing dynamic reconstructions of the surfactant layer on nanosecond to microsecond time scales.

The reason for such soft epitaxial preferences is the very high surface energy of metals (up to 3000 mJ/m^2) [130,210] in combination with the lattice spacing (Fig. 14). Especially (111) facets have an L1 spacing of 1.5 Å to 1.7 Å that is close to common C–C and C=C bond lengths in sp^3 and sp^2 hybridized carbon backbone chains, as well as a hexagonal symmetry with angles of 120º that is close to related C–C–C bond angles of 109º and 120º, respectively (Fig. 14a). Therefore, phenyl rings, guanidinium groups, and several other molecular features in extended molecules can easily adapt to the surface topography of (111) facets and enhance binding by multiple contacts with epitaxial sites (Fig. 13). This concept was discovered by molecular dynamics simulations [121] and is supported by a broad range of experimental data [122,123,130,177,209,211,212] as well as DFT results [213]. In aqueous solution, most organic molecules and peptides directly adsorb onto Ag, Au, Pd, Pt, and other metal surfaces without a water interlayer and with a significant adsorption energy. Common adsorption energies are −20 to −50 kcal/mol for a 7-peptide at high dilution, and the adsorption energy increases to larger negative values for longer molecules. The adsorption is also stronger the higher the surface energy of the metal (Pb < Al < Ag < Au < Cu < Pd < Ni < Pt) [210,214].

Adsorption on (100) surfaces requires matching to a different, square pattern of epitaxial sites and the critical spacing is the L2 spacing of approximately 2.5 Å to 2.9 Å depending on the metal (Fig. 14a). A phenyl ring, for example, cannot achieve a good fit to epitaxial sites on the (100) surface and molecular ligands often remain separated from (100) surfaces by an interlayer of water molecules between the metal surface and the ligand. Adsorption energies are then also closer to zero, sometimes positive, and rarely more attractive than −5 kcal/mol for a 7-peptide in dilute aqueous solution (in the absence of covalently binding thiol groups) [123].

The binding energy, in addition, also strongly depends on the concentration of the peptide and the corresponding surface coverage on the nanoparticle, on the shape of the nanoparticle (e.g. edges versus inner parts of facets), and on the peptide sequence [123,177]. At monolayer coverage for attracted peptides, adsorption energies tend to be on the order of −10 kcal/mol for a 12-peptide, which is much stronger adsorption in comparison to single peptides at high dilution on (100) surfaces (closer to zero) [173,215]. Finally, the (110) surface exhibits wider grooves as seen from the L3 spacing near 4 Å (Fig. 14a). The wider spacing leads to less molecule-specific adsorption, as demonstrated by oriented patterns of adsorbed molecules along the groves [216].

The soft epitaxial binding mechanism has been shown to be the same for a range of noble metals related to the similar lattice spacing (Fig. 14b). Support comes from strong binding of gold (111) binding peptides also to Ag (111), Pd (111), and Pt (111) surfaces, as well as the similarity of amino acids in other strongly binding peptides to any of these metals identified by phage display (e.g. Arg, Tyr, Trp, His, Phe) [81,217–222]. It has also been observed that the surface of some metals such as gold undergoes reconstruction at length scales larger than one nanometer [223,224]. Therefore, higher index facets are often present on nanorods and nanocrystals [225,226]. The principal mechanism of adsorption remains the same, however, and molecules adjust to the local (*h k l*) geometry. Computational methods can predict the interaction strength and visualize surface potentials in near-quantitative agreement with experiment [130,177,213,227].

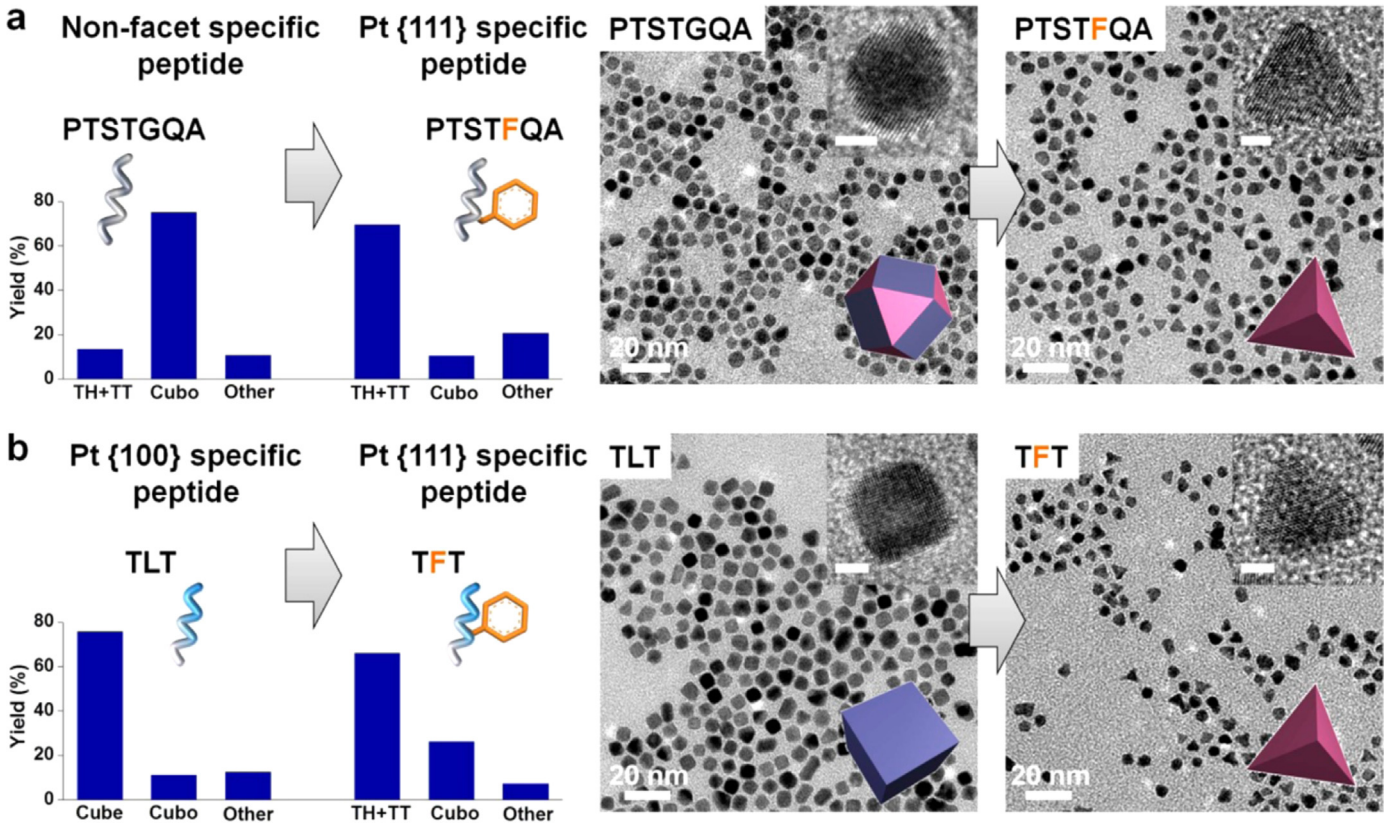

Fig. 15. Biomimetic design of peptides with Pt (111) specificity. (a) Demonstration of turning a non-facet specific Pt binding peptide (PTSTGQA) into a Pt (111) specific peptide (PTSTFQA) by including a phenyl ring (F). (b) Demonstration of switching a Pt (100) specific peptide (TLT) into a Pt (111) specific peptide (TFT) through the phenyl ring. Yields of NC shapes are shown on the left side. TH stands for tetrahedra that are bound by (111) facets, TT stands for truncated tetrahedra, and cubo stands for cuboctahedra. Uncertainties are $< 5\%$ for all data points. Corresponding TEM images of as-synthesized NCs are shown on the right side. Scale bars in inserted HRTEM images are 2 nm. (Adapted with permission from Ref. [209].)

3.2. *Relationship between facet-specific ligand binding and nanocrystal growth*

Facet-selective binding of ligands has been exploited to direct nanocrystal growth. For example, the preference of phenyl rings towards (111) facets was employed in a series of ligands to direct the growth of Pt and Ph nanocrystals into tetrahedra, which are exclusively bound by (111) facets (Fig. 15) [81,209,228]. The introduction of a single F residue anywhere in the sequence of a 7-mer peptide changed the shape of nanocrystals to tetrahedra upon growth of seed crystals in solution, whereas other peptides containing no phenylalanine (F) residues form cuboctahedra or cubes [209]. Even minor mutations, such as the substitution of F to tyrosine (Y) in the same peptide sequence no longer supports the formation of tetrahedral nanocrystals. While both F and Y containing peptide sequences bind strongly to (111) facets, the phenol ring in Y also binds with a negative binding energy to (100) facets in contrast to F with a positive binding energy. The binding differential between (111) and (100) facets in the presence of Y is then lost, protecting both (100) and (111) facets from crystal growth. Simulation tools such as the CHARMM-INTERFACE force field that accurately reproduce interfacial properties help elucidate specific molecular conformations and the dependence of binding processes from ligand chemistry, concentration, and pH value, consistent with experimental observations of the shape, size, yield, and spectroscopic properties of nanocrystals [123,209].

Traditional surfactants such as CTAB (n-$C_{16}H_{33}$–$N(CH_3)_3^+$ Br^-) and CTAC (n-$C_{16}H_{33}$–$N(CH_3)_3^+$ Cl^-) are also known to affect nanocrystal shape (Fig. 16) [89,229]. Specific halide ions such as Cl^-, Br^-, I^- can be used to adjust the reduction potential of ionic gold

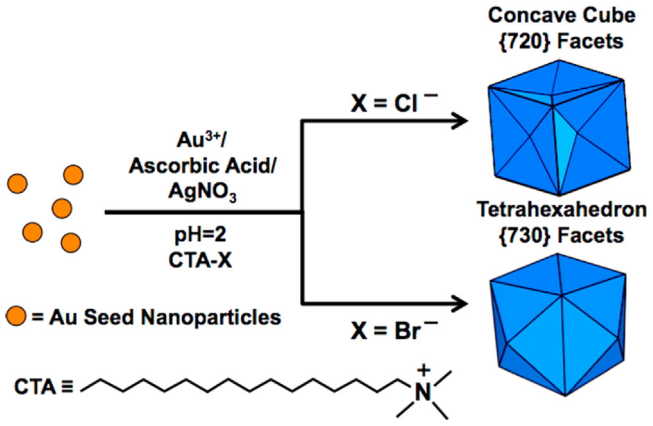

Fig. 16. In seed-mediated synthesis of gold nanoparticles, the use of a silver ion additive in the presence of a chloride-containing surfactant (CTA-Cl) results in the growth of (720)-faceted concave cubes (upper growth pathway), while the use of a bromide-containing surfactant (CTA-Br) under otherwise identical conditions results in the growth of (730)-faceted tetrahexahedra (lower growth pathway). (Reproduced with permission from Ref. [229].).

species in solution and passivate the gold nanoparticle surface [230]. The differences control the reaction kinetics and enable the selective synthesis of different particle shapes, especially when additional shape directing agents such as Ag^+ ions are introduced. Simulations indicated that the presence of Ag^+ ions favors protection of (110) and (100) facets over (111) facets in the synthesis of gold nanorods in ionic liquids, thus leading to preferential growth in the (111) direction [168]. Halide ions such as Cl^- and Br^- likely stabilize (100) surfaces according to DFT and molecular

dynamics simulations, supported by a soft epitaxial match [179,227,231]. The formation of open (520) facets was proposed to be related to the formation of complexes between surfactants, bromide, and silver ions on specific facets [180]. The exact role of additives in the formation of highly specific facets such as (310) and (720) still remains uncertain [229,232]. In summary, the mechanisms for shape controlled synthesis are known in certain cases and benefit from further investigations, as many excellent proposals have been made [77,78,81,112,123,203,209,228,233–235]. An increasing role is anticipated by simulation tools in atomic resolution that allow visualizations of the organic-inorganic interfaces and support the elucidation of mechanisms for specific systems [130,236].

The thermodynamic equilibrium shape of nanoparticles can also be predicted by the Wulff construction that relies on knowledge of the (h k l) surface energies obtained from experiment or computer simulations [237,238]. The crystal shape is then bounded by planes that are represented by all (h k l) vectors of the surface energies. Nanoparticle modification with surfactants alters the (h k l) surface energies of the nanoparticles and thereby its preferred shape [238]. Predictions of thermodynamically preferred equilibrium shape using this method have been made based on first principles and molecular dynamics simulations for systems with ten thousands of atoms [99,238–242]. Such estimates of equilibrium shapes, however, cannot be related to the kinetically controlled crystal growth and shape evolution of the vast majority of known anisotropic metal nanostructures obtained by reductive synthesis.

3.3. Nanoparticle superlattices from densely grafted rigid thiol surfactants

A very common modification of precious metal surfaces involves the covalent attachment of alkane thiols and functionalized alkane thiols via metal-sulfur bonds (Fig. 5) [36,49,101,208,243]. The grafting of functional thiol ligands has become a versatile method to adapt the chemical environment of the nanoparticle surface to application-specific needs (see Section 2). A particular highlight is the attachment of rigid DNA surfactants (Fig. 7 and Fig. 17) [79,109,111], in which an binding group such as a thiol or an azide anchors the surfactants to the nanoparticle, a spacer fragment provides some surfactant mobility near the metal surface, and a covalently bonded ssDNA recognition sequence enables hybridization of the DNA to form rigid strands. These spatially directed surfactants do not collapse on the curved nanoparticles as is the case for flexible alkyl chains (Fig. 6) and allow ordering of the nanoparticles into a variety of superlattices (Fig. 18). The crystal symmetry of these lattices can be controlled by DNA linker length, DNA linker sequence, and by the molar ratio of nanoparticles with different rigid DNA surface modification. In essence, DNA hybridization thereby directs nanoparticle assembly along a pathway that mimics atomic crystallization. Reported nanoparticle superlattices include fcc, hcp, bcc, simple cubic structures and other crystal geometries [112]. Recently, crystallization into Wulff polyhedra has also been shown [77].

It remains challenging, however, to predict reliably the outcome of such molecular crystallization processes as they are influenced by molecular interactions and solvent involvement [77,113]. Very slow cooling, over several days, of solutions of complementary-DNA-modified nanoparticles through the melting temperature of the system was necessary to yield the thermodynamic product with a specific and uniform crystal habit.

3.4. Applications in catalysis

Metal and alloy nanoparticles as described above are widely used in catalysis, including electrode materials in fuel cells, batteries, and active nanoparticles for the synthesis of commodity

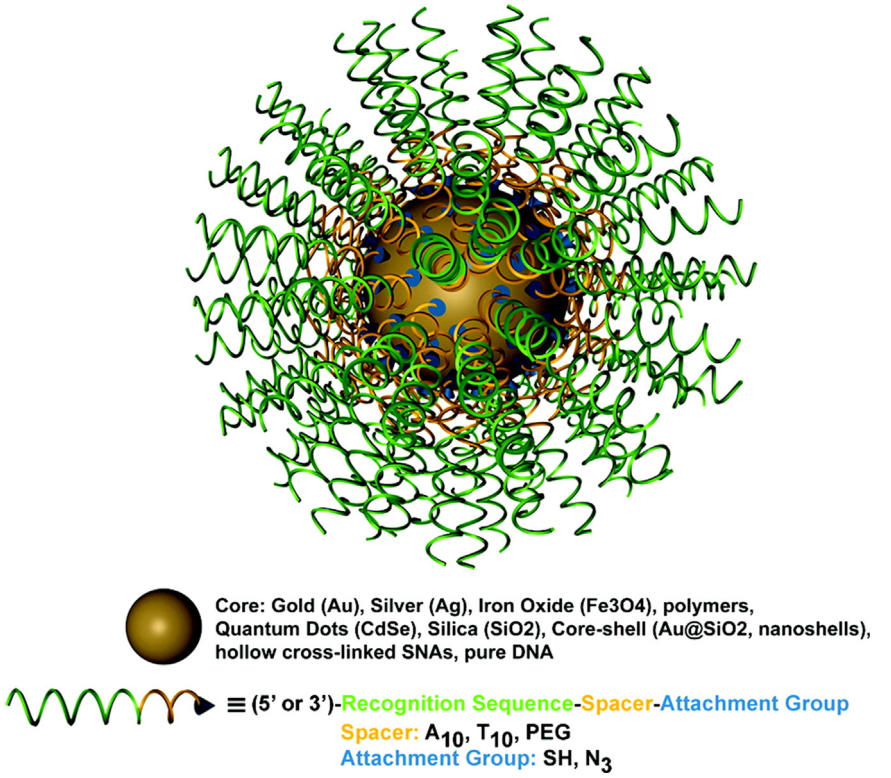

Fig. 17. Grafting of rigid DNA surfactants to metallic and oxide surfaces for the assembly of particle superlattices. An inorganic core is densely functionalized with oligonucleotides containing three segments: a recognition sequence, a spacer segment, and a chemical-attachment group. Additionally, other functional groups such as dye molecules, quenchers, modified bases, and drugs can be attached along any segment of the oligonucleotide. (Reproduced with permission from Ref. [111].)

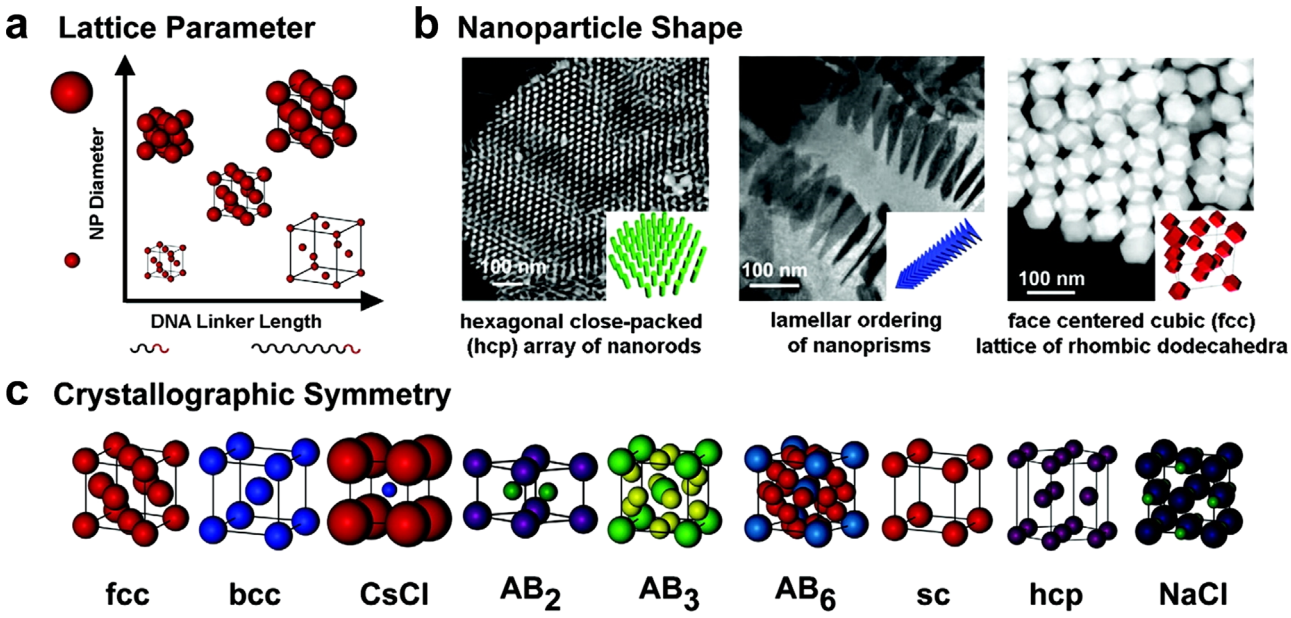

Fig. 18. Illustration of DNA-programmable nanoparticle assembly into ordered superlattices. Parameters that can be controlled using this technique are shown. (a) The lattice parameter can be tuned by using different linker lengths and NP diameters (figure not to scale). (b) NP shape can be controlled, resulting in directional bonding of different anisotropic NPs into a variety of one-, two-, and three-dimensional lattices. (c) Crystallographic symmetry can be adjusted by linker lengths, linker sequences, and molar ratios of particles. (Adapted with permission from Ref. [111].)

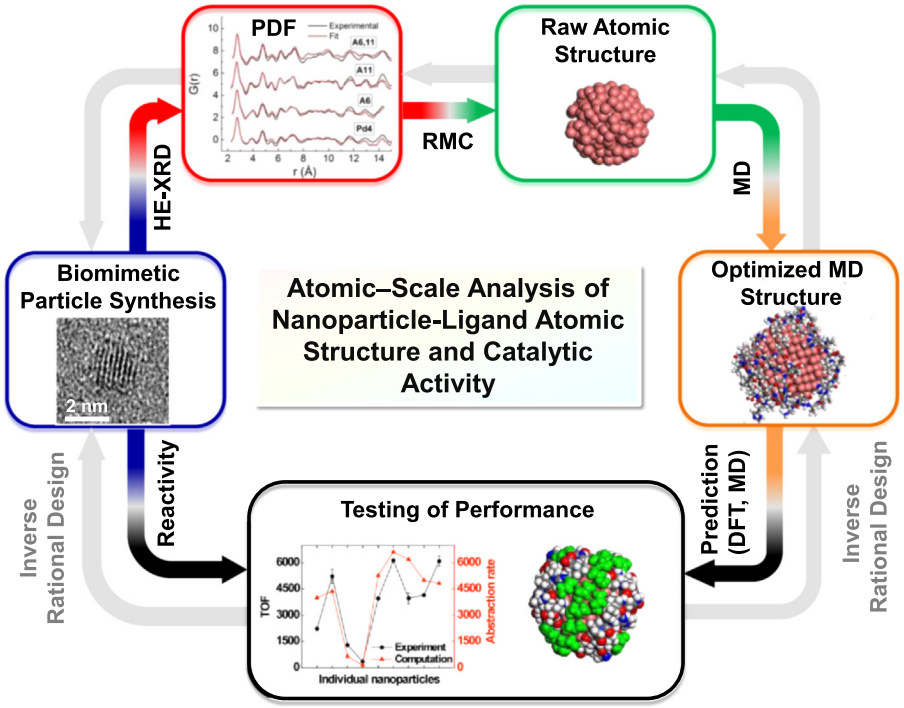

Fig. 19. Engineering functional nanoparticles (NP) using biomolecules for catalytic performance. Peptide-capped Pd NPs were synthesized and analyzed using a combination of high-energy X-ray analysis, pair distribution functions, and reverse Monte Carlo (RMC) simulation, which reveals the average particle structure in near-atomic detail. The structures were used for multi-scale simulation of ligand binding and computation of catalytic activity in comparison to turnover frequency measurements. Insight from specific reactivity and peptide binding characteristics for test systems can be utilized to inversely predict more effective NPs and biomolecular ligands for testing in laboratory using quantitative structure-activity relationships. (Adapted with permission from Ref. [80].)

chemicals [113,169,202,244–254]. High energy X-ray diffraction (HE-XRD) [85], TEM, and electron tomography [87,88,255] can provide critical information of particle shape and structures in atomic resolution that is helpful to assess and explain catalytic functionality [80,133]. The use of HE-XRD, which requires only short measurements of several minutes to determine pair distribution functions of metal atoms in a given nanostructure, is comparably cost-effective and applicable to many samples [256,257]. The combination of synthesis, HE-XRD, reverse Monte Carlo simulation, and molecular dynamics simulation enables the derivation of all-atomic particle models consistent with laboratory data to explain catalytic activity in agreement with turnover frequency (TOF) measurements (Fig. 19). The combination of characterization and activity testing paired with reactive molecular dynamics or ab-initio simulations of the rate-determining step revealed key parameters and rate predictions for a range of

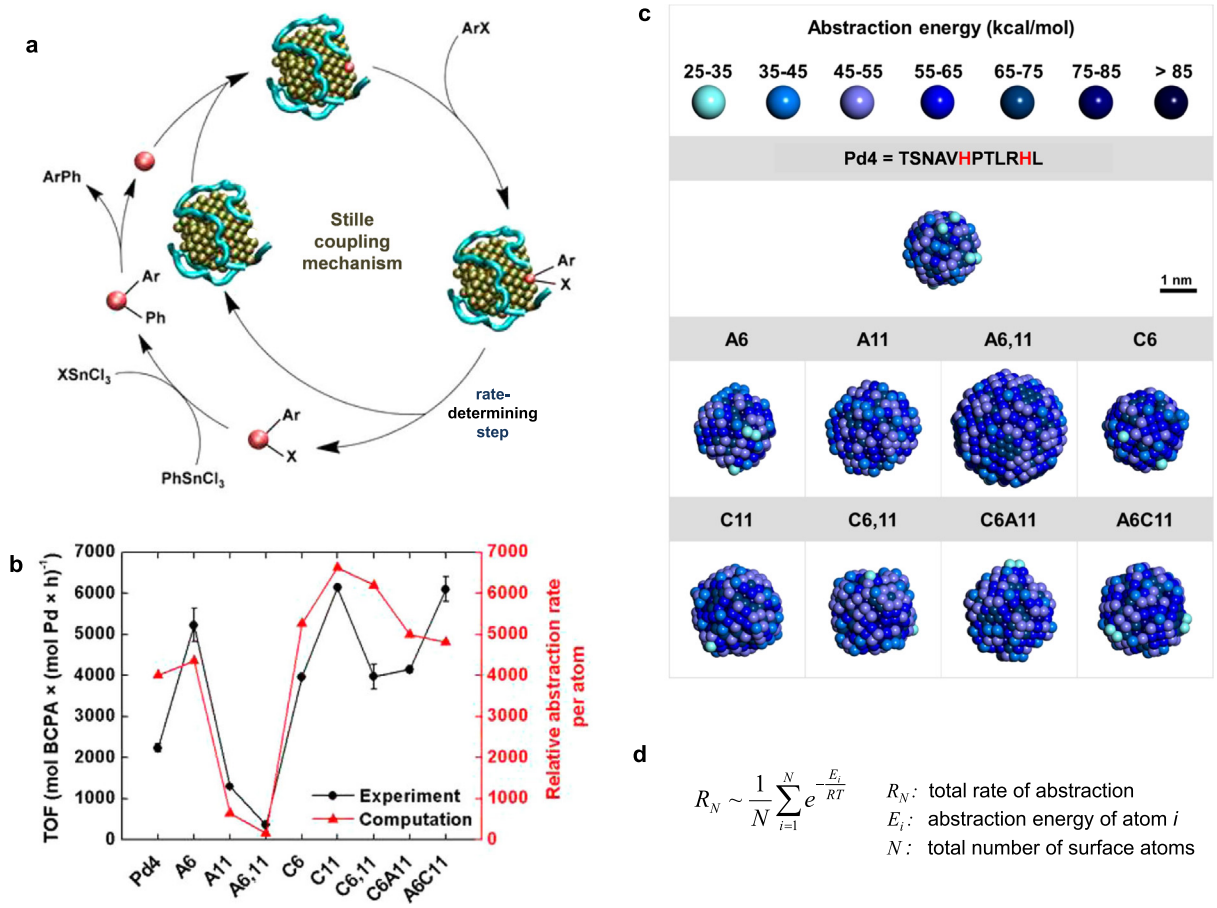

Fig. 20. Catalytic performance of peptide-capped Pd nanoparticles of different size and surface structure in Stille carbon-carbon coupling reactions according to experiment and estimates from reactive molecular dynamics simulations with the CHARMM-INTERFACE force field. (a) Mechanism of the Stille reaction on the surface of Pd nanoparticles. Abstraction of a superficial Pd atom by the ArX moiety was found to be the rate-determining step. (b) Correlation of the measured catalytic turnover frequencies (TOF) with the computed rate of atom leaching for various peptide-derived Pd nanoparticles. (c) Illustration of the abstraction energies for all individual surface atoms of the Pd4-derived nanoparticles and mutant-derived nanoparticles. The original peptide sequence Pd4 (TSNAVHPTLRHL) was modified in 6 and 11 positions by Ala and Cys, respectively. The most active sites, i.e., Pd atoms of lowest abstraction energy, are indicated in lighter color. (d) Calculation of the relative reaction rate from computed atom abstraction energies across the particle surface using statistical weights given by the Boltzmann factor. (Adapted with permission from Ref. [80].) (For interpretation of the references to color in this figure legend, the reader is referred to the web version of this article.)

structures with systematic variation in catalyst shape and composition [80].

Knowledge of the rate-determining step from experiment, or from high level electronic structure calculations, is thereby essential to computationally estimate the rate for a particular chemical reaction, as shown for a Stille coupling reaction as an example (Fig. 20a) [202]. The shape and reactivity of Pd nanoparticles is "imprinted" by the chosen peptide ligands upon synthesis. The critical size for crystallization of fcc Pd nanoparticles at room temperature is about 1.5 ± 0.2 nm [252]. Below this size no stable facets are present and melting temperatures of the particles and atomic clusters, respectively, are much lower than for the bulk metal. Characterization of the particle catalysts in a 2–4 nm size range in atomic resolution and modeling of the reactivity enables insight into peptide engineering to tailor relevant surface features (Fig. 20b and c).

The relative reactivity of several different Pd nanoparticles was then computed using reactive molecular dynamics simulations with the CHARMM-INTERFACE force field and agrees semi-quantitatively with TOF measurements for the same particles (Fig. 20b). The particles were synthesized using the original peptide TSNAVHPTLRHL and a series of mutants in which the residues H6 and H11 were replaced by Ala as a less binding residue (Ala) as well as by Cys as a thiol-bridging residue (Cys) [80]. Key to understanding reactivity of the nanoparticles was the unique fingerprint of atoms of low abstraction energy (Fig. 20c, light blue). The relative reaction rate was obtained by computation as a Boltzmann-average over all surface atoms, consistent with TOF measurements (Fig. 20d). Thereby, molecular dynamics simulations can quickly scan the abstraction energies of all surface atoms to compute relative reaction rates. The peptide ligands play no direct role in the reaction rate of the Stille reaction, as the energy barriers for the aryl halide to approach the bare surface are much lower than the minimum abstraction energy of 25 kcal/mol for individual Pd atoms (moving a few peptide residues sideways to access a surface site costs between 5 and 10 kcal/mol). Therefore, the role of the peptide ligands in the context of the Stille reaction lies in the initial synthesis and shape control of the nanoparticles that creates active sites, without a direct contribution in the catalytic cycle [133].

Similar approaches explained the reaction rates of the same set of Pd nanoparticles in olefin hydrogenation. The rate-determining step was then the docking of the reactant onto the surfactant-covered and hydrogen-saturated nanoparticle surface. Thiol ligands thereby showed near-zero rates, likely due to scavenging and deactivation of surface adsorbed hydrogen [80]. Control of the Pd catalyst poisoning level with tailored surfactants is also critical to increase the selectivity in hydrogenation reactions of acetylenic compounds [253]. DFT simulations have guided in the understanding the relative accessibility of active sites in Lindlar catalysts

for different thiol surfactant coverage on palladium surfaces, showing that increased packing density with upright oriented orientation of surfactants (see Figs. 3 and 5) can decrease the poisoning level and increase reactivity [254].

Alloy nanoparticles are used to catalyze many other conversions. Examples are graphene-supported Pt-Co alloy nanoparticle catalysts stabilized by HEPES buffer and other surfactants that enhance the catalytic activity in the oxygen reduction reaction (ORR) in fuel cells [244], as well as Au-Pd alloy nanoparticle catalysts for ORR and for the methanol oxidation reaction (MOR) [258]. Pt-Hg alloy nanoparticles were found to be effective for the oxygen reduction to H_2O_2 [246]. Definitive reaction mechanisms and understanding of the role of surfactants, however, are often unclear and benefit from further studies.

3.5. Applications in diagnostics and therapeutics

Functionalized gold and other metal nanoparticles are widely used in diagnostics and drug delivery [243,259,260]. Imaging for diagnostic purposes can be achieved through fluorescent labels or use of anisotropic nanorods that exhibit specific surface plasmon resonance [199,261]. A multitude of diagnostic sensor platforms based on specific binding of analytes to the metal surfaces has been developed. Femtomolar detection limits for protein and DNA target analytes can be reached, equal to the theoretical detection limit using microfluidic nanoscale sensors [145,262–264].

Much in the same way, decorated metal nanoparticles are suitable for drug delivery (Fig. 21) [243]. Advantages include (i) a high surface area that provides sites for drug loading and enhances solubility and stability of loaded drugs, (ii) the ability to functionalize the nanoparticles with targeting ligands to enhance therapeutic potency and decrease side effects, (iii) the advantage of multivalent interactions with cell surface receptors and other biomolecules, (iv) enhanced pharmacokinetics and tumor tissue accumulations compared to free drugs, as well as (v) the biological selectivity which allows nanoscale drugs to preferentially accumulate at tumor sites due to their "leaky" blood vessels, the so-called enhanced permeability and retention (EPR) effect [265]. Classical nanoparticle alternatives such as liposomes, polymeric nanoparticles, and protein-based nanoparticles possess physical properties such as size and high surface area, but lack unique optical and photothermal properties of gold and other metal nanoparticles [52].

Specifically, the unloading or loading of drugs can be accomplished by incorporation of drugs into a surfactant bilayer (Fig. 21a), by incorporation of drugs into an amphiphilic corona layer (Fig. 21b), by direct anchoring of drugs to the metal surface via thiolates (Fig. 21c), using DNA-thiol modified gold nanoparticles that release double-stranded or single-stranded DNA upon laser stimulation (Fig. 21d and e), by attachment of therapeutic agents to the far terminus of surfactants that can be cleaved off by hydrolysis, light, heat, or changes in pH (Fig. 21f), using layer-by-layer assembly and triggered release by changes in pH and charge reversal (Fig. 21g), by incorporation into the matrix of a cross-linked polymer and photothermal heating of Au nanoparticles in the same matrix (Fig. 21h) [243].

Surfactant-modified metal nanoparticles are also used in coatings and paints for corrosion inhibition [54,266–268] as well as in highly effective plasmonic superstructures with controlled circular dichroism [199].

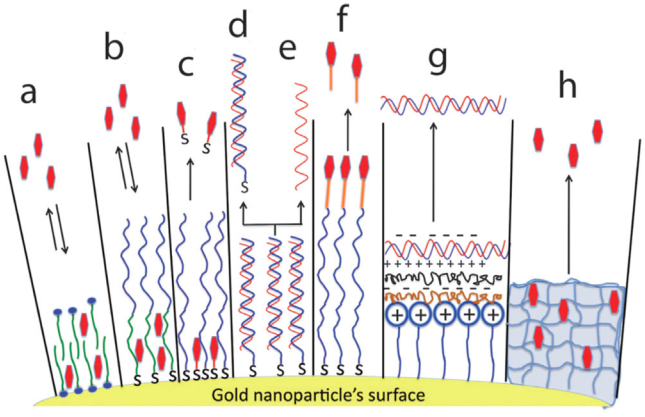

Fig. 21. Illustration demonstrating various approaches to loading/unloading therapeutics into/from gold nanoparticles. (a, b) Partitioning and diffusion-driven release of hydrophobic drug molecules in a surfactant bilayer or an amphiphilic corona layer. (c) Anchoring drugs directly to the surfaces of gold nanoparticles through Au–S or Au–N bonds (capping agent in blue is hydrophilic polymer, e.g. PEG, to enhance the overall solubility of the system). Release is triggered by the photothermal effect, thiol exchange (e.g. glutathione exchange), or simple diffusion to the cell membranes (in the case of Au–N). (d, e) Double-stranded DNA-loaded gold nanoparticles via Au–S bonding. The release of double (d) or single (e) stranded DNA can be controlled by an applied laser. (f) Therapeutic agents are coupled/complexed to terminal functional groups of the capping agent via a cleavable linker. Release can be triggered by hydrolysis, light, heat, and/or pH changes. (g) Loading charged biomolecules (e.g. DNA or siRNA) onto the surfaces of gold nanoparticles by electrostatic assembly (layer-by-layer coating). Release of the payload can be triggered by the use of charge-reversal polyelectrolytes combined with pH change. (h) Drug molecules are incorporated into the matrix of a thermosensitive, crosslinked polymer. Release can be triggered by the photothermal heating by gold nanoparticles also incorporated into the matrix. (Reproduced with permission from Ref. [243].) (For interpretation of the references to color in this figure legend, the reader is referred to the web version of this article.)

4. Modification of oxide and chalcogenide nanostructures with surfactants

Oxides and chalcogenides are abundant materials and its properties differ from that of metals mainly due to lower surface energy and diverse acid-base chemistry. Surface modifications of oxide and chalcogenide nanoparticles may involve covalent (Fig. 8) [114] as well as noncovalent grafting and are described in this section, with the exception of 2D layered nanostructures that are separately discussed in Section 5. Applications comprise catalyst supports [269], supercapacitors [270], batteries [271,272], photosensitizers, organic electronics [273–275], fluorescent labels, sensors [141,142], drug delivery vehicles [276–279], and fillers in polymer nanocomposites [82,141,189,280]. First, noncovalent interactions of surfactants and biomolecules with oxide and chalcogenide nanoparticle surfaces will be described, including the sensitivity to surface chemistry and pH. Then, covalent surface modifications discussed. Directed crystal growth in the presence of surfactants, charge transfer at titania interfaces, optical properties of quantum dots, as well as therapeutic applications are highlighted.

4.1. Surface chemistry and noncovalent binding mechanisms of surfactants

4.1.1. Surface chemistry

Noncovalent interactions often precede covalent attachment and follow rather different mechanisms compared to metal surfaces due to the variable surface chemistry of oxides and hydroxides [126,281–284]. The area density of hydroxyl termination in solution and specific protonation-deprotonation equilibria are critical for selective binding of ligands and assembly of nanostructures. On silica surfaces, as an example, the density of silanol groups (≡SiOH) and of ionized siloxide groups ($\equiv SiO^- \cdots Na^+$) can vary across orders of magnitude and depends on the type of

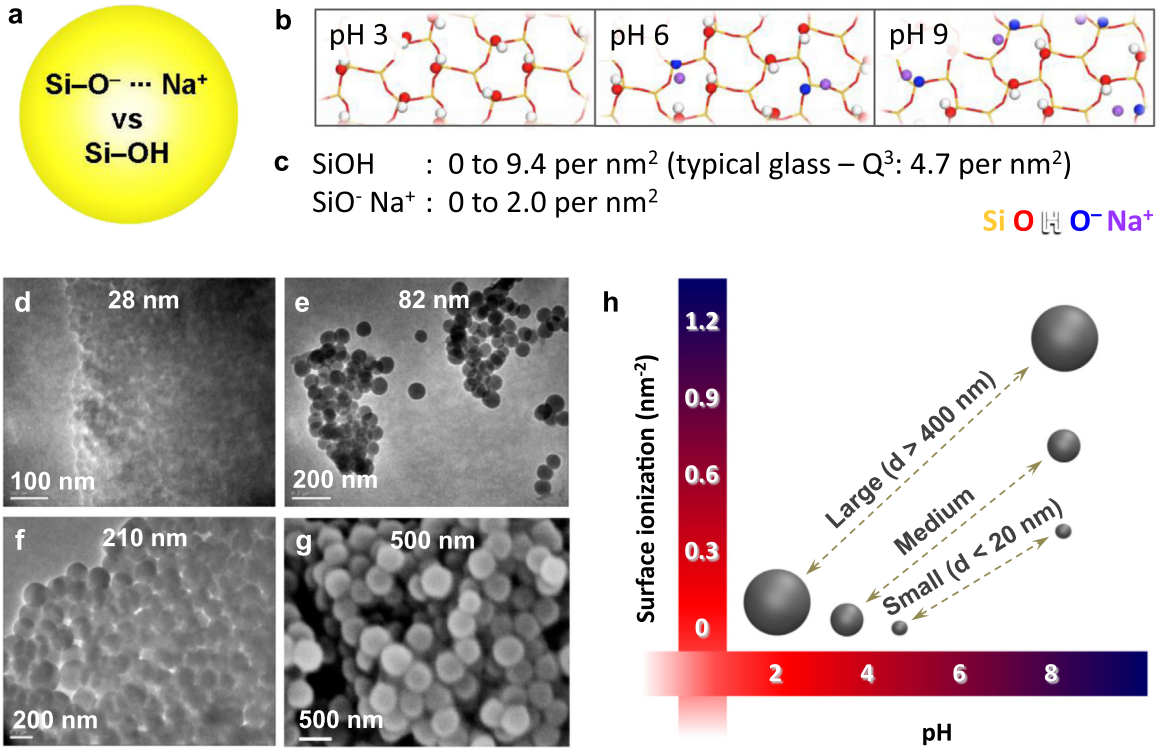

Fig. 22. Silica surface chemistry and its dependence on synthesis and pH values. (a) Key surface parameters are the area density of siloxide groups and silanol groups. (b) Schematic of the surface composition as a function of pH for a typical silica glass with 4.7 silanol groups per nm^2. (c) Common range of silanol area density and deprotonation to sodium siloxide. (d-g) TEM and SEM images of nanoparticles of average sizes 28, 82, 210, and 500 nm. Silica nanoparticles of size 28 nm are less dense and poorly defined in comparison to spherical larger particles. (h) Schematic relationship between surface ionization, pH, and particle size. Large nanoparticles contain Q^2/Q^3 surface environments, medium size and smaller nanoparticles contain mostly Q^3 environments. The amount of SiO^-Na^+ groups per nm^2 is shown at an ionic strength of 0.1–0.3 mol dm^{-3}. (Adapted with permission from Ref. [284].)

substrate, prior processing history, as well as the pH value in solution (Fig. 22) [126,284]. Extensive data on surface chemistry and surface ionization have been reported experimentally and the specifics for a given silica species determine the adsorption of surfactants, biomolecules, and polymers [282,285–295]. Common surface chemistries of silica have also been implemented in an atomistic model database for predictions by molecular modeling and simulation [236,284].

Typical silica surfaces consist of Q^3 silica, i.e., silicon atoms surrounded by three bridging oxygen bonds and one silanol group ($(-O-)_3SiOH$). The area density of silanol groups is then ~4.7 per nm^2 (Fig. 22a–c). Silica or glasses with low content of other oxides and annealed at very high temperatures above 1200 °C no longer contain silanol groups due to complete dehydration into Q^4 silica, i.e., all silicon atoms are then surrounded by four bridging oxygen atoms just as in bulk silica SiO_2 ($(-O-)_4Si$). In contrast, some cleavage planes of quartz and larger nanoparticles (> 100 nm size) can also feature up to two silanol groups per superficial Si atom; this structure ($(-O-)_2Si(OH)_2$) is then called Q^2 silica and has a maximum of 9.4 silanol groups per nm^2. In nanoparticles of several 100 nm size, the silanol density is often in between Q^3 and Q^4 [127,164,296]. Common techniques for surface characterization encompass measurements of the specific surface area (BET) and of weight loss upon heating from which the area density of silanol groups can be derived. Measurements of immersion energies, contact angles, adsorption isotherms, solid state NMR spectroscopy, infrared (IR) and Raman spectroscopy, X-ray photoelectron spectroscopy (XPS), as well as potentiometric titration and ζ-potential measurements also offer key insights into the surface chemistry and physics [126,284]. Potentiometric titration and ζ-potential measurements, in particular, are required to quantify surface ionization as a function of pH and ionic strength, and yields quantitative information on the characteristic area densities of cations and siloxide ions, respectively (Fig. 22d–h). The point of zero charge corresponds to the pH value of pure silanol termination (≡SiOH) without ionization to sodium siloxide groups ($\equiv SiO^- \cdots Na^+$) and lies between 2.5 and 4 for silica nanoparticles (Fig. 22h). Depending on silanol density, pH, particle size, and ionic strength in solution, up to 2.0 silanol groups per nm^2 can be ionized to sodium siloxide groups ($\equiv SiO^- \cdots Na^+$), before silica begins to dissolve around pH 8 to 9 (in most cases the ionization is less than 1.0 ($\equiv SiO^- \cdots Na^+$) groups per nm^2). These details of surface chemistry are essential to explain observed surfactant adsorption, selective binding, and ligand release. In addition, the porosity of nanoparticles or nanostructured surfaces plays a role in predicting adsorption, especially for pore sizes that are not significantly larger than the surfactants [297–299].

For titania nanoparticles [300], the point of zero charge (pzc) is somewhat higher at ~5.5 than that for silica at ~3.0 [301,302]. The higher point of zero charge for titania leads to somewhat less surface deprotonation at pH 7 in comparison to silica ($\equiv TiO^- \cdots Na^+$), and to positively charged protonated structures at pH values below 5.5 such as $\equiv TiOH_2^+ \cdots Cl^-$ groups.

For many other oxides such as indium tin oxide, alumina, iron oxides, zirconia, and ceria, quantitative evaluations of surface chemistry and influence of pH have not yet been available. Progress in this area, using both experiment and chemical knowledge/theory, holds great promise to enhance understanding of surface

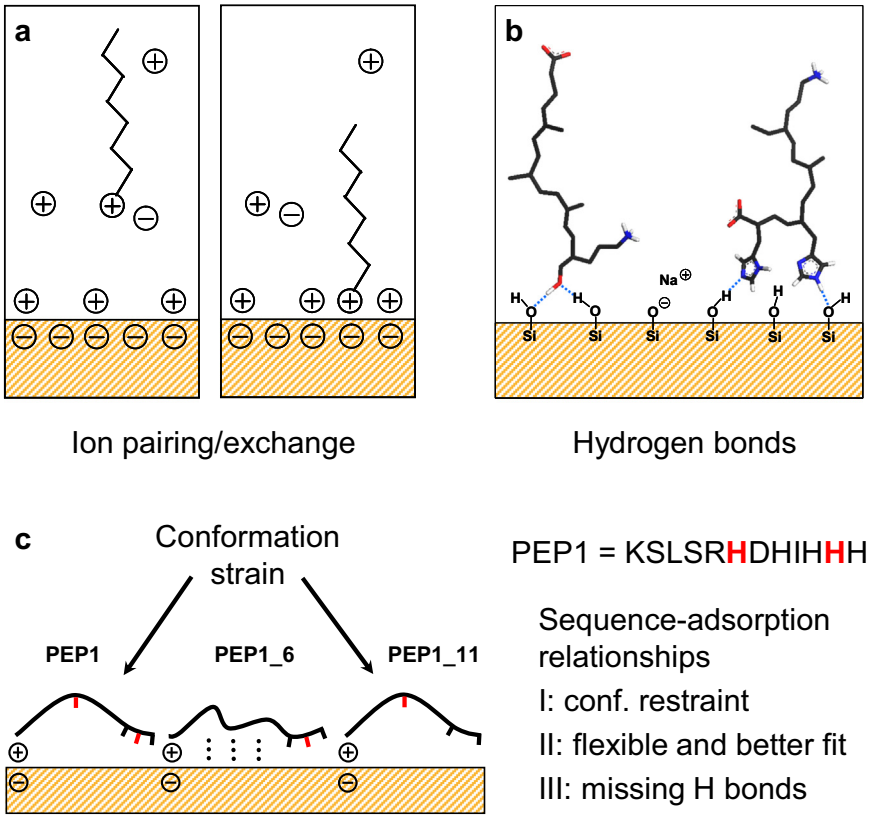

Fig. 23. Main contributions to adsorption of peptides onto silica surfaces. (a) Ion pairing and ion exchange. (b) Hydrogen bonds. (c) Conformation effects. Conformation analysis of a native 12-peptide PEP1 and two mutants on silica surfaces in experiment and molecular simulation shows that individual residues such as H6 can cause conformation strain that is relieved upon mutation to A6 in PEP1_6. Other residues such as H11 can be essential for binding through protonation and hydrogen bonds, which is no longer possible upon mutation to A11 in Pep1_11. Attraction of hydrophobic groups to the surface contributes to adsorption at low surface ionization, minimizing disruptions in the network of hydrogen bonds in the aqueous phase above the oxide substrate. (Adapted with permission from Ref. [126].)

modification and therapeutic applications of oxide nanostructures [126,303]. As a first approximation, known substance chemistry [304] as well as similarity considerations to acidic silica, amphoteric titania, and somewhat more basic alumina surfaces provide guidance for the extent of chemical equilibria between M–OH termination versus M–O–M bridges on the surface, as well as the likely extent of protonation and deprotonation equilibria ($\equiv MOH_2^+ \cdots Cl^-$ versus $\equiv MOH$ versus $\equiv MO^- \cdots Na^+$). Understanding of the interfacial chemistry is crucial to assemble molecularly designed materials from the nanoscale.

Decoration with surfactants, as well as nanocrystal growth and assembly, is determined by the presence of electric double layers of variable strength and charge density. For example, silica surfaces at pH 7 features the negatively charged oxide (siloxide, $\equiv SiO^-$) surface forming a double layer of negative zeta potential with coordinated and dissociated cations (Na^+) or positively charged surfactant head groups to maintain charge neutrality. On the other hand, at low pH values of 3 on titania, the surface layer consists of positively charged $\equiv TiOH_2^+$ groups and adjacent compensating anions such as Cl^- or anionic surfactants to complete the electric double layer. The surface chemistry and reactivity then also determines under which conditions covalent-cross links can be formed (Fig. 8) and remain stable [14,114].

4.1.2. Noncovalent binding mechanisms of surfactants

The noncovalent adsorption mechanism of surfactants to oxide surfaces involves ion pairing, ion exchange, hydrogen bonding, dipolar interactions, conformation effects, and hydrophobic interactions (Fig. 23). The difference between ion pairing and ion exchange is that ion pairing is an equilibrium process that reduces the observed ζ-potential by neutralizing the surface charge (Fig. 23a), whereas ion exchange is a substitution process with approximately constant ζ-potential, often followed by washing off the exchanged salts atop the surface, removing them from the equilibrium (see also Fig. 9).

In the case of silica, at pH values greater than 5 (greater than two units above the pzc), ion pairing to the negatively charged surface was found to be the dominant adsorption process for positively charged surfactants [126]. At the same time, hydrogen bonding between certain residues in the ligand, such as an alcohol group in a peptide side chain, and surface silanol groups adds to adsorption (Fig. 23b). The contribution of hydrogen bonds to adsorption increases towards the point of zero charge (lower pH) while ion pairing then decreases. Other dipolar interactions such as the complexation of cations pertaining to the surfactant (e.g. sodium acrylate polymers, potassium Asp and Glu residues in peptide surfactants) by negatively charged surface groups in the oxide support adsorption. For conformationally challenged molecules such as peptides and proteins, conformations contribute, too (Fig. 23c) [305], and removal of constraining groups can increase adsorption [126]. Conformation effects and their analysis can become very challenging for large polymers [306,307]. Finally, hydrophobic interactions were found to play a role [127,164]. Hydrophobic interactions dominate binding of noncharged surfactants to the surface, or binding of charged surfactants to a neutral surface (near pzc). Hydrophobic interactions in aqueous solution have also been described as a depletion effect as the ligands in solution may disrupt the hydrogen bonded network of water. Upon adsorption to the surface this disruption of hydrogen bonds in the liQ12quid phase is reduced, especially when both the ligand and the surface contain only few (or no) ionic groups with hydration shells. The “hydrophobic” adsorption mechanism also

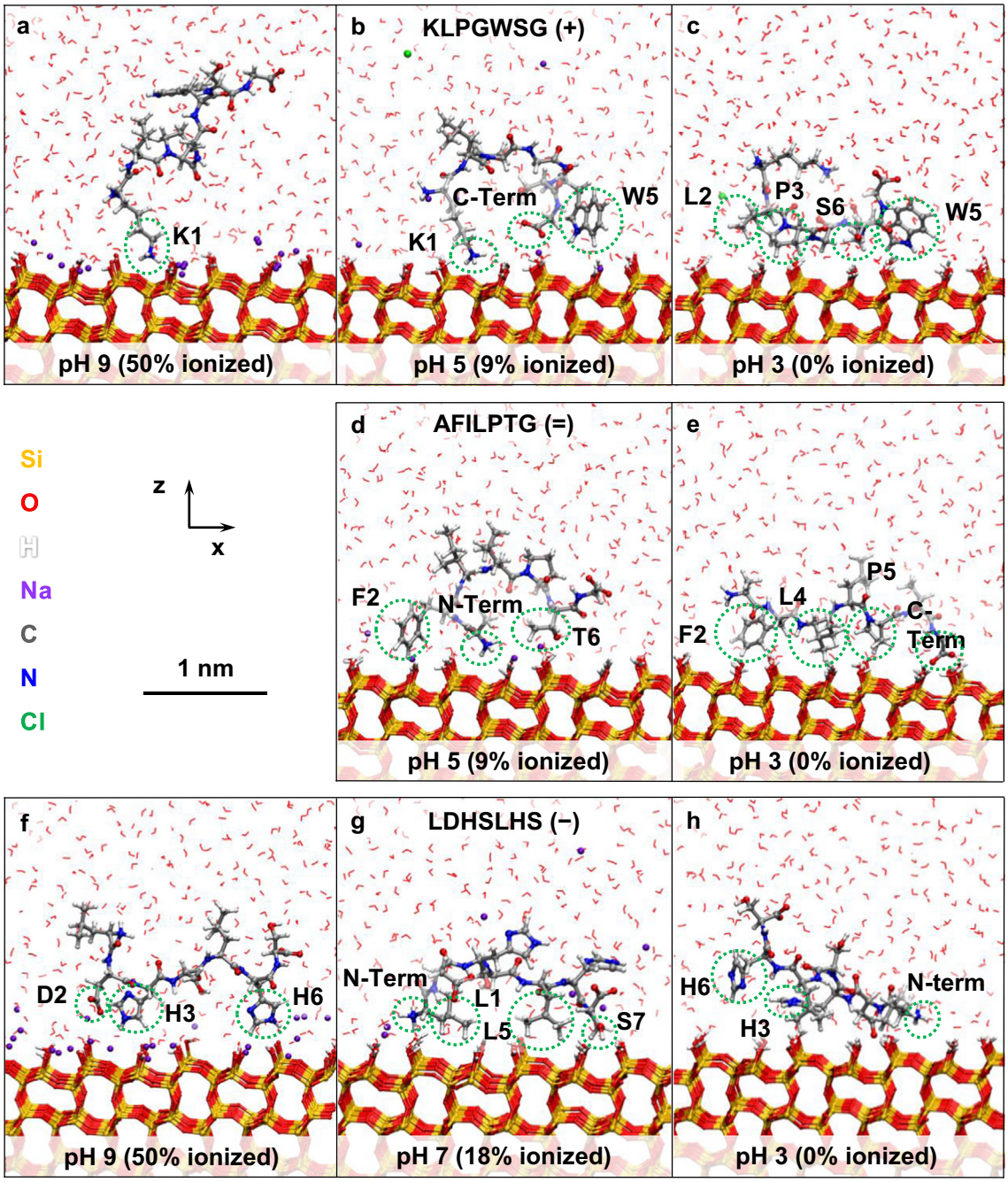

Fig. 24. Selected conformation of three peptides of different charge on Q^3 silica surfaces for a series of pH values according to molecular dynamics simulation in side view. The surfaces represent silica particles of 82 nm size with 4.7 SiO(H, Na) groups per nm^2 and pH dependent ionization that is implemented in the models in agreement with measurements (Ref. [284]). (a-c) The positively charged peptide KLPGWSG. (d, e) The overall neutral peptide AFILPTG. (f-h) The negatively charged peptide LDHSLHS. Amino acid residues with significant surface interactions are highlighted. Close contact with the surface as shown occurs between $>90\%$ of time (a) and 20% (f) of time depending on peptide affinity. (Reproduced with permission from Ref. [164].)

involves weak van-der-Waals interactions between the ligand and the surface, while often a depletion interaction is the actual driving force [164].

4.2. *pH-specific contributions to ligand adsorption*

The nonconvalent binding mechanism can be further illustrated for peptides of different charge in contact with silica (Figs. 24 and 25) [164]. The positively charged peptide KLPGWSG is more attracted to surfaces at higher pH when they carry a higher negative charge per unit area. On the 50% and 18% ionized Q^3 silica surfaces, that is, at pH 9 and 7, the peptide is anchored to the surface by the ammonium groups of the N-terminal and the K1 side chain for more than 80% of the time (Fig. 24a). At lower ionization of 9% and 0%, that is, at pH 5 and 3, electrostatic interactions through ion pairing are diminished and hydrogen bonds of the OH groups of residue S6 and of ammonium groups on N-terminal K1 with the silica surface increasingly contribute to adsorption (Fig. 24b and c). In addition, close contacts of L2, P3, and W5 side chains with the surface are seen. Hydrophobic residues have thereby no intrinsic affinity to the silica surface; their surface attachment mainly diminishes disruptions of the hydrogen-bonded structure of liquid water, equal to a reduction in excluded volume. Near-neutral silica surfaces, therefore, attract

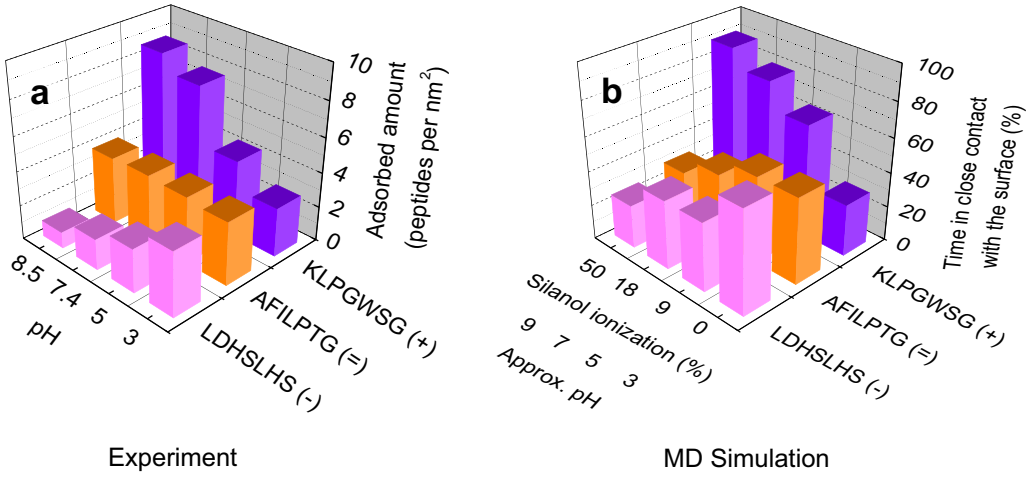

Fig. 25. Selective binding of peptides to silica surfaces by measurement and molecular dynamics simulation. Data are shown for nanoparticles of average diameter 82 nm with 4.7 silanol groups per nm^2 as a function of pH value. (a) Adsorbed amount of peptides of different charge as a function of pH at 1 mM initial concentration. (b) Percentage of time the same peptides spend in close contact with Q^3 silica surfaces of different ionization according to the simulation (< 3 Å). Near quantitative correlations are seen, including binding free energies (not shown). (Reproduced with permission from Ref. [164].)

hydrophobic residues to concentrate unfavorable hydrophobic (van der Waals) interactions directly at the surface. In contrast, hydration shells of siloxide ions and cations on notably ionized silica surfaces keep hydrophobic residues away. For these reasons, the time-averaged adsorbed conformation of the positively charged peptide KLPGWSG changes from anchor-like with strong contribution by ammonium groups on highly negatively charged surfaces (Fig. 24a and b) to flat-on arrangements with higher mobility and with more contact of polar and hydrophobic functional groups on less ionized surfaces (L2, P3, W5) (Fig. 24c).

Adsorption of the overall neutral peptide AFILPTG was weaker than for KLPGWSG and statistically not affected by changes in surface ionization and pH (Fig. 25). Interactions with the 50% ionized surface, which exceed the experimental surface charge, were found to be slightly more repulsive than in experiment. On all other surfaces, the peptide was in contact with the silica surface at least 40% of the time in molecular dynamics simulation through the N-terminal ammonium group by electrostatic forces (ion pairing) as well as through hydrogen bonds (Fig. 24d). Hydrogen bonds involve the carboxylate group of the C-terminal and the OH group in T6 in contact with surface silanol groups (Fig. 24d). Additional hydrophobic interactions were observed through the phenyl ring in F2, the L4 side chain, and the ring of P5 in agreement with experimental observations (Fig. 24e) [127].

The negatively charged peptide LDHSLHS showed less time in contact with most surfaces than the other two peptides and adsorption decreased with higher density of negative charge (Fig. 25). This peptide also notably changes its own charge from approximately -1.5 at pH 8.5 to $+2$ at pH 3 [296]. Direct contact with the highly ionized surface at pH 8.5 amounted to only 20% of simulation time (Fig. 24f) and increased to above 40% of simulation time for 18% and 9% ionized silica surfaces, respectively (Fig. 24g). The N-terminus of L1 and hydroxyl groups in S7, as well as some hydrophobic groups approach the surface at lower pH. At the point of zero charge, the peptide is in close contact with the surface for more than 60% of simulation time, including protonated H3, H6, and temporarily all residues (Fig. 24h).

These studies illustrate molecular-level insight into the highly specific interactions between biomolecular ligands and silica [164]. The results also explain earlier experimental and theoretical observations [126,308–310]. Differences in the surface chemistry of silica nanoparticles of different origin and processing were found to be so substantial that combinatorially selected silica-binding peptides exhibit less than 20% sequence similarity at comparable pH and ionic strength [75,310–312]. Sequence similarity approaches randomness (5%) when the pH value was changed in addition [127,296]. Specific consideration of surface chemistry, morphology, and ionization for a given type of silica and conditions in solution is therefore essential. The same considerations apply for other, yet less well studied oxides, such as titania, carbonates, and apatites that exhibit a similar diversity of surface environments [15,120]. The diversity of surface chemistry of oxides is in stark contrast to the simple surface chemistry of precious metals which, as a result, attracts similar peptide sequences (see Section 3) [121,122,130,209,220,313,314].

4.3. Covalent modification of oxide surfaces

Covalent modification of oxide surfaces can be achieved using silanes, phosphonates, carboxylates, catechols, alkenes, and amines (Fig. 8) [114,115]. The critical surface feature are reactive metal-hydroxyl groups such as ≡Si-OH and ≡Ti-OH. Hydrophilic silica surfaces can be rendered hydrophobic by these techniques, for example, and multiple new surface-terminating groups can be introduced via successive modification (post-grafting) using bifunctional linker molecules. For example, silicate glass surfaces can be first treated with piranha solution (7:3 mixture of H_2SO_4 and H_2O_2) to activate the surface silanol groups, and leach out other oxide components in the glass such as sodium oxide. Then, octadecyldimethallylmethylsilane can be grafted onto the silanol terminated surface to create a highly hydrophobic surface (Fig. 26a) [114].

Indium tin oxide (ITO) glass can be pre-treated in the same way and then modified with the same ligands; here an example of ferrocene-bearing ligands is shown (Fig. 26a). The resulting ferrocene-functionalized glass with specific redox properties was tested as an electrode in phosphate-buffered aqueous solution using cyclic voltammetric (CV) measurements. The surface functionalization allows conductive ITO electrodes to be modified for photovoltaic and organic electronic applications.

Another common multistep process of covalent surfactant grafting begins with the grafting of an N-hydroxysuccinimide ester (NHS-ester) onto a silica substrate, which subsequently could be used to immobilize glucose oxidase and produce a biosensor (Fig. 26b) [315]. As a result, mesoporous silica balls bearing a covalently immobilized enzyme with a high loading rate were obtained compared to conventional multistep grafting methods.

Silica nanoparticles have also been modified using controlled radical polymerization, including atom transfer radical

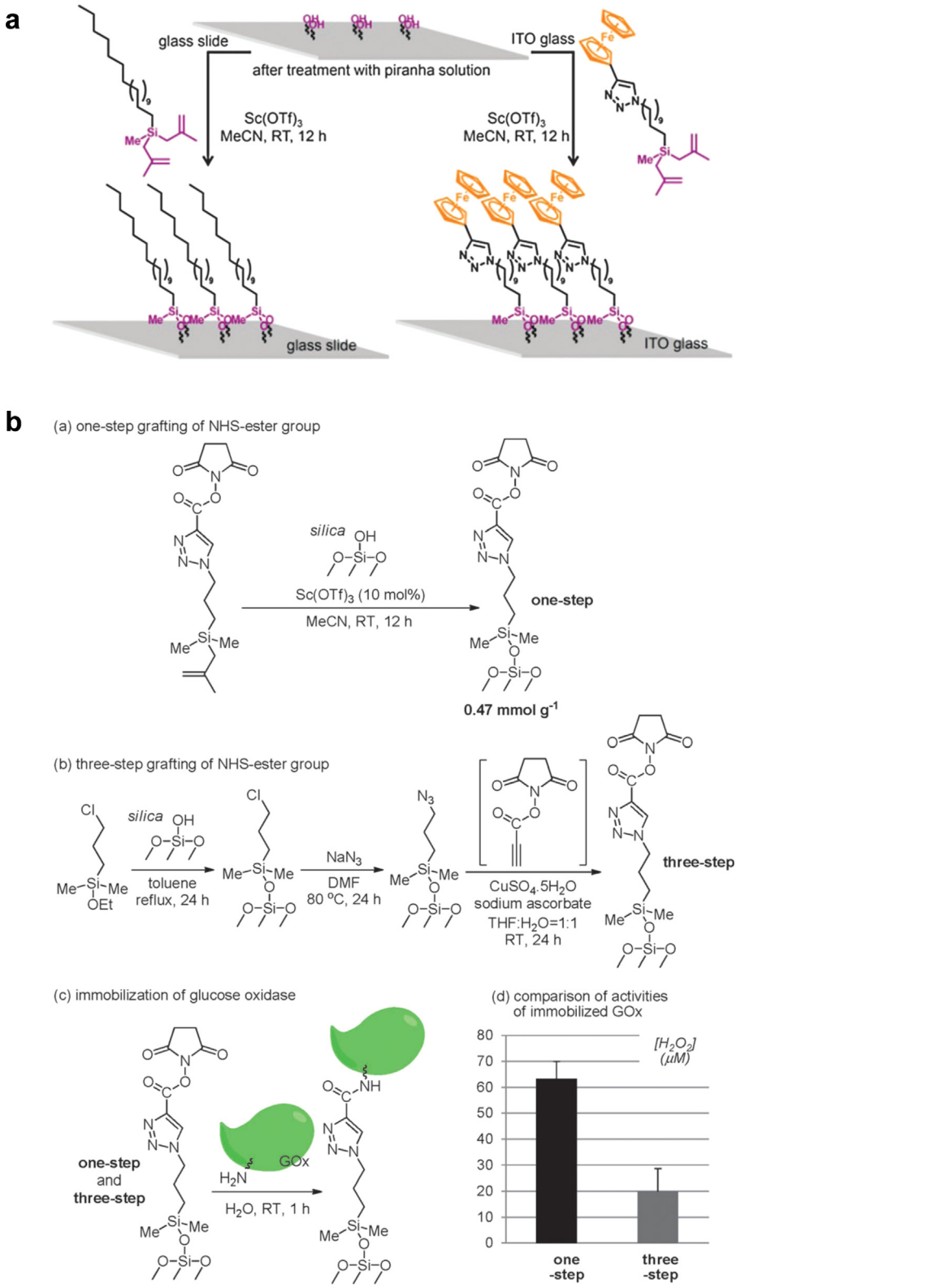

Fig. 26. Advanced covalent surface modification of silica and ITO glass for electrode materials and bioconjugation. (a) Surface modification of glass slide and ITO glass for photovoltaic applications using the 2-methylallylsilane protocol. (b) Immobilization of glucose oxidase (GOx) onto N-hydroxysuccinimide ester (NHS-ester) functionalized silica via one-step and multi-step methods. The silica surface serves as a carrier for glucose oxidase. The activity of the modified silica nanoparticles is higher after the one-step process. (Reproduced with permission from Ref. [114].)

polymerization (ATRP), nitroxide-mediated polymerization (NMP), and reversible-addition-fragmentation chain transfer polymerization (RAFT) [189]. Through the use of new RAFT agents and coupling agents, the graft density, and thereby the packing density, can be controlled from 0.01 to ~0.7 chains/nm^2 and brushes of molecular weights up to 150 kg/mol with a dispersity index below 1.15 could be obtained [316]. Functionalization typically starts with a bifunctional amine silyl ether, and the RAFT agent is then

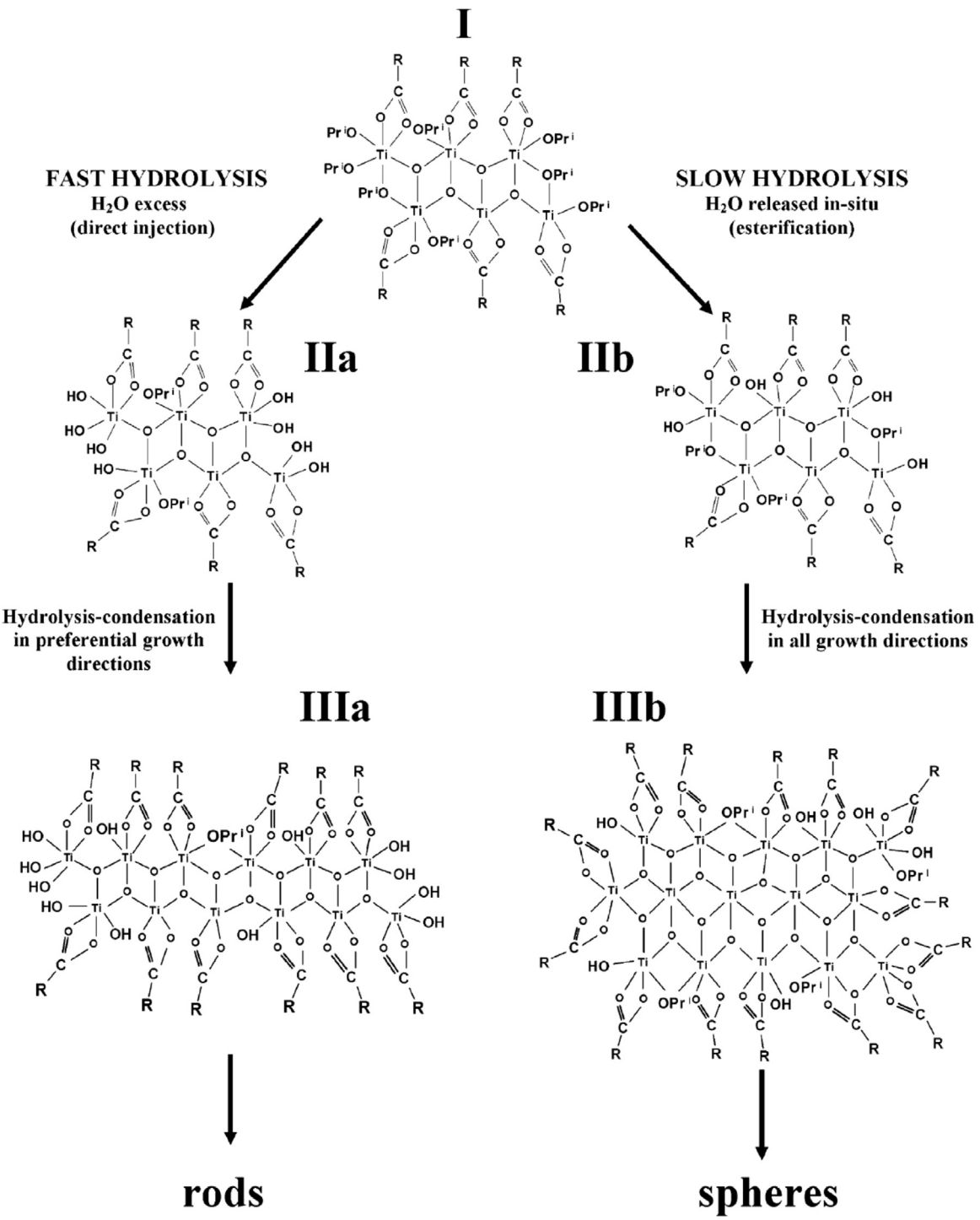

Fig. 27. Likely growth mechanism of titania in oleic acid as a pure solvent into anisotropic products (route a) and into isotropic products (route b) (–OPr^i=–CH(CH3)2 and R=alkyl chain of oleic acid). (Reproduced with permission from Ref. [320].)

attached to the amine-modified silica surface to begin the polymerization reaction.

Lee et al. further reported surfactant-templated syntheses of magnetite-silica core-shell nanoparticles [317]. The nanoparticles were then amine-functionalized, reacted with glutaraldehyde and with the enzymes lipase and α-chymotrypsin for covalent attachment (CA). The bifunctional aldehyde enables further cross-linking of the enzyme-modified nanoparticles. Such crosslinking of enzyme clusters (CEC) in various nanomaterials results in synergetic enzyme stabilization and improves the apparent enzyme activity due to the high loading [318]. The high enzyme activity in nanoparticle-based crosslinked enzyme clusters has begun to be exploited in the biosynthesis of chemicals, pharmaceuticals, and commodity catalysts. The ability to separate the nanoparticles by application of a magnetic field thereby eases recycling and automation of biocatalysis.

Silica nanoparticles were also encapsulated in polystyrene using a combined noncovalent/covalent grafting mechanism [319]. The silica nanoparticles were first treated with oleic acid that binds non-covalently to the silica surface via hydrogen bonds (Fig. 23). Then, the C=C bonds of oleic acid were copolymerized with styrene monomer through bond addition. The resulting

polystyrene-coated silica nanoparticles (~200 nm size) can be better dispersed in polymer matrices than pure silica due to a lower interfacial tension.

4.4. Surfactant-directed growth of oxide nanoparticles, nanowires, and porous nanostructures

The synthesis of oxide nanoparticles from soluble precursors is widely used, for example, using tetraesters of silicic acid in the presence of ammonia [298,299]. The silica nanoparticles with negative surface charge (Fig. 22) can then be non-covalently modified with CTA^+ surfactants that form a spherical micelle-like shell around the nanoparticle [297]. Deposition of further mineral precursors (tetraethylorthosilicate, tetrabutyl titanate) then leads to their assembly between the silica core and the CTA^+ shell, followed by mineralization and growth of core-shell nanoparticles. This protocol can be used to synthesize SiO_2-TiO_2, Fe_2O_3-TiO_2 and other core-shell oxide stoichiometries.

Surfactants can also be used to direct the growth kinetics and shape of nanoparticles starting at the nucleation stage [320–325]. The growth and aspect ratio of anatase TiO_2 by hydrolysis of titanium tetraisopropoxide (TTIP) can be controlled by the use of oleic acid as surfactant (Fig. 27). Tertiary amines or quaternary ammonium hydroxides were used as catalysts to promote fast crystallization, and chemical modification of TTIP by oleic acid was employed to tune its reactivity toward water. Slow hydrolysis lead to thermodynamically favored, spherical titania nanoparticles. Fast hydrolysis, in contrast, lead to growth in preferential directions and the formation of titania nanorods as a kinetically favored product. The synthesis of the organic-capped anatase TiO_2 was also possible using different capping ligands, for example, to achieve high solubility in both apolar and polar solvents [320].

A classic example of surfactant-directed assembly is the templated growth of oxide nanostructures (Fig. 28) [318,323,324,326–328]. First, surfactants above the critical micelle concentration organize into micelles or other aggregate structures, and then soluble oxide precursors are added. The precursors subsequently mineralize onto the template and form a solid oxide around the surfactant template. For example, when cylindrical micelles are used that pre-order in a hexagonal array, tetraalkyl silicates or other oxide precursors form a cylindrical silica shell (or other oxide shell) after deposition and hydrolysis (Fig. 28a). Subsequently, the surfactants can be removed by calcination to form mesoporous silica. Chiral mesoporous silica has been synthesized using chiral surfactants that assemble into chiral micellar templates [329]. Thereby, the definition of "mesopores" is a size range of 2–50 nm. In comparison, "micropores" are defined in a size range of 0–2 nm and "macropores" larger than 50 nm (this common terminology conflicts with the actual nanometer-scale size).

An alternative method leading to the same mesoporous structure is the use of surfactants that assemble into a liquid crystal upon addition of solvent (lyotropic liquid crystal) (Fig. 28b). Asymmetric triblock copolymers can also be used and function as more advanced surfactants (Fig. 28c). For example, the copolymer PS-b-PVP-b-PEO assembles into micelles that then internalize oxide precursors such as titanium tetraisopropoxide (TTIP) in a controllable way. The structures are ultimately calcined as in classical surfactant-templated synthesis to eliminate the block copolymer, solidify the oxide, and yield a mesoporous oxide. The techniques using lyotropic liquid crystals and triblock copolymers have been applied to produce mesoporous silica, titania, Ta_2O_5, Al_2O_3, Nb_2O_5, and mixed oxides [324]. Mesoporous nanoparticles

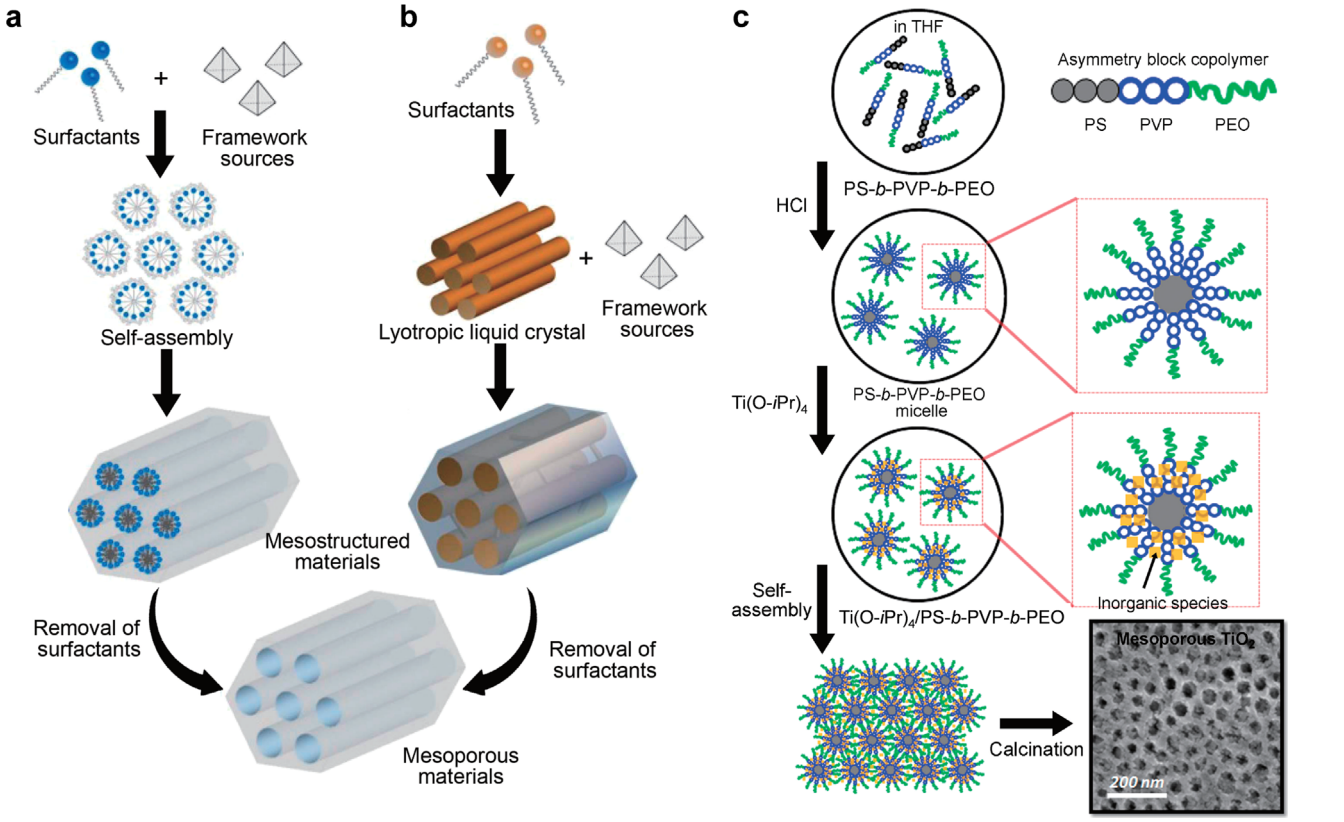

Fig. 28. Use of surfactant, liquid crystals, and block copolymer templates to assemble soluble oxide precursors into mesoporous materials (e.g., silica, titania, alumina). (a) Classical surfactant based cooperative self-assembly route. (b) Classical surfactant based lyotropic liquid crystal templating route. (c) Formation mechanism of mesoporous TiO_2 through a micelle assembly process by using the asymmetric triblock copolymer PS-b-PVP-b-PEO and titanium tetraisopropoxide (TTIP) precursors. Other compositions such as Ta_2O_5, Nb_2O_5, and mixed oxides can also be prepared. (Adapted with permission from Refs. [323,324].)

are used for many applications, including drug delivery, MRI contrast agents, sensors, and electrode materials in batteries [66,70,279,330–335].

In a similar fashion, ZnO nanowires and nanotrees have been hydrothermally grown from soluble $Zn(OAc)_2$ and $Zn(NO_3)_2$ precursors in the presence of hexamethylenetetramine and polyethylene imine surfactants (Figs. 29 and 30) [325]. Starting with seed nanoparticles, the surfactants act as capping agents and enable anisotropic growth. Length grow can be repeated to reach high aspect ratios in excess of 100 (Fig. 29a–c). Polymer removal and addition of further seed crystals also enables branched growth and the steps can be repeated (Fig. 29d and e). The resulting nanotrees and nanoforests from such hybrid growth (Fig. 30) offer a very high surface area that enables dense dye loading and improved light harvesting when used in dye sensitized solar cells (DSSCs) [325,336]. ZnO-polyvinylpyrrolidone films (PVP films) have also been used in dithienogermole–thienopyrrolodione-based polymer solar cells [337]. The growth mechanism is not yet fully understood down to the molecular scale. Therefore, rational predictions of aspect ratios and nanostructures, other than directly from experimental trials, are still a challenge.

4.5. Optical and electronic properties of surfactant-modified oxide nanoparticles, quantum dots, and applications

Interactions of titania surfaces with organic dye molecules are critical for the performance of dye sensitized solar cells (DSSCs) (Fig. 31) [338]. In Gratzel cells, a ruthenium-bipyridyl dye absorbs light and forms electron-hole pairs aided by charge transfer to titania. The positive charge is typically retained by the Ru dye and its binding affinity to the oxide surface determines the transport efficiency of negative charge to the titania electrode (Fig. 31a). The

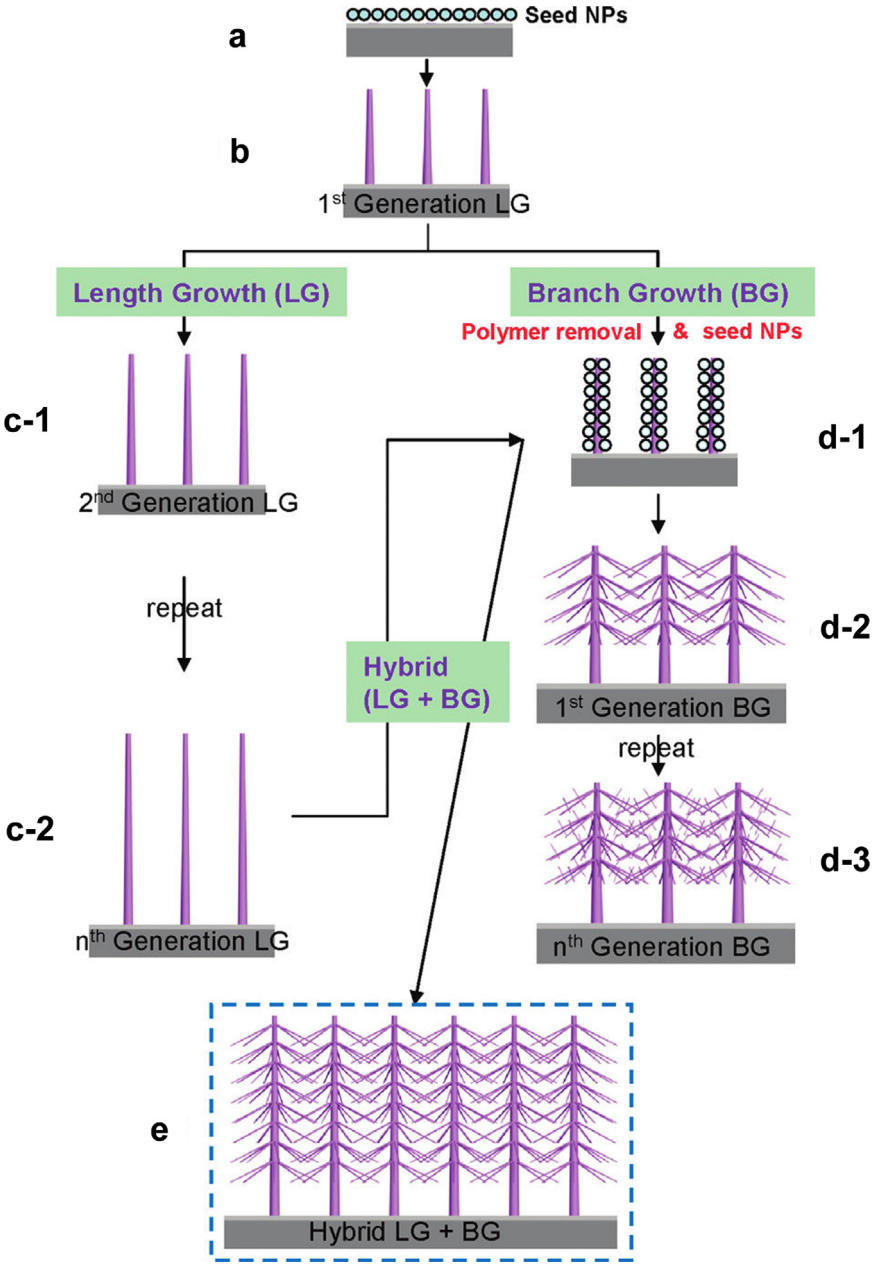

Fig. 29. Two routes for hierarchical ZnO nanowire hydrothermal growth into nanotrees and nanoforests. Hexamethylenetetramine and polyethyleneimine (PEI) were used as capping agents to enable anisotropic growth. Length growth (LG) (a-b-c), branched growth (BG) (a-b-d), and hybrid growth (a-b-c-d-e). Notice polymer removal and introduction of seed nanoparticles to achieve branched growth. (Reproduced under the Creative Commons Attribution license from Ref. [325].)

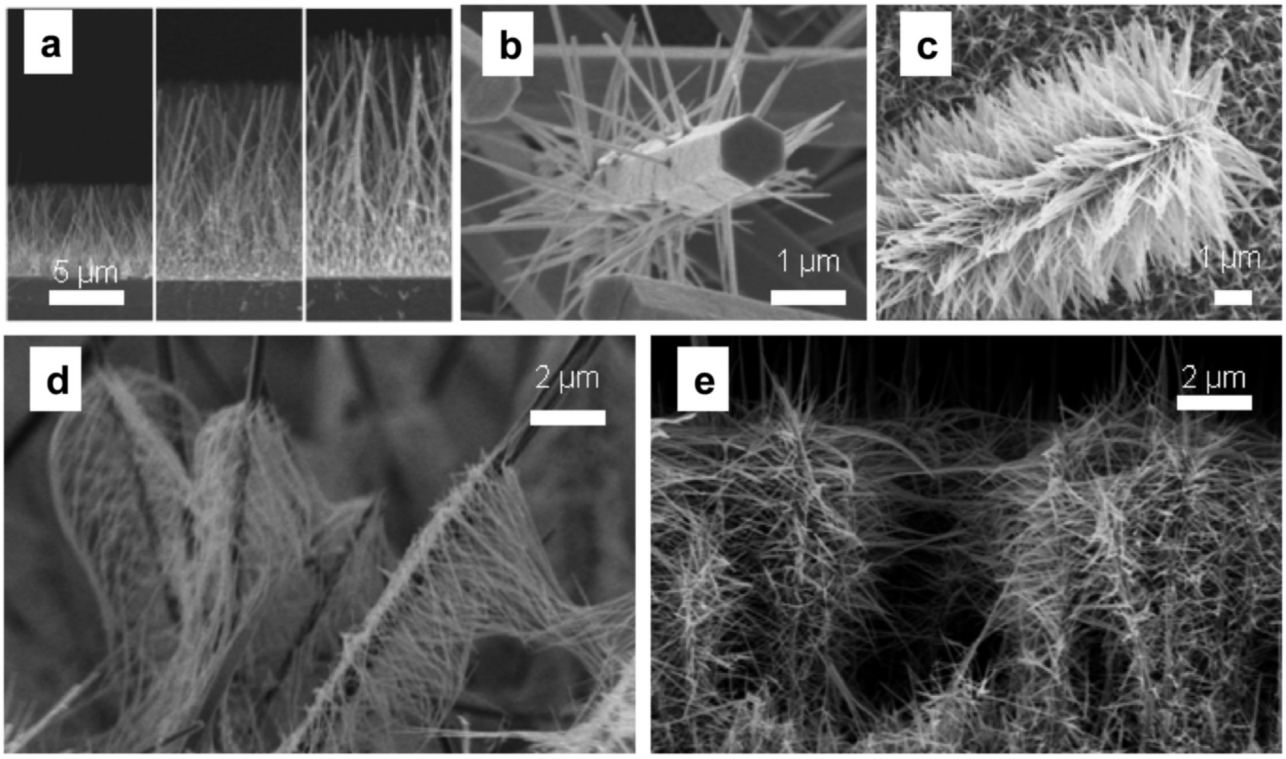

Fig. 30. SEM images of ZnO nanowires for applications in dye sensitized solar cells. (a) Length growth (1, 2, 3 times growth). (b, c) Seed effect: first generation branched growth (b) without seeds and (c) with seeds after polymer removal. (d, e) Polymer removal effect: first generation branched growth (d) without polymer removal and (e) with polymer removal after seed NP deposition. Polymers on ZnO nanowires are removed after 350 °C heating for 10 min. (Reproduced under the Creative Commons Attribution license from Ref. [325].)

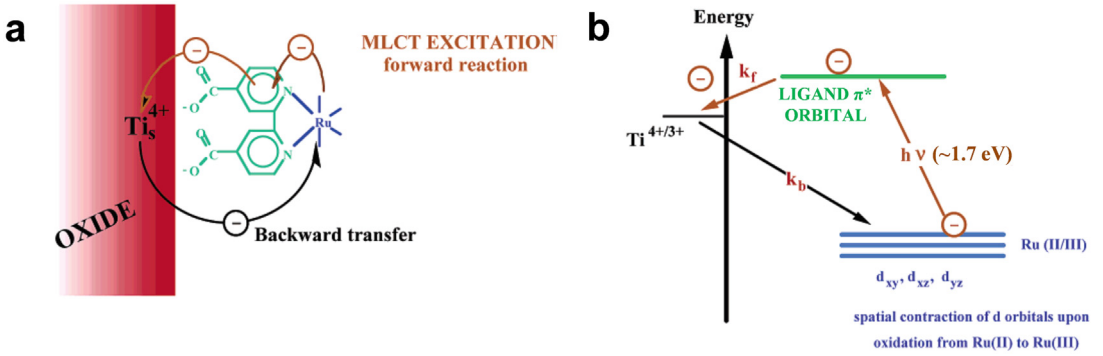

Fig. 31. Surface modification of titania by ruthenium dyes in dye-sensitized solar cells. (a) A ruthenium complex binds to the surface of TiO_2 via a carboxylated bipyridyl ligand. Upon exposure to sunlight, a metal-ligand charge transfer (MLCT) excitation initiates interfacial electron transfer towards titania, which is in contact with an electrode. (b) Orbital diagram for the forward electron injection (rate constant k_f) from the π^* orbital of the bipyridyl ligand into the empty t2g orbitals forming the TiO_2 conduction band and the backward electron transfer from the conduction band of the oxide into the Ru(III) *d* orbitals. (Adapted with permission from Ref. [338].)

electron in the excited state in the π^* orbital of the ligand is transferred into the conduction band of TiO_2. A competing process is the backward transfer of the electron from the titania electrode into the ground state orbital of the ligand, leading to charge recombination. The efficiency of the process depends significantly on the chemistry and on the arrangement of the dye molecules on the surface [339]. Many alternative ligands have been synthesized that are reminiscent of porphyrins, however, only some of them enable the desired high power conversion efficiency of dye-sensitized solar cells [340]. Natural dyes such as bacteriorhodopsin have also been employed [274]. More recently, perovskites were discovered as solid-state replacements for the electrolyte, allowing significantly higher power conversion efficiencies on the order of 20% [341,342]. However, the relationship between the chemical structure of the dye (or perovskite), binding preferences to the mineral electrode, associated electronic structure, and photovoltaic performance remain largely empirical. Further mechanistic studies supported by measurement and realistic simulations at the 1–10 nm scale may provide specific guidance in the future.

The electronic structure of mineral interfaces plays a major role also for properties of quantum dots such as ZnS, ZnSe, ZnTe, CdS, CdSe, and CdTe (Fig. 32) [134]. Solutions of CdTe and CdSe capped with aminoethanethiol, for example, exhibit temperature-dependent UV adsorption characteristics and colors (Fig. 32a). The band gap of various metal chalcogenides, phosphides, nitrides, and arsenides is primarily controlled by the chemistry and associated electronic structure (Fig. 32b), and can be further modified and fine-tuned by specific surface-adsorbed ligands [343,344]. Surfactants can have also been grafted to the nanoparticle surfaces to introduce new functionalities (Fig. 32c). Van der Waals, electrostatic or covalent interactions with the surrounding surfactant

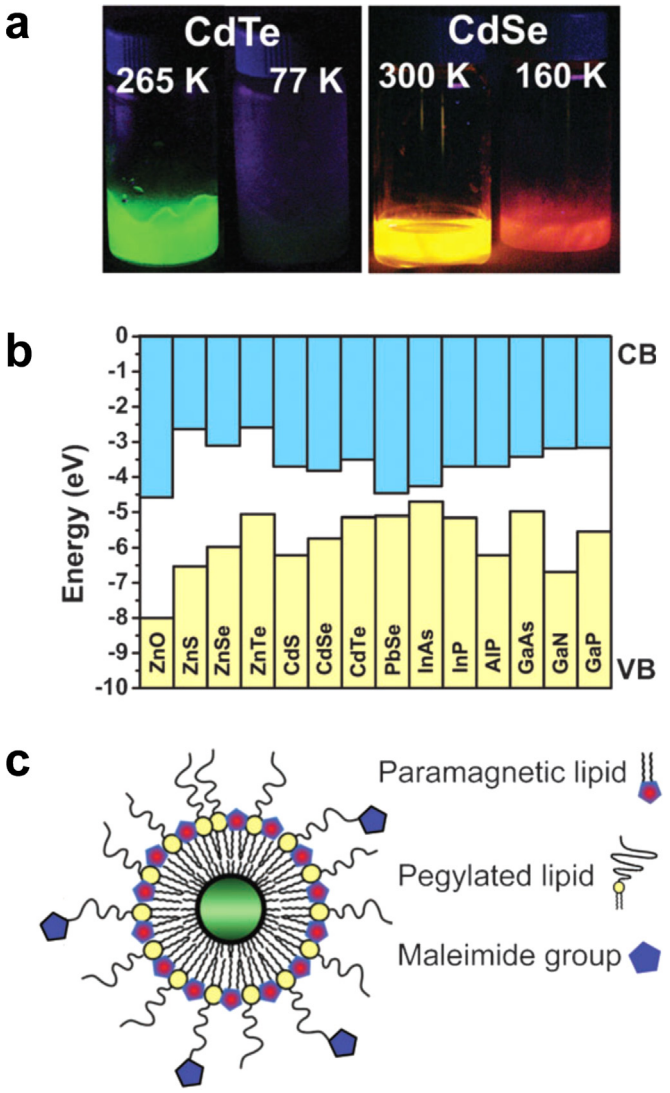

Fig. 32. Quantum dots (QDs), associated band gap, and attachment of nanolabels for medical imaging. (a) Left panel: Vials containing an aqueous solution of CdTe QDs capped with aminoethanethiol under UV (365 nm) illumination at the temperatures indicated. Right panel: Solutions of colloidal CdSe QDs in toluene under UV (365 nm) illumination at the temperatures indicated. The luminescence temperature anti-quenching effect is evident in both cases, since the photoluminescence intensity is dramatically reduced upon cooling. (b) The energy of the electronic band edges relative to the vacuum level of selected semiconductors (VB: valence band, CB: conduction band). The space between the solid bars gives the band gap. Values for bulk materials are given, except for PbSe, which are estimated from nanocrystal results. (c) Schematic representation of a nanolabel for bimodal biomedical imaging (optical and MRI), obtained by self-assembly of a multifunctional lipid monolayer around an organically capped CdSe/(Cd,Zn)S/ZnS core/multishell colloidal QD. (Adapted with permission from Ref. [134].)

layer can be utilized to assemble new molecules around the colloidal nanocrystals, thereby introducing new recognition elements and modified properties. For example, van der Waals interactions between lipid molecules and an octadecylamine coating layer in CdSe/(Cd,Zn)S/ZnS core/multishell (CSS) QDs have been successfully used to self-assemble a multifunctional lipid monolayer around the QD, yielding nanolabels for bimodal biomedical imaging. The CSS core/multishell QDs retain their efficient photoluminescence, allowing the detection of the biolabels by optical imaging techniques [134]. Further inclusion paramagnetic Gd^{3+} ions in the lipids renders them efficient contrast agents for magnetic resonance imaging. Solubility in water is maintained by the use of PEGylated lipids (PEG = polyethylene glycol), while lipid molecules with a maleimide head are used to covalently bind biorecognition molecules (Fig. 32c). This approach was also used to produce octadecanol coated silica NPs with properties of CSS QDs [134].

Upon such surface modification, the grafting density of surfactants is not always well known (Fig. 33). Studies using ICP-AES, NMR, TGA, and XPS have been able to quantify the number of ligands attached to the surface of various nanoparticles (Fig. 33a) [345]. The corresponding packing density can reach values close to 1.0 (about 5 alkyl chains per nm^2) yet is often clearly below (see Fig. 3 for definition of the packing density). The structure and thermal behavior of the surfactants follows the description in Section 2, whereby the curvature of the nanoparticle leads to more conformational disorder of the surfactants as the distance from the immediate QD surface increases (Fig. 6). Measurements of electron transfer from the surface of CdSe quantum dots modified with mercaptocarboxylic acids to a polyviologen matrix confirmed the presence of a collapsed ligand shell (Fig. 33b and c). The packing density right on the surface corresponds to about $\lambda_0 \sim 0.8$ (~ 4 carbon chains per nm^2) and less in the outer region (see Section 2.3). Gauche conformations were found to be present, explaining the observed tunneling barriers consistent with Marcus theory. Quantum dots modified with surfactants have also been applied in solar cells as an attachment to TiO_2 films [346]. Chemical composition and assembly of the surfactants affect the efficiency and photostability of the quantum dots.

4.6. Applications as therapeutics and diagnostics

Oxide, chalcogenide, and chemically similar nanoparticles are used as diagnostics and therapeutics ("theranostics") (Fig. 34) [279]. For example, iron oxide nanoparticles contain Fe_3O_4 (Fig. 34d) and the superparamagnetic core allows the nanoparticles to be tracked using magnetic resonance imaging (MRI) [347]. Chemical modification on the surface of each type of nanoparticle is similar in that protective ligands, such as PEG, are tethered to the nanoparticles' surfaces to prolong the bioavailability of the nanocarrier. Other surface modifications include appending targeting ligands, such as folic acid, and drug conjugated polymers to enhance biodistribution and uptake as well as stimuli-responsive release of a drug or oligonucleotide, respectively [279]. Iron oxide nanoparticles are often produced as core-shell nanoparticles with a silica shell which promotes biocompatibility and enables standard surface functionalization (Figs. 8, 23, and 26). Aminosilane-modified magnetite nanoparticles have been employed for treatment of cancer using Magnetic Fluid Hyperthermia (MFH) [348]. The uptake of the nanoparticles by glioblastoma cells was found to be 10-fold higher than by normal glial cells at a dose of about 10 mg ferrite/g tumor, and leading to visible pigmentation.

Pristine silica nanoparticles are also common carriers (Fig. 34f) [66]. Post-synthetic grafting can introduce functional groups mainly to the exposed silica surface, before or after surfactant removal. Besides covalent attachment, functional moieties can also be introduced to mesoporous silica nanoparticles through electrostatic interactions, making use of the negative charges from the free $\equiv SiO^-$ groups on the particle's surface (Figs. 22 and 23). Cationic polymers (such as polyethyleneimine) can be electrostatically adsorbed onto the silica nanoparticles to provide nucleic acid binding properties [349]. Another crucial property that makes mesoporous silica materials promising for drug delivery applications is the ability to encapsulate different types of cargo molecules within their pore channels. This is important as encapsulation can protect therapeutic agents from enzymatic degradation. The particles are usually loaded by soaking them in a drug solution, and the drug molecules are incorporated into the particles

a

quantum dot	radius (nm)	ligand	ligands/nm^2	technique
CdSe	1.8–3.4	octylphosphonic acid and condensate	$\langle 11 \rangle^{a,b}$	ICP-AES
PbSe	1.5–3.5	oleic acid	$\langle 4.2 \rangle^{a}$	^{1}H DOSY
CdSe	1.08	TOP(O,Se)	$\langle 1.09 \rangle^{a}$	^{1}H NMR
CdSe	1.84	TOPO	0.57	TGA
CdSe	0.93–3.02	TOPO	3.0	XPS
PbS	1.7	oleic acid	4.4 ± 0.8	^{1}H NMR
PbS	1.55	decanethiol (87%)/oleic acid (13%)	5.0 ± 0.8	^{1}H NMR

[a] Brackets indicate an average value. [b] Ligands are incorporated into a multilayer Cd-phosphonate "polymer", rather than a monolayer, in this system.

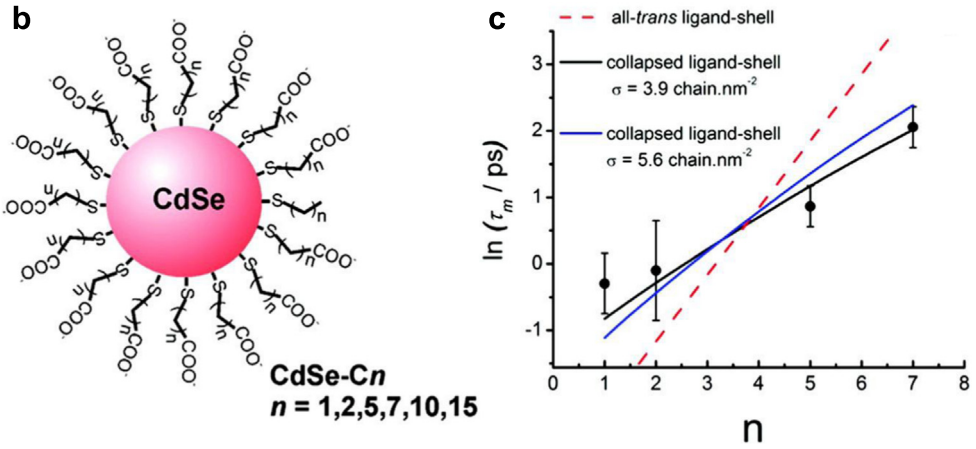

Fig. 33. Typical grafting density of ligands onto quantum dots (QDs) and an example of photoinduced charge transfer. (a) Number of ligands per unit area on the surface of quantum dots for different ligands, types, and sizes of quantum dots. TOPO=trioctylphosphine oxide. (b) Schematic of CdSe QDs with mercaptocarboxylic acid ligands of various length as an example. (c) The ligands act as a tunneling barrier against photoinduced electron transfer from CdSe QDs (donor) to a polyviologen matrix (acceptor). Marcus theory predicts an exponential decrease in charge transfer rate with increasing separation distance between donor and acceptor. Measured charge transfer rates as a function of the ligand-length (black data points) are consistent with a collapsed ligand shell due to nanoparticle curvature and high packing density (~4 carbon chains per square nanometer and packing density $\lambda_0 \sim 0.8$ at the immediate QD surface; packing density down to $\lambda_0 < 0.5$ at the outer surface). An alternative model describing electron tunneling through a rectangular barrier of the width expected for a ligand shell with all-anti conformation yields a poor fit with experimental data (red dashes). (Adapted with permission from Ref. [345].) (For interpretation of the references to color in this figure legend, the reader is referred to the web version of this article.)

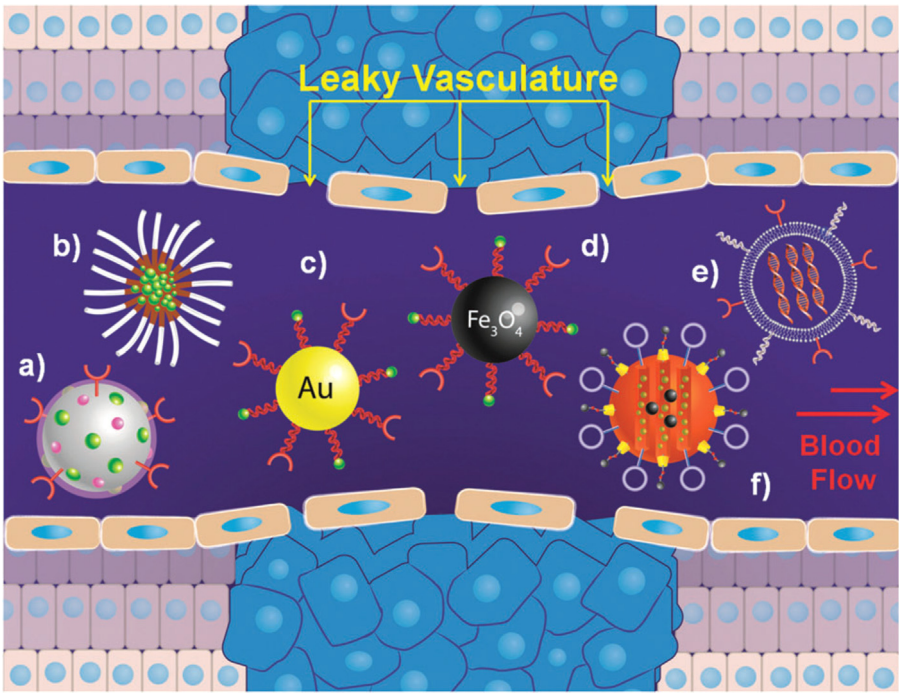

Fig. 34. Diagnostic and therapeutic ("theranostic") applications of nanoparticles including metals, oxides, and polymers. Various types of theranostic nanomedicines are depicted in "attack mode" over a site of tumor growth in this cartoon representation. Conjugated targeting ligands are shown as circles or semi-circles. Cargo, conjugated or housed internally, is shown as green spheres. Purple spheres represent imbedded contrast agents. (a) Multifunctional polymeric nanogel. (b) Polymeric micelle. (c) Gold nanoparticle. (d) Iron oxide nanoparticle. (e) siRNA ensconced in a liposome delivery vector. (f) A stimuli-responsive capped mesoporous silica nanoparticle. (Reproduced with permission from Ref. [279].) (For interpretation of the references to color in this figure legend, the reader is referred to the web version of this article.)

through adsorption. The interactions between the cargo molecules and the particle often include electrostatic and other dipolar interactions such as hydrogen bonding (Fig. 23). The uptake capacities of the mesoporous silica nanoparticles are correlated with the specific surface area of the materials [350]. Loading and release efficiencies of the particles are corresponding to the noncovalent binding energy and their contributions as described in Section 4.2. for peptides. When combined with the functional surfactant modifications on the mesoporous silica nanoparticles, payloads can be released in a controllable fashion at the targeted diseased tissues, with no premature release during their circulation within the bloodstream [65]. More sophisticated surface modification in this manner can significantly reduce adverse side effects of drugs and increases the overall therapeutic efficacy.

5. Surface modification of 2D layered nanostructures

Two-dimensional layered nanomaterials have become of great interest for various applications [137], including electrode materials for batteries and fuel cells [271,351,352], sensors [141,353], nanoelectronics and dielectric building blocks [354,355], hydrogels [356], as well as fillers in polymer nanocomposites [341,357–361]. In this section, first the functionalization and selective binding of ligands to graphitic materials will be discussed, including applications to sensors and composites. Second, the dispersion of transition metal chalcogenides and control of crystal growth by means of surfactants is reviewed along with applications in electrode materials. Then, surface modification and reversible swelling of layered transition metal oxides is described for the example of layered titanates in detail. Last, the well-studied surface modification of clay minerals and layered double hydroxides are described, including an analysis of surfactant dynamics, and implications for property enhancements in polymer nanocomposites and supercapacitors.

5.1. Graphene-based nanomaterials

Graphene is the allotrope of carbon that can be present in the form of individual graphene layers, fullerenes, carbon nanotubes, and graphite (Fig. 35a) [136,362]. A wide variety of different 3D structures [363], [m, n] nanotubes with different numbers of walls [364], and stacked graphenes have been synthesized and applied in polymer solar cells, fuel cells, batteries, supercapacitors, including N-doped and B-doped structures with tailored conductive and semiconductor properties [365–367]. Covalent chemical functionalization can be employed at the edges, on the basal plane, and asymmetrically on both sides of the basal plane (Fig. 35b). In addition, noncovalent adsorption and self-assembly of functionalized graphene sheets into superstructures are important means to direct bottom-up assembly. Unlike edge modification, covalent functionalization of the graphene basal plane can cause significant distortion of the π conjugation and associated physicochemical properties. However, the graphene basal plane structure remains largely unchanged with noncovalent functionalization by adsorption.

Covalent functionalization of the pristine graphene sheet is very difficult, if not impossible, due to poor solubility. Therefore, a popular starting material for the functionalization of graphene are solution-processable graphene oxide (GO) sheets that contain reactive carboxylic acid groups at the edge and epoxy as well as hydroxyl groups on the basal plane (Fig. 35c) [136]. Graphene oxide is derived from the solution oxidation of graphite with strong oxidizing reagents, for example, HNO_3, $KMnO_4$, and/or H_2SO_4 [368].

The reactivity of GO allows the covalent grafting of peptides, thiols and gold nanoparticles, silica nanoparticles and a wide range

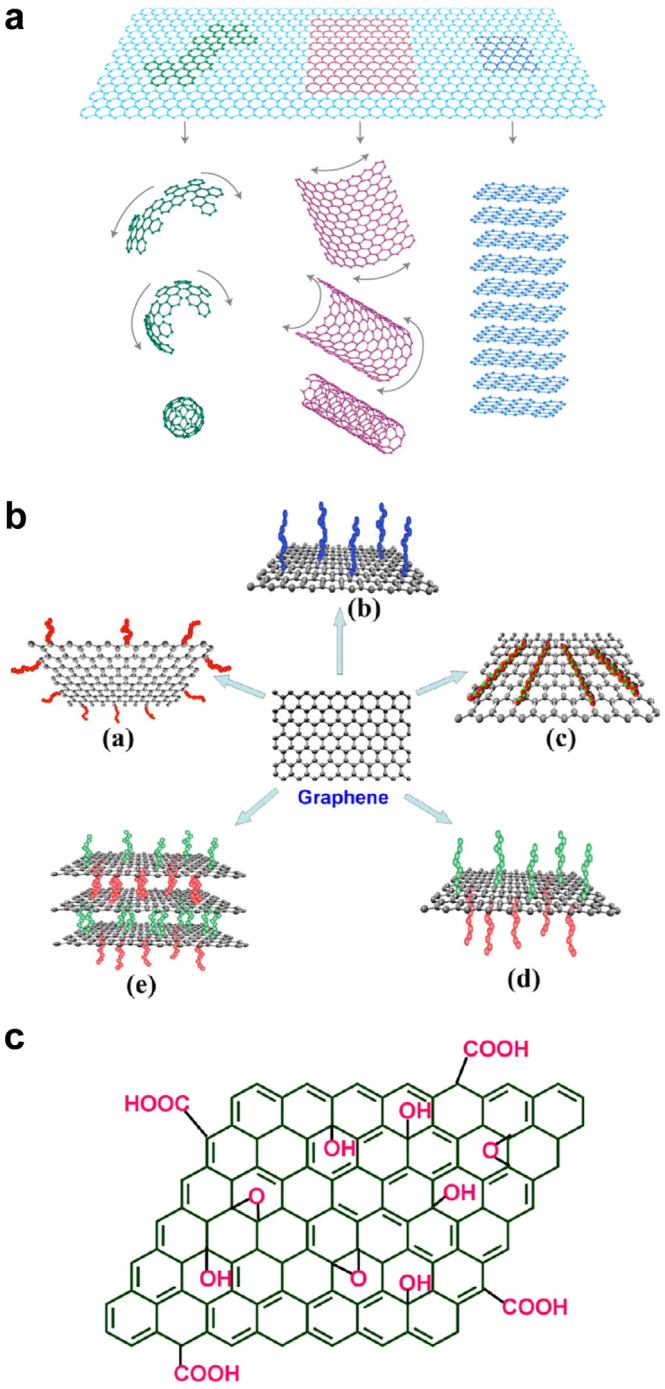

Fig. 35. Graphene-based layered materials. (a) Graphene and its relation to fullerenes, carbon nanotubes, and graphite. (b) Functionalization possibilities for graphene: (a) edge-functionalization, (b) basal-plane-functionalization, (c) noncovalent adsorption on the basal plane, (d) asymmetric functionalization of the basal plane, and (e) self-assembly of functionalized graphene sheets. (c) Chemical structure of graphene oxide. (Adapted with permission from Refs. [136,362].)

of other polymers and nanostructures [369–372]. Yet also inert pristine graphene has been successfully applied to intercalate oxide and metal nanoparticles in the presence of surfactants [258,352,373]. Graphene was also directly grown on metal surfaces using chemical vapor deposition [374].

Noncovalent binding of peptide ligands to graphene, graphite, and CNT nanotubes has been explored by phage display (Fig. 36)

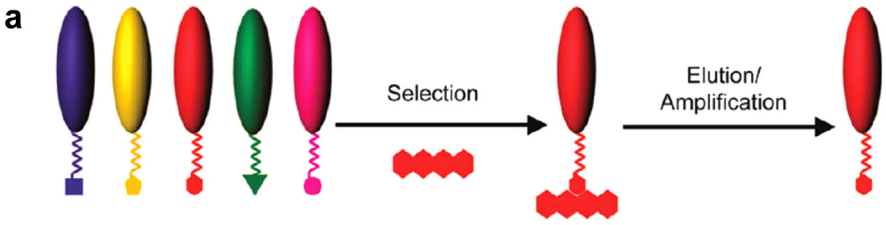

b Phage displayed peptides binding to graphite/graphene

	Heptamer	pI	Dodecamer	pI
SLP30	EPLQLKM (GBP1)	6.1	TMGFTAPRFPHY (GBP2)	8.44
	QQQLSTH (GBP3)	6.74	YHRMPQALSAME (GBP4)	6.76
HOPG	no consensus		GAMHLPWHMGTL	6.92
N006	no consensus		GAMHLPWHMGTL	6.92

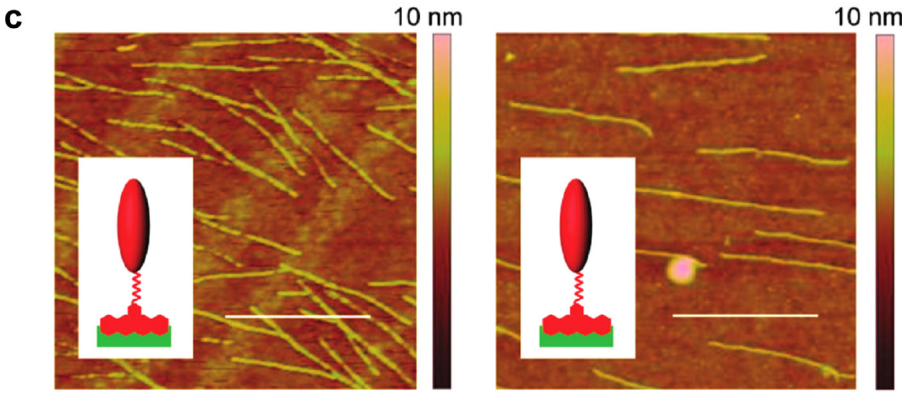

Fig. 36. Identification of peptides derived from phage display as binders to graphene/graphite flakes via non-covalent adsorption. (a) Schematic illustration of the generalized screening protocol to identify phage displayed peptides which recognize graphene/graphite flakes. (b) Summary of consensus graphene binding peptides (GBPs) to various graphene/graphite flakes. (c) AFM images of bacteriophages displaying GBP1 7-mer (left) and GBP2 12-mer (right) peptides binding to graphene (scale bars 1 μm). (Adapted with permission from [375].)

[375–377], similar to combinatorial peptide selection on other substrates like metals and oxides [75,217,222]. The technique involves combinatorial screening of about a billion different bacteriophages with the substrate of interest such as graphene, graphite, and CNTs [378,379]. The various phages in the library display cilia at the surface of the capsid that terminate with randomized amino acid sequences (Fig. 36a). Some of these sequences are binding stronger and are determined after several washing cycles. The analysis of strongly bound peptides by amplification and sequencing then reveals the order of amino acids (Fig. 36b and c). The peptide sequences attracted to graphene and graphite have some similarity, for example, the amino acids M, L, Q, H, P, T occur multiple times, as well as Y, E, S, and A (ranked in order). In comparison, CNT binding peptides are rich in T, H, S, Y, W, A, as well as in N, P and F (ranked in order) [377]. The amino acids T, H, S, Y, A, and P are in common, as expected due to the similarity of the carbon materials and a certain randomness in combinatorial peptide sequences attracted to the same type of graphitic substrate. There is no obvious dominance of π stacking interactions, although all aromatic residues (H, F, Y, W) are part of the strongest binding sequences. The binding also appears to involve alcohol side chains of T and S, as well as nonpolar residues such as P and A.

Atomistic modeling and simulation has emphasized the role of hydrophobic and π stacking residues, even though common force fields do not reproduce cation-π and π-stacking interactions [125,376,380–382]. Therefore, conclusions about binding mechanisms are somewhat preliminary. From a standpoint of chemical knowledge and theory, however, it is certain that graphitic substrates exhibit multipole moments and remarkably strong cation-π interactions due to the presence of π electrons (in excess of 20 kcal/mol in vacuum) [124,383]. It is less clear, however, how organic functional groups in solution interact with the surface and to which extent these interactions affect molecular recognition (Fig. 37). It has been shown that computed binding energies of amino acids by DFT calculations in vacuum and with force field based calculations to-date are in good agreement [384]. Nevertheless, the relative position and registry of aromatic ligands with respect to the graphene-like substrate upon adsorption is not consistent among current force fields, and might also depend on the chosen density function in DFT. Therefore, the structure of graphitic interfaces with organic ligands is still uncertain, especially in the presence of competing solvent molecules and ions in solution.

In the following, two applications are highlighted. ssDNA-modified graphene oxide has been used as a molecular-beacon-like probe for multiplex sensing of targets such as sequence-specific DNA, protein, metal ions and small molecules [144,353]. The sensitivity and selectivity of the biosensor towards Ag^{+} and Hg^{2+} was tested in presence of Mn^{2+}, Pb^{2+}, Mg^{2+}, Fe^{3+}, Ca^{2+}, Cu^{2+}, Ni^{2+}, Zn^{2+}, Co^{2+}, Cd^{2+}, and Al^{3+}, each at a concentration of 10

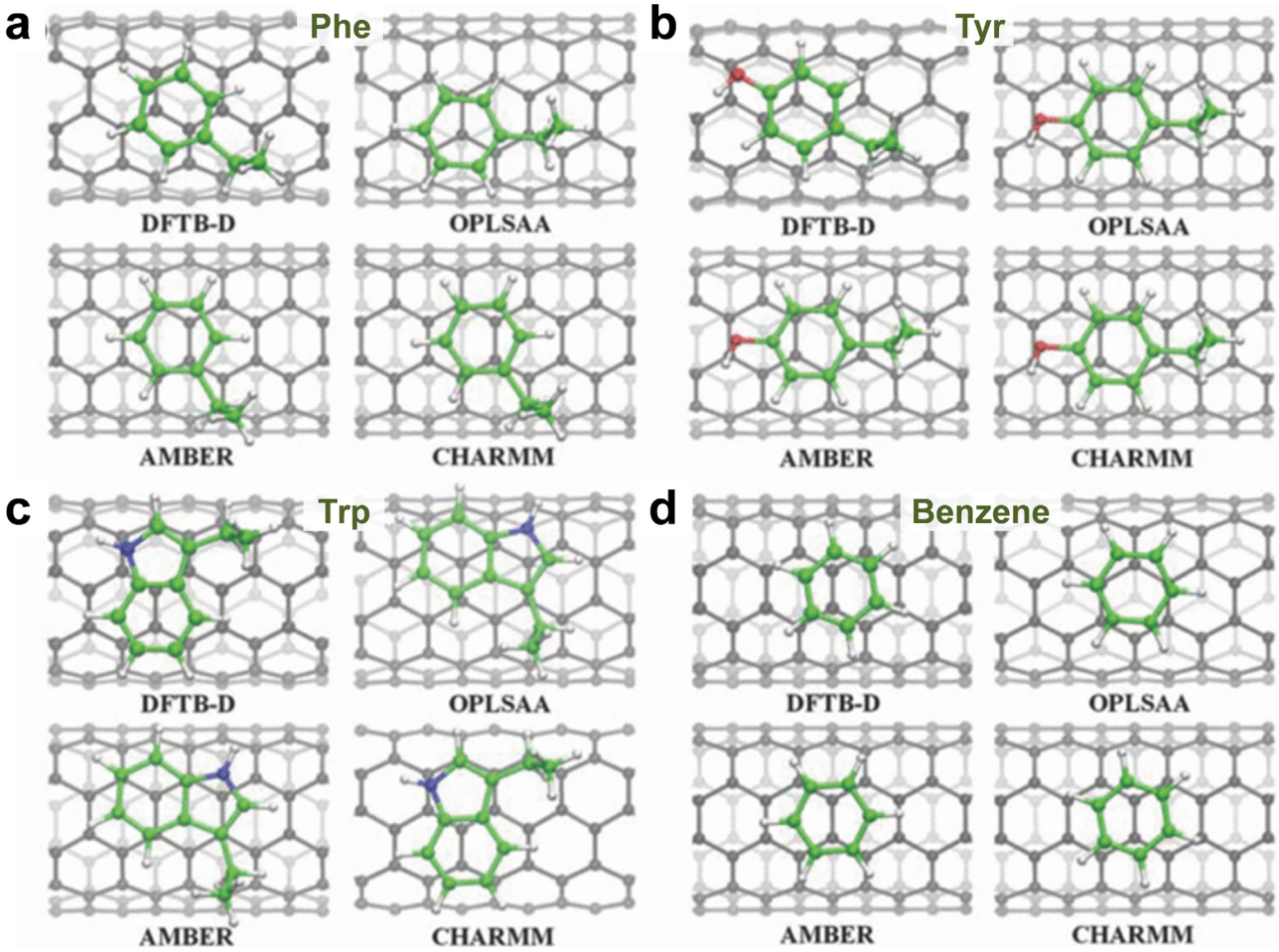

Fig. 37. Snapshots of the equilibrium structures of aromatic molecules binding to a (5,5) single wall carbon nanotube in vacuum predicted by quantum mechanical and classical atomistic simulation methods. (a) Phe. (b) Tyr. (c) Trp. (d) Benzene. "Flat" configurations of minimum energy are shown in top view. The true registry of aromatic rings atop the CNT (or other graphitic) surfaces is most likely to correlate with DFT results while current force fields do not include π-stacking interactions and yield random orientations. Computed binding energies, nevertheless, agree between DFT and force field methods (-7 to -13 kcal/mol depending on molecule size). (Reproduced with permission from Ref. [384].)

μM (Fig. 38). The surface modified graphene sensor demonstrates very high selectivity towards Ag^{+} and Hg^{2+} ions over the alkaline earth and heavy transition metal ions. The detection limit is less than 0.05 μM in each case.

Functionalized graphene sheets were also shown to be effective fillers in polymer nanocomposites that affect mechanical and thermal properties [359,385]. Surface termination of graphene by carboxyl groups and other reaction sites involved in oxidation and reduction processes yields a wrinkled sheet structure of the functionalized graphene of high surface area and polarity that still retains its conductivity (Fig. 39). Interfaces of the functionalized graphene with polymethylmethacrylate (PMMA) are well integrated in three dimensions and display graphene-polymer contacts with high interfacial area (Fig. 39a and b). In comparison, PMMA interfaces with exfoliated graphite are composed of thicker stacks of graphene layers without a continuous 3D interfacial region (Fig. 39c). As a result, Young's modulus, glass transition temperatures, ultimate tensile strength, and threshold temperatures for thermal degradation are significantly increased for the functionalized graphene-PMMA composites relative to the equivalent exfoliated graphite-PMMA composites (Fig. 39d). Improvements in mechanical and thermal performance of functionalized graphene composites also exceed that of single wall carbon nanotube (SWCNT)-PMMA composites [359].

Graphene and graphene-derived graphitic structures can be produced in large quantities and are therefore exploited for a plethora of applications. Alternative layered materials with unique functional properties are also being explored, such as transition metal chalcogenides, layered oxides, clay minerals, and layered hydroxides (see following subsections). An recent example is black phosphorus that allows tuning the band gap, optical absorption spectrum, and anisotropic polarization energy window across a wide range by controlling the number of atomic phosphorene layers included in the stack [386].

5.2. Transition metal chalcogenides

Transition metal chalcogenides such as (Mo, W, Nb, Ta)(S, Se, $Te)_2$ exhibit semiconductor properties and are therefore of interest as part of electronic and thermoelectric devices, catalysts, electrode materials, and sensors [370,387–390]. The sub-nanometer thin layers expose mostly hydrophobic surfaces and are insoluble in water. Non-covalent adsorption of amphiphilic surfactants can render the surfaces hydrophilic (Fig. 40). Dispersion of the otherwise insoluble stacked layers in water was achieved using sonication in the presence of SDS, CTAB, sodium cholate, and taurodeoxycholate surfactants [391,392].

MoS_2 was shown to grow into porous flower-like structures upon hydrothermal synthesis from ammonium heptamolybdate and thiourea in the presence of ethylenediaminetetraacetic acid (EDTA) as a surfactant, whereas dense spheres were obtained without the surfactant (Fig. 41) [393]. EDTA acts as a strong

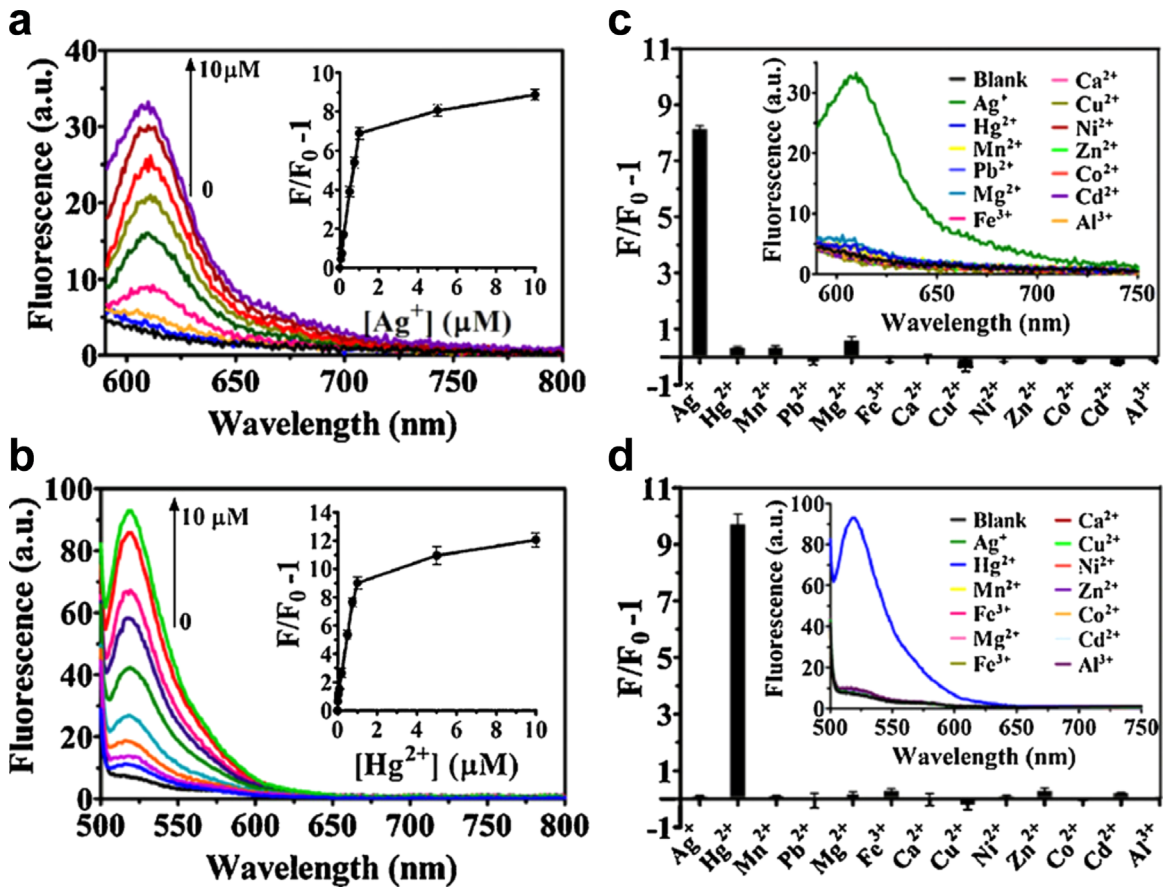

Fig. 38. Selective and sensitive multiplex sensors for metal ions (Ag^+ and Hg^{2+}) using ssDNA-modified graphene oxide. (a, b) Fluorescence response to Ag^+ and Hg^{2+} ions. The fluorescence emission spectra are shown for various ion concentrations of 0, 0.02, 0.05, 0.1, 0.2, 0.5, 0.75, 1.0, 5.0 and 10.0 μM. Insets: Plots of $(F/F_0 - 1)$ as function of the metal ion concentrations. (c, d) Selectivity analysis for the detection of Ag^+ and Hg^{2+} ions. (Reproduced with permission from Ref. [353].)

chelating agent and the disodium salt functions as a ligand to inhibit the growth along the (0 0 l) direction. CTAB surfactants exhibited a similar effect [391]. The dense MoS_2 spheres are hypothesized to evolve from the porous MoS_2 flowers through growth along the $<0\ 0\ l>$ direction of the nanosheets (Fig. 41a and b). Based on this growth mechanism, the microstructure of MoS_2 can be controlled by adjustment of the S/Mo ratio and addition of a surfactant in the recipe. Electrochemical measurements demonstrate that the flower-like MoS_2 shows better electrochemical performance than MoS_2 spheres as anode materials for Li-ion batteries, including a high reversible capacity of 900 mA h g^{-1} at a current density of 100 mA g^{-1}, excellent cycling stability, and rate capability.

Highly effective electrode materials consisting of layered MoS_2/graphene composites were also prepared using L-cysteine as a surfactant [394]. Sodium molybdate, $Na_2MoO_4 \cdot 2H_2O$, graphene oxide, and cysteine were used as starting materials in the hydrothermal solution synthesis at 240 °C, whereby cysteine functions as a reducing agent for the molybdate, as a sulfur source, and as a growth directing ligand [394]. The resulting wet MoS_2/graphene products were processed into composites upon annealing under H_2/N_2 at 800 °C. It was then observed that the incorporation of the graphene considerably inhibited the growth of MoS_2 crystals in the composites, especially in the (002) plane of MoS_2 during hydrothermal processing and annealing. Further addition of CTAB surfactants in this protocol showed that the Li^+ ion storage capacity was increased (Fig. 41c) [370]. The increase in CTAB concentration also leads to a decrease in the layer number of MoS_2 sheets. For example, the graphene-like MoS_2 sheets in the composites are few-layer in the case of 0.01 to 0.03 mol l^{-1} CTAB in the hydrothermal solution and single-layer in the case of 0.05 mol l^{-1} CTAB. The best reversible capacity of 940–1020 mA h g^{-1}, greater cycle stability, and a higher rate capability as an anode material in batteries were identified for the few-layer samples (Fig. 41c(b)).

Transition metal dichalcogenides have also found applications in transistors [387], as catalysts for hydrogen generation upon functionalization of edge sites [395], and sensors [396]. For example, a thin MoS_2 nanoparticle film on a glassy carbon (GC) electrode could be directly used as a H_2O_2 sensor with a detection limit of 2.5 nM. Similarly efficient MoS_2-based glucose sensors have been prepared by immobilization of glucose oxidase on a MoS_2 nanoparticle film on a GC electrode using drop-casting at a loading of 0.2 mg cm^{-2}, and protection of the modified electrode with a thin Nafion layer.

5.3. Layered transition metal oxides

Transition metal oxides also form layered materials with interesting optical and electronic properties [354–356,397–401] Iron substitution in titania, for example, leads to layered titanates such as $H_{0.8}[Ti_{1.2}Fe_{0.8}]O_4 \cdot H_2O$ with high defect density and large cation exchange capacity (Fig. 42a) [398]. Upon reaction with amines such as dimethylaminoethanol or tetrabutylamine, protonation of the amines in the interlayer space by the TiOH-bound hydrogen atoms leads to giant reversible swelling of the layered material up to 100-fold its initial volume and layer spacing (Fig. 42b). The likely reason for the reversible swelling is the high density of charged sites on the surface of ~3.1 per nm^2 per exposed surface area on both sides of the titanate layers. This high area density of

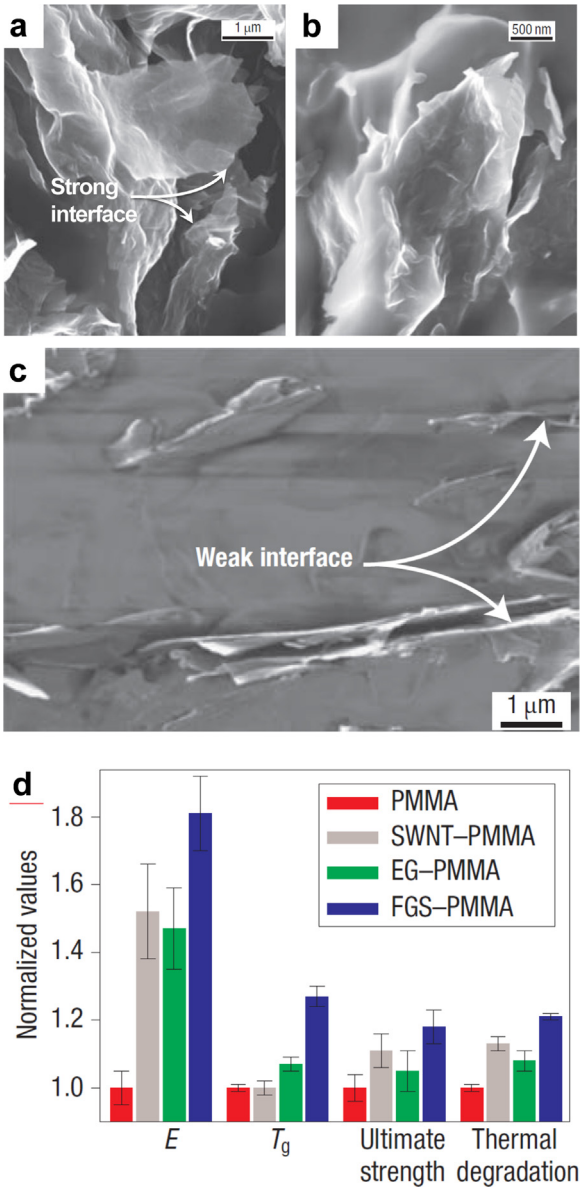

Fig. 39. The wrinkled nature of functionalized (oxidized) graphene sheets (FGS) and improvements in polymer composite properties. (a, b) SEM images of an FGS–PMMA composite fracture surface revealing the subsurface morphology of FGS and the presence of strong 3D interfaces (at high acceleration voltage of 6–10 kV). The persistent wrinkled nature of the FGS within the composite provides for better interaction with the host polymer matrix. (c) Topographical scanning electron micrograph of an exfoliated graphite (EG)–PMMA composite fracture surface obtained under 3 kV acceleration voltage. The simple expanded graphite exhibits thicker protruding plates (as opposed to exfoliated nanosheets) with poorer bonding to the polymer matrix. (d) Property improvements for 1 wt% nanoparticle–PMMA composites, comparing neat PMMA, 1 wt% SWNT–PMMA, EG–PMMA, and FGS-PMMA composites. All property values are normalized to the values for neat PMMA and thus relative to unity on the scale above; averages are calculated over five samples each and error bars for standard deviation are shown. Values for neat PMMA are Young's modulus E ~2.1 GPa, glass transition temperature T_g ~105 °C, ultimate tensile strength ~70 MPa, thermal degradation temperature ~285 °C. (Adapted with permission from Ref. [359].)

cations, which is about 50% more than on muscovite mica (Section 5.4), leads to electrostatic repulsion among the large ammonium ions and drives them off the surface into solution depending on the degree of the protonation reaction. In contrast, before the addition of amine, the acidic hydrogen atoms are covalently bound to oxygen on the titania nanosheets, or closely in proximity, so that the charge density is not felt and the layers remain stacked on top of each other. The structure of the swollen layers that expand into striped structures can be seen in optical microscopy (Fig. 42c and d). Similar swelling behavior and specific interactions with amine surfactants have also been observed for defective, iron free titanate layers of the composition $H_{1.08}Ti_{1.73}O_4$ (or $[Ti_{1.73}(H_{0.27})_4]O_4$) in which some of the titania is replaced by 4 hydrogen atoms to form additional TiOH groups. The titanate structures have been tested as anisotropic hydrogels [356] and might also find applications in photosensitizers, photonic crystals, conducting oxide nanostructures, and actuators.

Other transition metal oxides such as molybdates, tungsten oxides, and lanthanide oxides exhibit similar layered structures [355,399]. Layered niobates, in particular, have been examined by modification with surfactants, rolled into nanoscrolls, and surface-modified with proteins, polymers and dyes [397].

5.4. Clay minerals

Clay minerals are abundant in soil and comprise a number of chemically diverse layered aluminosilicates, for example, kaolinite, pyrophyllite, montmorillonite, laponite, veegum, and muscovite mica (Fig. 43) [1,18,41,402]. Clays have been among the nanomaterials on which first systematic studies of ion exchange and surfactant modification have been performed (Section 2). Neat and surface-modified clay minerals are used in drilling fluids, polymer/clay nanocomposites, paints, coatings, hydrogels, and cosmetics. Swellable clay minerals such as montmorillonites exhibit thixotropic properties in solution, and well dispersed nanometer-thick layers in polymer/clay nanocomposites increase the mechanical stability, reduce the gas permeability, and improve electrical insulating properties at filler fractions in the low or sub-percent range [40,403–406].

Clay minerals have a plate-like structure that is a sequence of a rigid, bonded layers, and a non-bonded, more flexible interlayers containing alkali or earth alkali cations (Fig. 43). In 2:1 layered silicates, alkali or earth alkali cations are located in between rigid, bonded aluminosilicate layers, leading to a thickness of approximately one nanometer per vertical repeat. One rigid bonded layer thereby consists of two outer silicate sheets and one inner aluminate (or magnesium-containing) sheet, which are covalently interconnected, therefore called 2:1 layered silicates. Examples are muscovite and biotite micas, montmorillonite, laponite, pyrophyllite, and talc. The cations are electrostatically bound to the interlayer space via charge defects in the layers such as $SiO_2 \rightarrow AlO_2^- \cdots K^+$ or $AlO(OH) \rightarrow MgO(OH)^- \cdots Na^+$ defects (Fig. 43). The deficiency in one valence electron of Al versus Si, or of Mg versus Al, respectively, introduces a negative charge on the surrounding oxygen atoms at the defect sites in the lattice which maintains an isoelectronic framework [407]. The cations between the layers compensate for negative charges in the rigid bonded layers and render the mineral surface hydrophilic. These features contribute to swelling of bentonite (montmorillonite) soil by intercalation of water and humic substances [20]. Alternatively, in so-called 1:1 layered silicates, only one silicate and one aluminate sheet are covalently fused together. Examples of such clay minerals are kaolinite, $[Si_2O_4][Al_2O(OH)_4]$ [408–410], and its tubular isomorph halloysite [411,412]. Defects and sites for ion exchange are then rare, however, covalent surface modifications on superficial AlOOH groups and silicate layers are possible to develop materials for tissue scaffolds, controlled drug release, and high strength polymer nanocomposites [412,413].

5.4.1. Ion exchange, structure and dynamics of alkyl-modified clay minerals

Cation exchange reactions of 2:1 clay minerals lead to organically modified surfaces, for example:

Fig. 40. Dispersion of nanosheets of transition metal chalcogenides and BN in aqueous solution requires the use of surfactants such as sodium cholate or SDS. (a) Photograph of dispersions of MoS_2, WS_2, $MoTe_2$, $MoSe_2$, $NbSe_2$, $TaSe_2$, and BN stabilized in water by sodium cholate. The powders were sonicated at initial concentration, $Ci = 5$ mg/ml, with a surfactant of concentration $C(SC) = 1.5$ mg/mL for 30 min. (b) Chemical structure of two layers of a transition metal dichalcogenide where M is the transition element and X the chalcogen. Two polytypes of single-layers are shown: trigonal prismatic (D_{3h}) and octahedral (D_{3d}). (c) Sodium cholate. (Reproduced with permission from Refs. [392,390].)

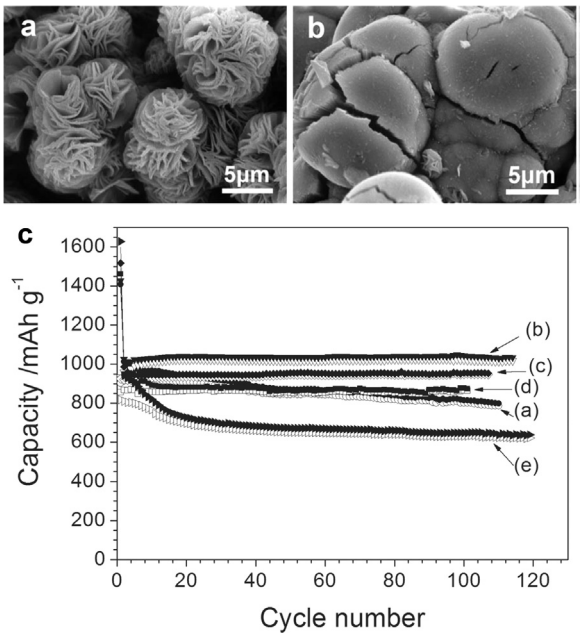

Fig. 41. MoS_2 shape control by surfactants and applications in electrode materials. (a, b) SEM images of MoS_2 samples as obtained in 3 mol/l NaOH solution at 220 °C for 10 h. (a) With EDTA · 2Na surfactant, S/Mo ratio = 2.2. (b) Without EDTA · 2Na surfactant, S/Mo ratio = 3. Ethylenediaminetetraacetic acid disodium salt (EDTA · 2Na) functions as a surfactant to inhibit the growth along the (0 0 l) direction since EDTA is a strong chelating agent. CTAB surfactants exhibit a similar effect. (c) Testing of graphene-like (GL) MoS_2/graphite composite electrodes for Li ion storage in batteries. Cycle performances of (a) annealed MoS_2-CT02, (b) GL-MoS_2/G-CT01, (c) GL-MoS_2/G-CT02, (d) GL-MoS_2/G-CT03, and (e) GL-MoS_2 /G-CT05 at a current density of 100 mA/g are shown. The thickness of the individual units in the MoS_2/G composites are few atomic layers, increasing from CT01 to CT05 samples that correspond to CTAB concentrations of 0.01 to 0.05 mM, respectively. The storage capacity is highest for the graphene-like composite electrode at low CTAB concentration. (Reproduced with permission from Refs. [393,370].)

$$\text{mont}{-}\text{Na}_{0.4} + 0.4(n\text{-}\text{C}_{18}\text{H}_{37})\text{N}(\text{CH}_3)_3^{+} + 0.4\text{Br}^{-} \rightleftarrows \text{mont}{-}\left[(\text{CH}_3)_3\text{N}(n\text{-}\text{C}_{18}\text{H}_{37})\right]_{0.4} + 0.4\text{Na}^{+} + 0.4\text{Br}^{-} \quad (3)$$

The organic modification changes the polarity of the clay mineral surface from hydrophilic to hydrophobic and leads to a variety of organically modified clay minerals depending on the cation exchange capacity of the mineral, the length, and architecture of the surfactants (Figs. 2–4 and 44) [1,18,19,21,22,24,28,29,38,96,414,415].

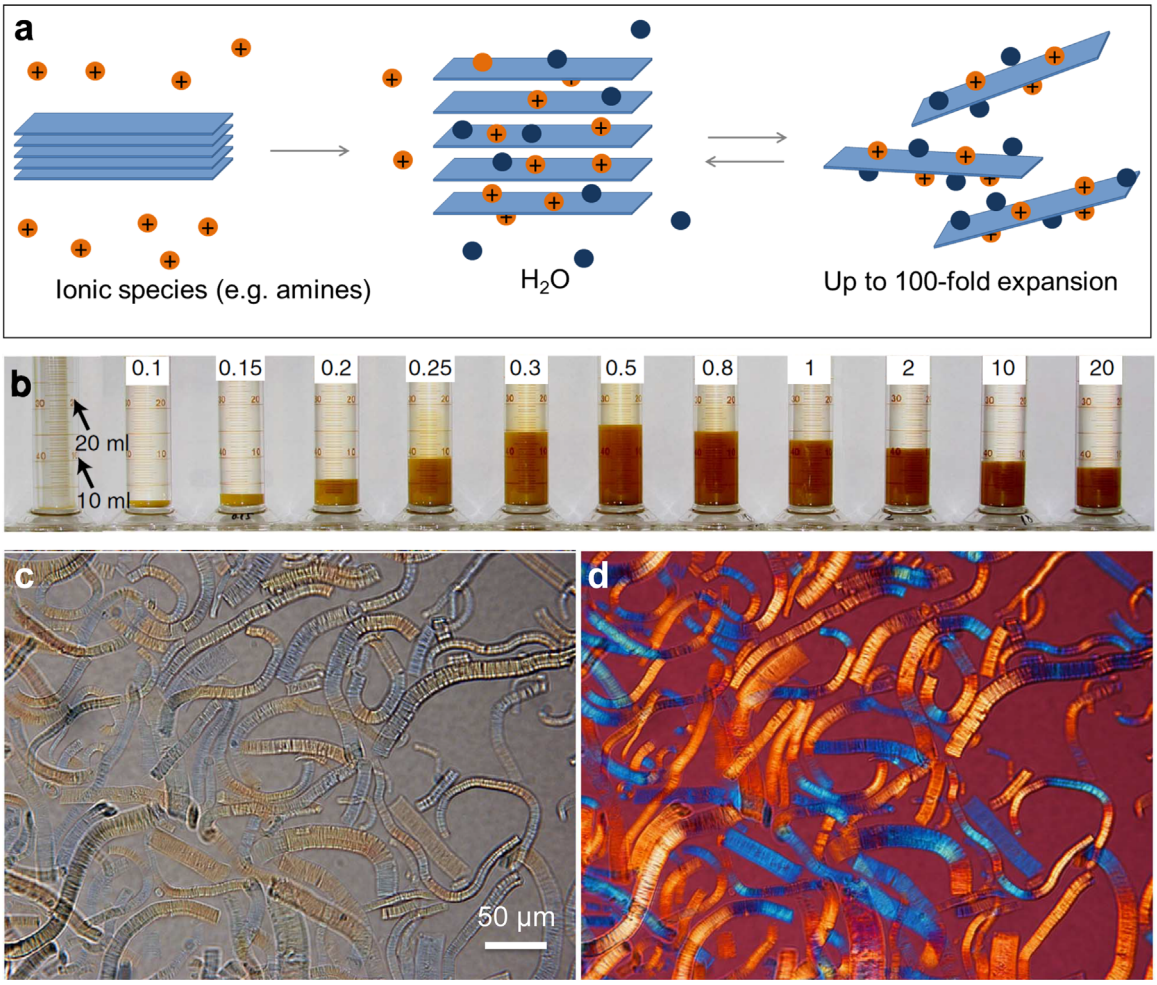

Fig. 42. Reversible swelling of layered titanates in the presence of amine intercalants. Individual layers are ~0.7 nm thick. (a) Schematic of amine intercalation, protonation, and reversible expansion of galleries of $H_{0.8}[Ti_{1.2}Fe_{0.8}]O_4 \cdot H_2O$ microcrystals. (b-d) Macroscopic volume and microscopy characterization of $K_{0.8}[Ti_{1.2}Fe_{0.8}]O_4 \cdot H_2O$ microcrystal samples upon reversible swelling. (b) Photograph showing the changes in macroscopic volume of the swollen crystals in 100 ml dimethylaminoethanol (DMAE) solutions. The given numbers from 0.1 to 20 refer to the concentration of DMAE in units of the total ion exchange capacity of $K_{0.8}[Ti_{1.2}Fe_{0.8}]O_4$. The yellow-brown swollen phases settle at the bottom of the graduated cylinders. The leftmost sample is the original $H_{0.8}[Ti_{1.2}Fe_{0.8}]O_4 \cdot H_2O$ microcrystal sample before swelling for comparison. (c) Optical microscopy image showing the extended lamellar structures of the typical swollen phases at DMAE/H^+ = 0.5. Observations were made by placing one or two drops of the swollen samples, shown in panel b, onto glass slides. The longest swollen length is ~200–250 µm (from ~2-3 µm stacks before swelling). (d) The swollen samples observed via crossed polarizers. (b-d adapted with permission from Ref. [398].) (For interpretation of the references to color in this figure legend, the reader is referred to the web version of this article.)

At low packing density (λ_0 less than ~0.20, see also Section 2.2), short alkyl chains form a monolayer parallel to the layered silicate surface (Fig. 44a and b) [94,97,416]. When the chain length increases, the packing within the monolayer increases, accompanied by a small increase in gallery height (C_2 to C_{10} in Fig. 44a). A significant increase in gallery height occurs when the lateral alkyl monolayer is densely packed so that the alkyl chains begin to build a partial second layer (C_{14} in Fig. 44a). Once a partial bilayer is formed, the gallery spacing increases only marginally up to a chain length at which the formation of a dense bilayer is completed. For longer chains, the surfactants do not fit into the bilayer and a partial third layer begins to form, which is accompanied by a marked increase in gallery spacing again (at higher CEC as shown in Fig. 44b). In this series, the interlayer density and the average chain conformation undergo similar fluctuations as a function of chain length as the basal plane spacing [97]. The interlayer density reaches maxima when densely packed layers are formed, and minima when frustrated new layers are formed. The percentage of gauche conformations in the alkyl layers varies between 15% and 40%, which also depends on the presence of a primary ammonium head group versus a quaternary ammonium head group, as evidenced by IR spectroscopy and molecular simulations [37,97]. Overall, the alkyl chains are in a disordered, liquid-like state, although generally with a percentage of gauche conformations clearly below that of a free-standing octadecylamine liquid at 100 °C. (~40%) [94,97].

At higher packing density (λ_0 above ~0.20), alkyl chains form tilted layers as illustrated for octadecyltrimethylammonium chains on mica (Fig. 45). The alkyl chains are imperfectly ordered at room temperature and can undergo reversible phase transitions upon heating (see also Fig. 3b) [38,96,414]. The order of the chain backbones is lost above ~40 °C, which causes one or two phase transitions (Fig. 45). The first phase transition involves an order-disorder transition of the tethered alkyl backbones and is immediately reversible upon cooling. A second transition is seen for quaternary alkylammonium ions at ~70 °C, which shows a larger melting enthalpy [96], and involves changing locations of the quaternary ammonium head groups on the surface (this transition is not observed for primary ammonium surfactants with additional hydrogen bonding to the silicate surface). The second transition is not immediately reversible upon cooling, as seen in

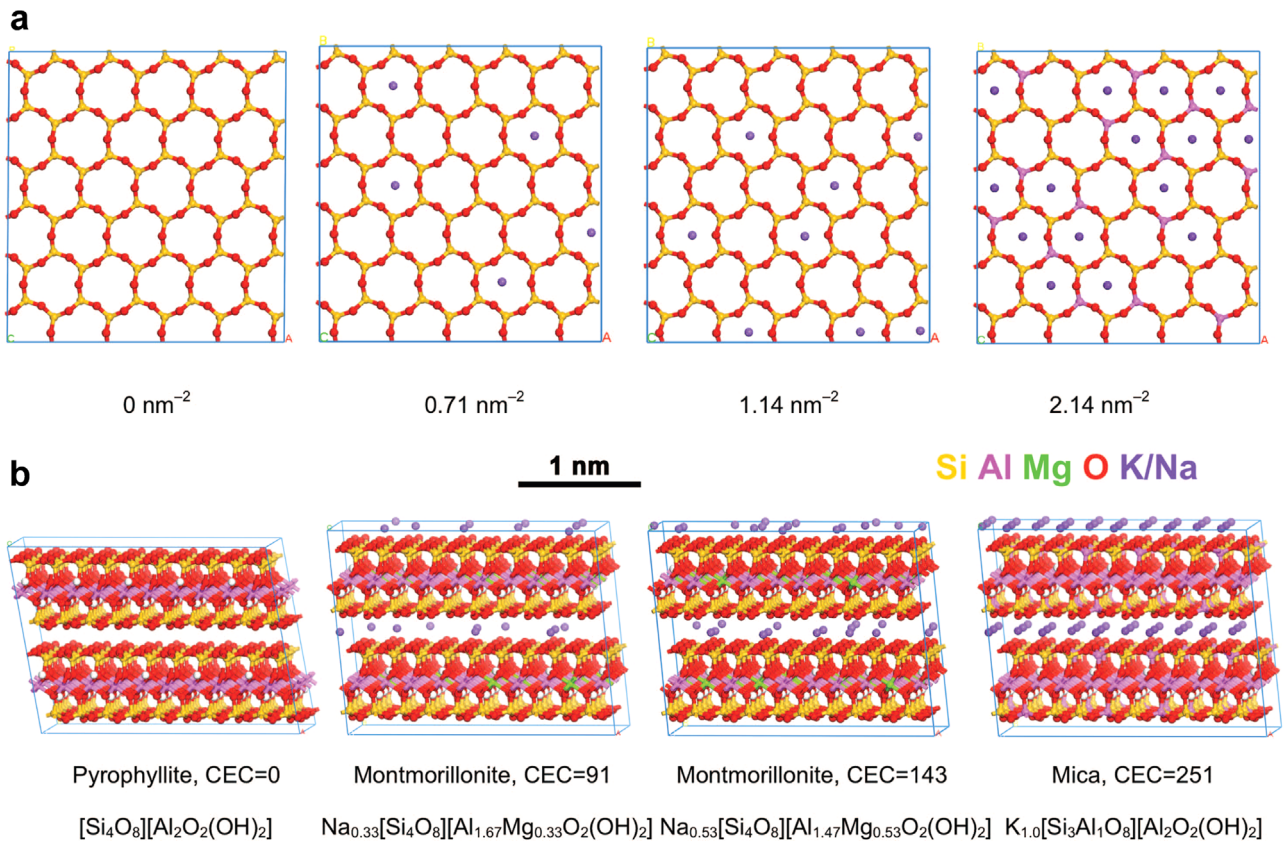

Fig. 43. Examples of the structure and chemical composition of common 2:1 clay minerals (smectites, vermiculites and micas). (a) The top view depicts the variable cation density on the cleaved mineral surfaces. (b) The side view shows the nanometer-scale structure of the layers. Pyrophyllite contains no interlayer cations, montmorillonite is of intermediate cation density, and muscovite mica has the highest density of 2.14 cations per square nanometer on a cleaved surface. The cation exchange capacity (CEC) is a measure of the amount of exchangeable cations in meq/100 g material. The value for mica is a hypothetical maximum as complete exchange of all interlayer cations requires special treatments. (Reproduced with permission from Ref. [41].)

the DSC curve, due to significant energy barriers for rearranging the quaternary ammonium head groups back to the original position (Fig. 45). Recovery of the second transition is complete after several hours [39,96]. Transition temperatures of the alkyl chains range from 0 °C to 100 °C depending on length and ordering; enthalpies up to 12 kJ/mol tethered C_{18} chain have been measured. The percentage of gauche conformations in the alkyl chains is about 20–25% in the semi-crystalline state and increases to approximately 30% in the molten state [38].

Conformational differences between different organoclays and the variations across the range of temperatures can be conveniently analyzed by NMR and IR spectroscopy (Fig. 46) [37,414]. ^{13}C-NMR reveals gradual changes in anti-conformations versus gauche-conformation as the temperature increases (Fig. 46a). The ^{13}C methylene chemical shifts indicate the conformational "freezing" at lower temperature. However, the NMR data do not allow monitoring of the transition temperature because there is no abrupt change in the percentage gauche conformations. Infrared spectroscopy can detect the changes in the symmetric and asymmetric CH_2 stretching vibration as a result of melting and rearrangements of the quaternary ammonium head groups on the surface (Fig. 46b). It is possible to discern melting temperatures from the small shifts in IR wavenumbers when plotted as a function of temperature within ± 3 K [414]. However, in case of two separate transitions (Fig. 45), IR spectroscopy detects only the transition at higher temperature associated with greater conformational and larger enthalpy [96]. Standard NMR and IR spectroscopy may thus not be able to exactly determine the number and temperature(s) of the phase transitions observed. Therefore, DSC is apparently the most reliable indicator for phase transitions. Details of the relationship between packing density, tilt angles, and thermal transitions were described in Section 2.2.

5.4.2. Cohesion between layers

The interlayer structure and density of organically modified clay minerals also affects the cohesion between the individual clay layers. A quantitative measure for the "stickiness" between the layers is the cleavage energy (Fig. 47) [417,418]. Ion exchange for alkylamonium surfactants as described above, for example, lowers the cleavage energy of (non-hydrated) montmorillonite from 133 mJ/m^2 to only 40 mJ/m^2, i.e., by 70% (CEC 91 meq/100 g), and use of different surfactants enables a tunable range from 25 to 210 mJ/m^2 (CEC 143 meq/100 g) [41,418]. The underlying cause for this widely tunable range is the tunable separation of positively charged head groups between adjacent aluminosilicate layers at equilibrium distance (see highlights in Fig. 47). In the unmodified montmorillonite, over 70% of the cleavage energy consists of Coulomb energy that results from the initial separation of interlayer cations (Fig. 47a). These forces are of short range as after more than 0.5 nm layer separation away from equilibrium distance the cations distribute equally between the two separated layers and remaining Coulomb energies are small. In the surfactant modified mineral, the organic interlayer separates the cationic head groups among the two clay minerals layers already before cleavage so that essentially only van-der-Waals interactions remain (Fig. 47b). The surface is then similar to a paraffin surface rather than an ionic clay surface, and the cleavage energy as well as the barrier to dispersion in a nonpolar polymer matrix are much lower.

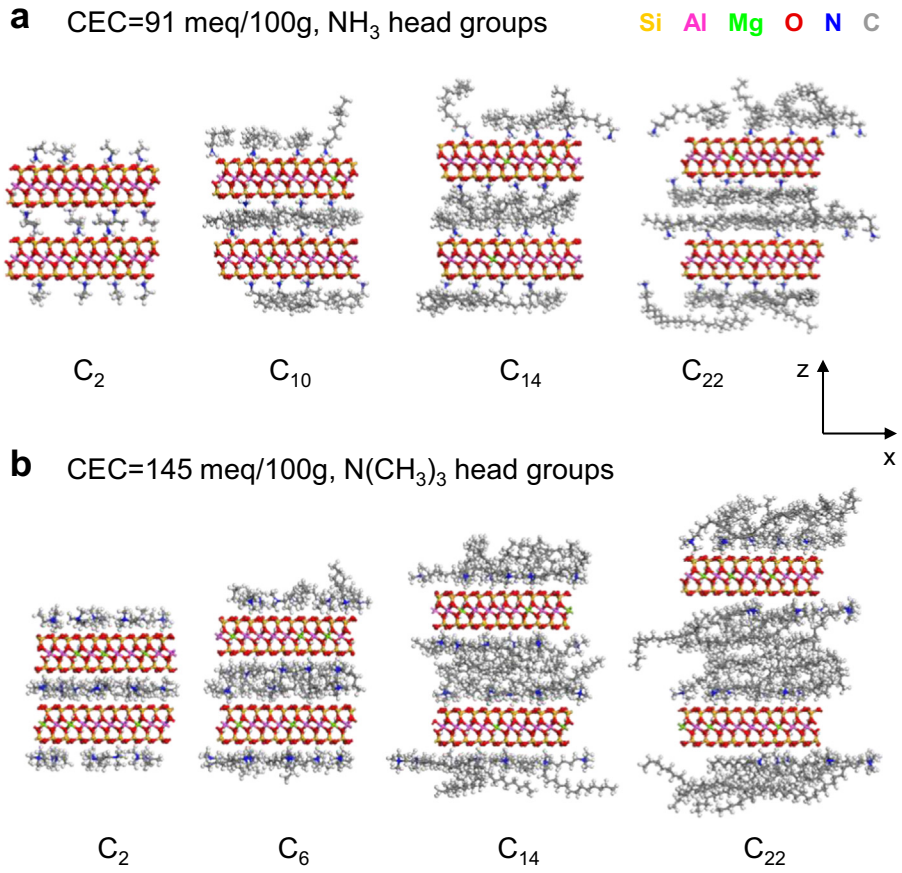

Fig. 44. Visualization of the structure of alkylammonium montmorillonites at the nanoscale in molecular dynamics simulation, viewed along the *y* direction. (a) CEC = 91 meq/100g and NH_3^+–C_nH_{2n+1} chains (packing density $\lambda_0 = 0.13$). The difference between partially formed layers (C_2, C_{14}) and completely formed layers (C_{10}, C_{22}) can be seen. (b) CEC = 145 meq/100 g and NMe_3^+–C_nH_{2n+1} chains (packing density $\lambda_0 = 0.21$). The successive formation of (pseudo)layers with decreasing order can be seen. (Reproduced with permission from Ref. [97].)

5.4.3. *Dispersion in a host matrix*

A common reason for surface modification of layered nanofillers in composites and hydrogels is the desire for homogeneous dispersion, or "exfoliation", in a polymer host as opposed to aggregation [3,358,404,418]. The propensity for mixing depends on interfacial energies that are determined by cleavage energies, solvation energies, and solubility (Fig. 48). The free energy of exfoliation, ΔG, is composed of contributions from cleavage of the mineral layers ΔG_M, from the creation of void spaces in the polymer matrix ΔG_P, and from recombination of the cleaved mineral surface with the polymer ΔG_{MP}. As seen in Fig. 47, the cleavage energy of the mineral without surface modification can be prohibitively high [418]. Therefore, lower values of ΔG_M by surfactant modification play a critical role to support dispersion. The radius of gyration of the polymer and kinetic effects of polymer motion to create void spaces for the mineral layers in the matrix are also a barrier towards achieving dispersion (ΔG_P). ΔG_P may have to be accepted as is, however, as often the polymer cannot be freely chosen due to its overall desired properties for the composite. ΔG_{MP} reflects the interfacial free energy to combine filler and polymer matrix. In case of direct reactive cross-linking with the polymer matrix, ΔG_{MP} becomes negative and can be a strong driver for ΔG towards exfoliation. Mechanical processing using extrusion and ultrasound are typically employed to overcome positive values of ΔG. When processes occur in a good solvent for clay and the polymer, the separation of layers and interaction with polymers can become exergonic, as is the case for several clay-containing hydrogels (such as spontaneous swelling of montmorillonite in water and mixing with polyethylene oxide without further modification) [3,419,420].

As an example, the addition of laponite clay (approximate formula: $Na_{0.25}[Si_2O_4][Mg_{2.75}Li_{0.15}Na_{0.1}O_2(OH)_2][Si_2O_4]$) [421] to collagen-based hydrogels resulted in enhanced surface interactions and bone growth activity [3]. A 4-fold increase in compressive modulus was reported upon incorporation of laponite along with an increase in pore size compared to collagen-based hydrogels. The laponite nanocomposite hydrogels were capable of promoting osteogenesis in vitro in the absence of any osteoinductive factors. A 3-fold increase in alkaline phosphatase activity and a 4-fold increase in the formation of a mineralized matrix were observed. Although the underlying mechanisms are not yet well understood, the clay mineral showed multiple functions conducive to the regeneration of bone in nonunion defects in a growth-factor-free microenvironment, such as increased network stiffness and porosity, injectability, and enhanced mineralized matrix formation [3].

5.5. *Layered double hydroxides and applications*

Layered double hydroxides (LDH) are often considered as "anionic clays" and can be synthesized from a number of main group and transition metal hydroxides [138,355,422–426]. A common layered double hydroxide is hydrotalcite, $Mg_6Al_2CO_3(OH)_{16} \cdot 4(H_2O)$ (Fig. 49). It consists of ~0.7 nm thick metal hydroxide layers in between which water-soluble anions are located. The layer charge results from the combination of formally two-fold charged

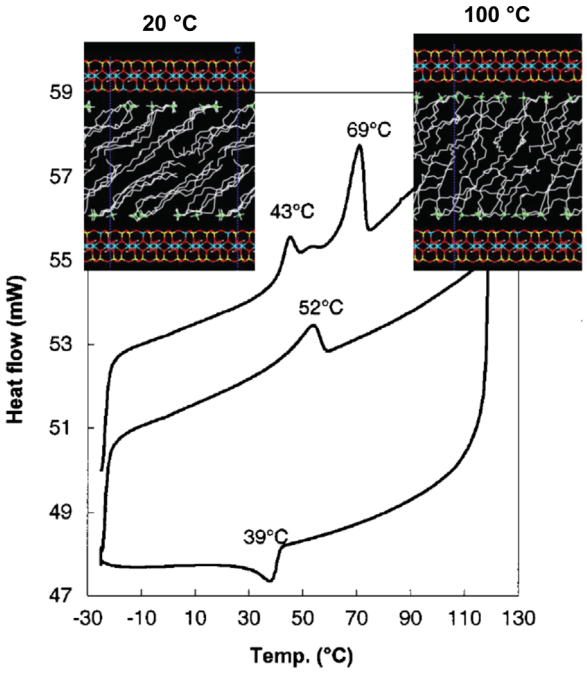

Fig. 45. Thermal transitions of alkyl chains on mica. The DSC trace of octadecyltrimethylammonium mica shows two transitions upon heating (80% ion exchange and packing density $\lambda_0 = 0.40$). The second transition at 69 °C is not immediately reversible; it involves lateral rearrangements of the head groups on the surface. The insets show models of the corresponding molecular structures at 20 °C and 100 °C as seen in molecular dynamics simulations. (Adapted with permission from Refs. [38,96].)

(Mg) and a minority of formally three-fold charged metal ions (Al) in the dihydroxide layer. The excess positive charge is compensated by the anions in the interlayer space, such as carbonate, nitrate, or sulfate. Accordingly, a more general formula for LDHs is $[M_{1-x}^{2+}\ M_x^{3+}(OH)_2]^{x+}[A_{x/n}]^{n-} \cdot m(H_2O)$ [424]. The anions in the interlayer space can be exchanged for a wide range of negatively charged surfactants, for example, carbonic acids, amino acids, SDS, anionic polymers, drug molecules, as well as for inorganic anions and reduced oxygen species [138,425,427,428].

An example for surfactant interactions with LDHs is the intercalation of vitamin C into MgAl, MgFe, and ZnAl LDHs by co-precipitation and reconstruction (Fig. 50) [429,430]. The molar ratio between the metals was $M^{2+}/M^{3+} = 3$ and binding of the L-ascorbic acid occurred via its negatively charged anionic site. The percentage of anion exchange, the molecular orientation of ascorbic acid, and the observed gallery spacing depended on the method of intercalation. In all cases, however, the interlayer space provided a stabilizing effect and shielded the vitamin C from oxidation, to reduce the impact of exposure to air, light, and heat.

LDHs can also serve as mechanical reinforcements to prepare ultrastrong nanocomposite hydrogels (Fig. 51a) [431]. MgAl LDHs were superficially modified with isethionate ($HO(CH_2)_2SO_3^-$), and a composite of polyacrylamide with low content of the modified LDH showed nearly complete exfoliation of the inorganic layers upon in-situ polymerization. The exfoliation is seen from changes in the X-ray patterns for neat LDH and hydrogels with different LDH content (L_1M, L_2M, L_3M) (Fig. 51b), as well as TEM micrographs (Fig. 51c and d). The hydrogels show dramatically altered properties compared to neat polyacrylamide, including over 30-fold improvements in the elongation at break and nearly triple the yield strength (Fig. 52).

Layered double hydroxides are also used as catalysts or catalyst supports due to the ability to immobilize various active ligands on the surface that exhibit catalytic activity not found when fully dissolved in solution (Fig. 53) [432]. For example, MgAl–LDHs containing different intercalated amino acids exhibited higher activity in the chemoselective O-methylation of phenols and S-methylation of thiophenol with dimethyl carbonate in comparison to a negligible activity of the free amino acids. The intercalation of amino acids thus created an environment facilitating the reaction in a facile manner with high conversion efficiency and selectivity (Fig. 53). The catalysts could also be easily recycled and reused without decreasing the catalytic activity. A plausible reaction pathway for the O-methylation of phenol was proposed for the leucine-intercalated LDH catalyst (Leu-LDH) as an example (Fig. 53). The amine group of leucine is exposed and the elongated side chain creates a hydrophobic pocket. The free amine could then abstract a proton from phenol generating a phenolate anion, which in turn attacked dimethylcarbonate forming a six membered transition state, which rearranges to give the anisole product [424].

Other applications of functionalized LDHs include supercapacitors [423], oxygen evolution catalysts [425,426], drug delivery systems, biological reactors and sensors [138,424].

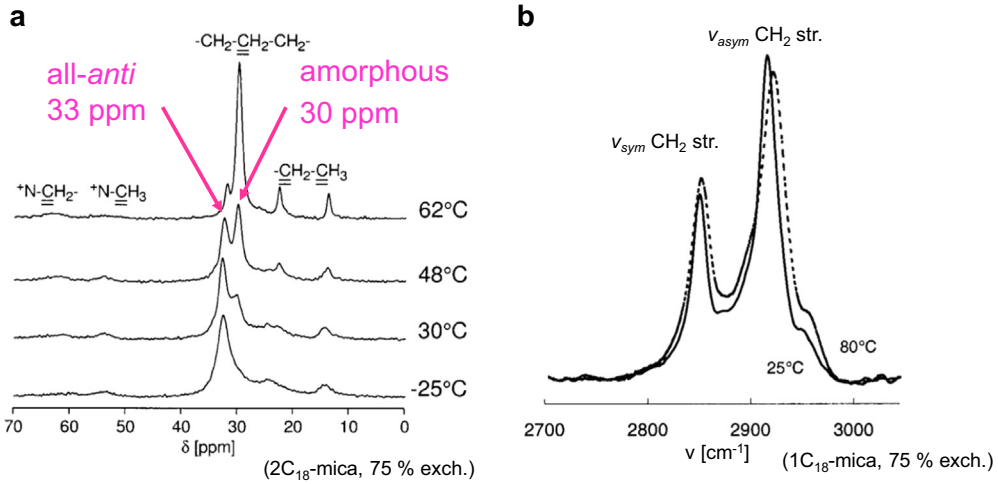

Fig. 46. Conformational information on the alkyl chains from NMR and IR spectroscopy. (a) ^{13}C-NMR on $2C_{18}$ mica at various temperatures (CEC = 251 meq/100 g with ~75% of ions exchanged). A sole ^{13}C chemical shift at 33 ppm indicates all-anti conformations, and emerging peaks at both 30 and 33 ppm indicate the emergence of gauche conformations at higher temperatures. One phase transition at 59 °C was observed for this system in DSC. (b) Small differences in IR adsorption energy (3–6 cm^{-1} shifts) can indicate the approximate T of phase transitions (± 3 K), shown for $1C_{18}$ mica shown. (Adapted with permission from Refs. [96,414].)

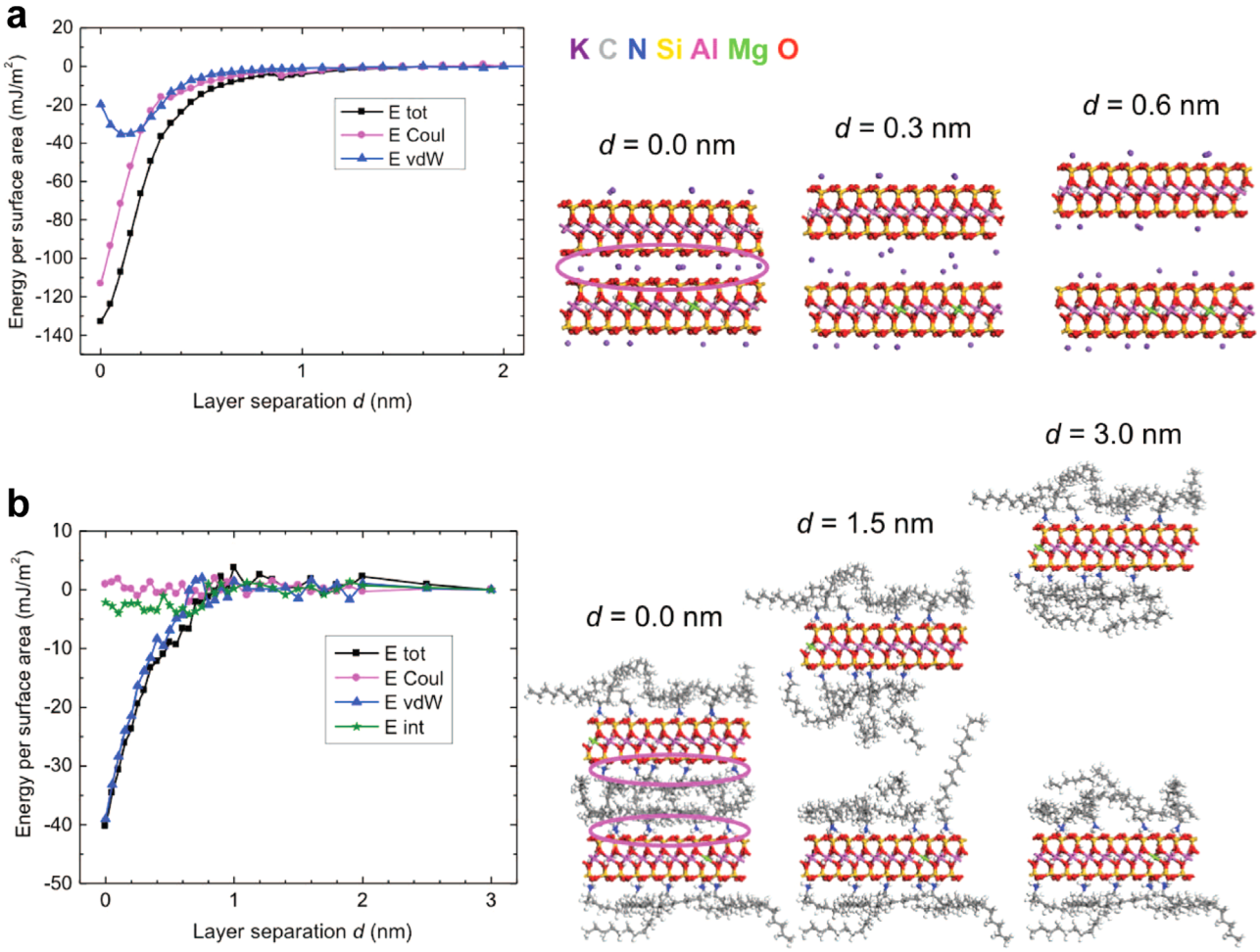

Fig. 47. Cleavage of montmorillonite and the role of surfactants. The alkyl chains in the interlayer of octadecylammonium montmorillonite shield Coulomb forces between the layers and reduce the interaction energy. (a) Cleavage energy of sodium montmorillonite. The cleavage energy of the unmodified mineral is mainly composed of Coulomb energy to separate and redistribute the alkali cations between the two layers. This process occurs at short distances below 0.5 nm layer separation in the absence of solvents. (b) Cleavage energy of octadecylammonium montmorillonite. The cleavage energy of the modified mineral is reduced by ~70% relative to the neat mineral due to the separation of the ammonium head groups pertaining to each of the two layers before cleavage (see oval highlights). The ~0.8 nm thick organic layer shields the positively charged head groups from mixing with each other. Entropic contributions to the cleavage free energy are near zero in the natural clay minerals and remain minor for organically modified clay minerals (smaller than 5 mJ/m^2 related to conformational changes of the alkyl chains). Beyond 2–3 nm separation of the layers, residual interaction energies are <3 mJ/m^2 for unmodified and modified minerals. (Adapted with permission from Ref. [417].)

6. Surface modification of cement minerals and other inorganic nanostructures

A broad range of functionally modified inorganic nanostructures from across the periodic table is being explored for exciting applications and holds tremendous potential for future use [62,342,433–435]. This review can impossibly cover all types of nanoparticles, and rather focuses on a selection of compounds of current technological importance, and where mechanistic details of surfactant interactions are available. At the time of discovery of systems with new functionality, the underlying science for interfacial interactions with ligands and the observed performance are often still unclear. In the following, interfaces in building materials will be discussed, followed by a survey of inorganic nanoparticles and surface modifications that are less covered in this review.

6.1. Nanoparticle-organic interfaces in cementitious materials

Cement has the worldwide largest annual production of man-made materials on a scale of billion tons every year and forms a special nanomaterial called calcium silicate hydrate (C-S-H) upon hydration [435–438]. Calcium silicate hydrate is the main product formed during the hydration of cement, located on the surface of cement particles, and acts as a binder in concrete (Fig. 54a–c). C-S-H reaches a high specific solid-liquid interfacial area (80–280 m^2/g) [439], and can be viewed as an assemblage of nanoparticles, or as a nanotextured material [236,440–445]. The stoichiometry is variable and the basic building blocks are known [446,447], however, there are still conflicting interpretations about its mesoscopic structure (Fig. 54c and d) [448]. Despite these divergences it is agreed that key engineering properties of concrete are affected by the high specific surface area of calcium silicate hydrate binder. The key engineering properties include strength through cohesive forces between contacting hydrates, shrinkage through capillary forces and/or disjoining pressure [442], as well as durability through transport of ions and water.

It is therefore of great interest to control the properties by modifying the calcium-silicate-binder, including its interfacial behaviour and use of organic additives. Because the surfaces involved in a commodity material such as cement are so large, opportunities for interfacial engineering are also limited by cost constraints. If cost is less a concern for specialty applications, the addition of certain fillers such as 0.15% of functionalized WS_2 nanotubes to Portland cement can lead to improvements in the strength up to 80% and to inhibited crack propagation related to the high aspect ratio and high modulus [449]. On a large scale with

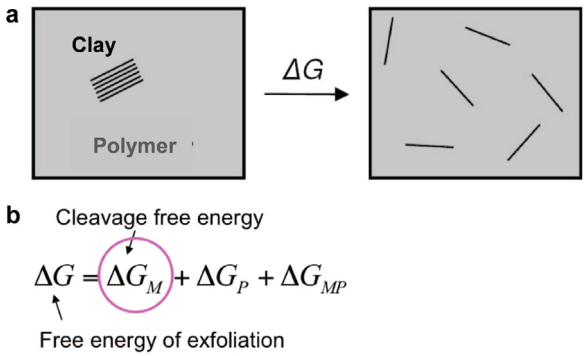

Fig. 48. Dispersion of clay minerals and surface-modified clay minerals in polymer matrices (exfoliation). (a) Schematic diagram for the homogeneous dispersion of aggregated layered silicates in a polymer matrix and the associated balance of free energy. (b) The free energy of exfoliation ΔG involves contributions by the cleavage of the mineral layers ΔG_M, creation of void spaces in the polymer ΔG_P, and recombination of the cleaved mineral surface with the polymer ΔG_{MP}. Surface modification of the clay minerals affects the cleavage energy ΔG_M, whereby lower values support dispersion in the polymer matrix. The radius of gyration of the polymer and kinetic effects of polymer motion are also critical to create void spaces for the filler in the matrix and achieve dispersion. Mechanical processing using extrusion and ultrasound are commonly employed to overcome positive values of ΔG. (Adapted with permission from Ref. [418].)

commercial impacts, promising insights from some of the more common pathways of surface functionalization are described below.

6.1.1. Polymer effects on the nanostructure of calcium silicate hydrates

One proposition is to attempt modifications of the nucleation, growth, and assembly of calcium silicate hydrate using organic additives in some form of catalytic or retardation process. Organic compounds can be used to impact the growth of the C-S-H phase, provided these compounds do not get trapped, can escape and repeatedly serve to impact the assembly process as has been reported for other inorganic compounds [451,452]. An alternative option is the modification of the growth of other phases, in particular calcium hydroxide that forms simultaneously to calcium silicate hydrate during most of cement hydration [436]. In effect, the ionic composition and stoichiometry of the calcium silicate hydrate can then be modified, as has been shown to occur in presence of polymeric dispersants (Fig. 54d) [450,453]. In the presence of a comb copolymer, an increase Ca/Si ratio was observed during the early formation of calcium silicate hydrate, although values tend to converge back together at longer times [450]. Under different conditions, a decrease of the Ca/Si ratio was reported at longer times [454]. While opposite, the results indicate that stoichiometric changes in the main product of cement hydration may be obtained thanks to surface modification by admixtures. At present, however, the changes in stoichiometry of the products are still a side effect of other, hydration-regulating and setting-regulating effects by the organic additives.

6.1.2. Modification of the formation of calcium sulfo-aluminates

The most reactive phase in cementitious materials such as Portland cement is tri-calcium aluminate, $Ca_3Al_2O_6$, which is present in amounts of 5–10% (w/w) [436]. Its origin lies in the composition of the raw materials used to produce clinker as well as by the need to have a liquid phase during the burning stage in cement kilns (~1450 °C). The reactivity of $Ca_3Al_2O_6$ is controlled by adding calcium sulfates which react with tri-calcium aluminate to produce a calcium dodecahydroxytrisulfato aluminate (ettringite), $Ca_6Al_2(SO_4)_3(OH)_{12}\cdot 26H_2O$ [436]. The formation of ettringite has great impact on early age properties, in particular rheology, but also on hardening kinetics [455]. Among a wide range of organic compounds that are used for the processing of cementitious materials, many tend to modify the nucleation of ettringite, which can substantially alter the development of cement properties [435]. Ettringite may also further evolve into Ca-Al layered double hydroxides, and polymeric dispersants may adsorb preferentially onto the layered double hydroxide surface [456,457] than being available elsewhere as dispersants [458]. The LDH platelets may assemble into an intercalated structure up to a few layers thickness under certain conditions, leading to particular conformations of comb copolymers with an adsorbing backbone and non-adsorbing, blob-like side chains (Fig. 55) [459,460].

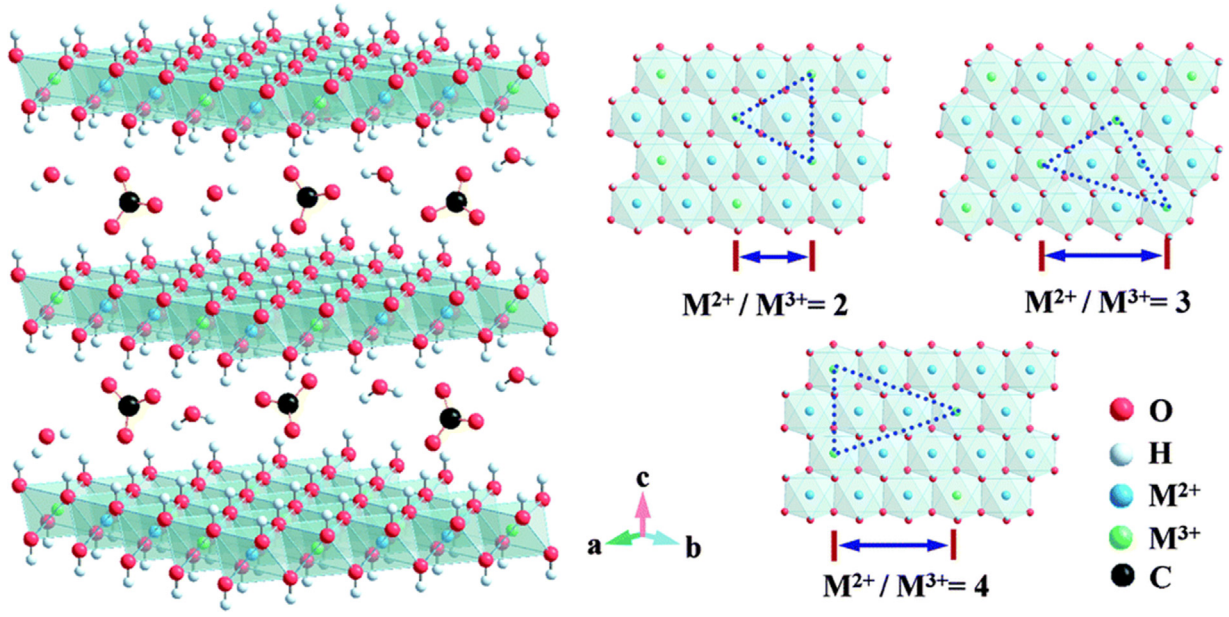

Fig. 49. Idealized structure of carbonate-intercalated LDHs with different M^{2+}/M^{3+} molar ratios showing the metal hydroxide octahedral stacked along the crystallographic c-axis, as well as water and anions present in the interlayer region. The dotted surface areas on the right hand side indicate the available surface area per anion depending on the M^{2+}/M^{3+} ratio. (Reproduced with permission from Ref. [424].)

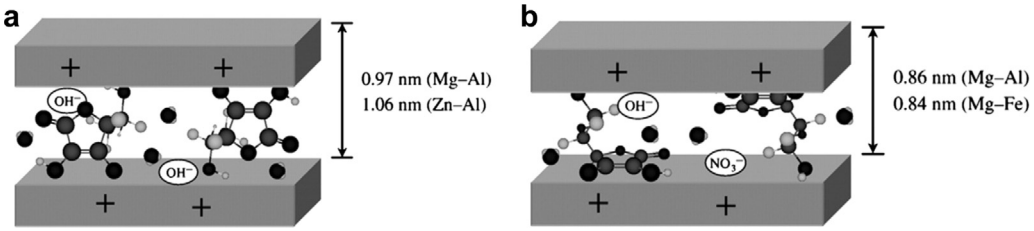

Fig. 50. Schematic illustration of L-ascorbic acid intercalation into LDHs by the reconstruction method and by the coprecipitation method. (a) With the reconstruction method, the ring assumes an upright orientation with higher gallery spacing. (b) With the coprecipitation method, the ring orients flat-on with reduced gallery spacing. (Adapted with permission from Ref. [429].)

6.1.3. Polymeric dispersants at the cement-water interface

By far the most used organic admixtures for concrete are polymer dispersants [435], of which the most effective are comb-copolymers that are produced worldwide at a rate of about 2 million tons yearly. These admixtures in just about any modern cement enhance the rheological properties of concrete, making it possible to produce materials that are stronger, more durable, and have a lower environmental footprint [84].

Polymer dispersants are highly efficient because the specific surface area of cement increases by about 2–3 times from before hydration to after hydration, allowing the polymers to thoroughly modify agglomeration and shear properties. Even before hydration, the cohesive properties of cement particles ($\sim$10 μm size) are strongly influenced by surface chemistry and agglomeration. The particular complexity of dispersing cement with respect to other materials lies in its chemical diversity and reactivity of the constituting phases. While general principles of colloidal science have quite successfully been able to account for the main structural-function dispersing behavior of these admixtures, the impact on hydration has remained elusive [450,461]. Nevertheless, substantial progress has been made recently, in particular by the possibility of predicting retardation with comb-copolymers using scaling laws [450,462].

6.1.4. Molecular modelling of interfacial properties

The aforementioned effects are governed by interface specific processes including the role of ions and organic admixtures. Many trends are explicable in terms of scaling laws and first principles, allowing to compare impacts of different compounds on competitive adsorption [463], hydration [450], and rheology [464]. However, these approaches are limited to specific classes of compounds and their generalization to more diverse chemical structures is limited. This is where molecular scale simulations of interfaces has begun to play a game changing role. For example, molecular simulations have explained how small organic compounds reduce the agglomeration energy of dry as well as hydroxylated cement particles, and affect the energy demand in industrial-scale ball mills during grinding (Fig. 56) [465–468]. One molecular monolayer of the so-called grinding aids of about 0.5 nm thickness reduces the agglomeration energy over 95% compared to the original cleavage energy of 1340 mJ/m^2 of tricalcium silicate (Ca_3SiO_5), the major phase in Portland cement. A larger thickness of the organic interfacial film produces no substantial improvement but also no deterioration in grinding performance as noticed in simulation and laboratory studies [466]. Almost 80% reduction in agglomeration energy of initially hydrated tricalcium silicate surfaces is possible due to the diminished strength of interfacial Coulomb interactions, analogous to the reduction in cleavage energies of layered silicates in polymer composites via surface modification with alkyl surfactants (Fig. 47). The reduction in Coulomb energy is due to the spacer effect of the organic interlayer and minimization of local dipole moments by molecule-specific complexation of surface ions.

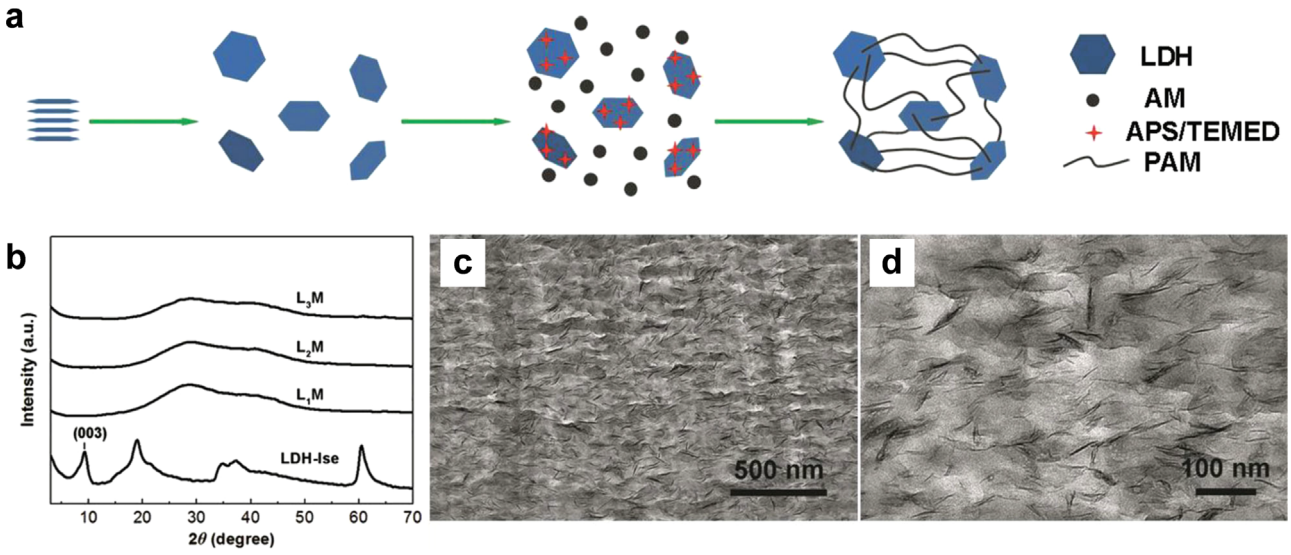

Fig. 51. Preparation and structural characterization of LDH-isethionate/polyacrylamide nanocomposite hydrogels (L_mM where *m* stands for the concentration of LDH in the hydrogel).(a) Schematic illustration showing the preparation procedure by in-situ polymerization. AM: acrylamide; APS: ammonium peroxydisulfate; TEMED: *N*, *N*, *N*′, *N*′-tetramethyl-ethylenediamine. (b) XRD patterns demonstrate that the ordered structure in LDH-isethionate ($[Mg_{2.52}Al(OH)_{7.04}](HO\text{-}(CH_2)_2\text{-}SO_3)\cdot 1.27H_2O$) was dramatically destroyed and the LDH-isethionate was greatly exfoliated in the composite hydrogels. (c, d) TEM images prove the extensive degree of exfoliation and homogeneous dispersion of LDH primary particles and nanolayers in the polyacrylamide matrix. The dark lines represent single nanolayers and primary particles of LDH-isethionate. (Reproduced with permission from Ref. [431].)

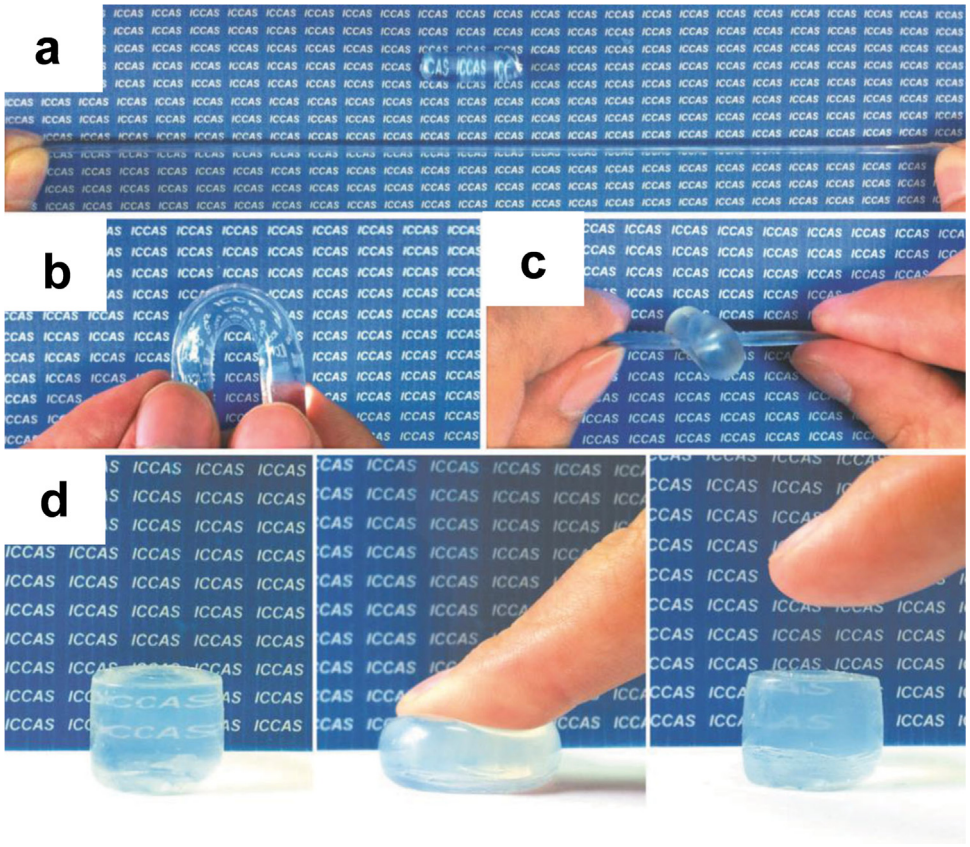

Fig. 52. Extraordinary mechanical toughness of the as-prepared LDH-isethionate/polyacrylamide hydrogels. The nanocomposites withstand high levels of deformation by (a) elongation, (b) torsion, (c) knotting, and (d) compression. (Reproduced with permission from Ref. [431].)

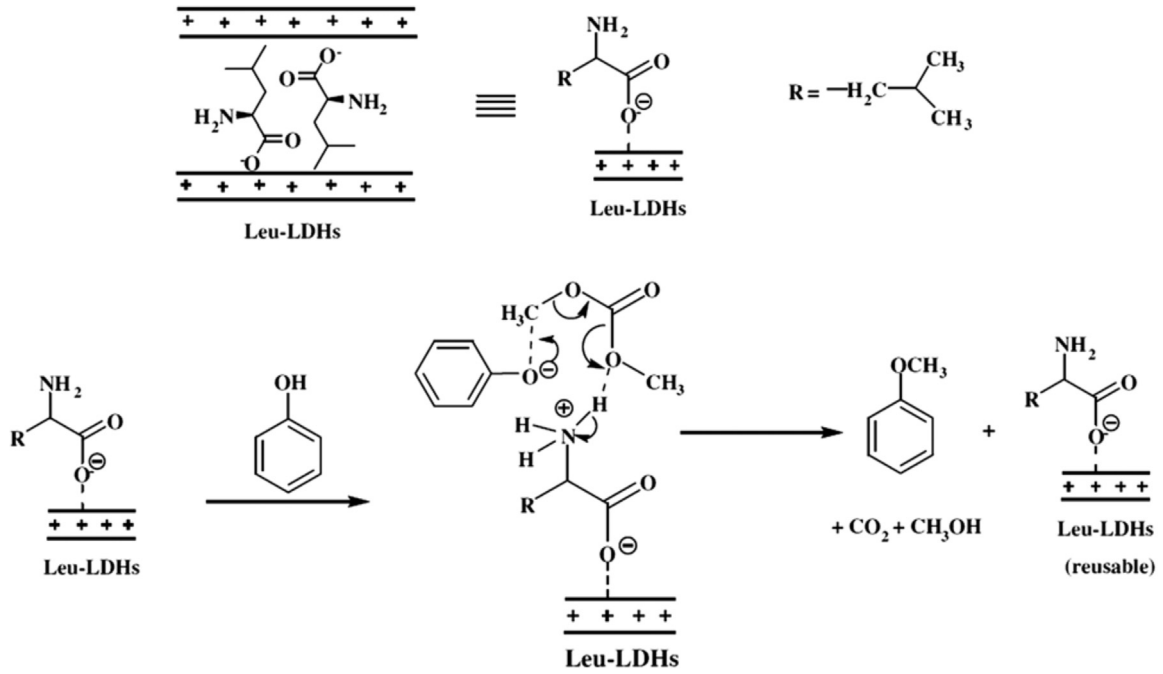

Fig. 53. Reaction mechanism for Leu–LDH catalyzed O-methylation of phenol with dimethylcarbonate. (Reproduced with permission from Ref. [432].)

6.2. Other inorganic nanostructures

Among the nanostructures not further covered are biominerals such as calcium carbonate and apatites, which are commonly found in marine organisms, bone, and teeth [62]. A key aspect of these nanocrystals and protein-nanocrystal composites is their susceptibility to pH, which allows proteins and organic modifiers to carry out biological assembly and disassembly at room temperature under physiological conditions (Fig. 57) [15]. Interactions with water, surfactants, peptides, and

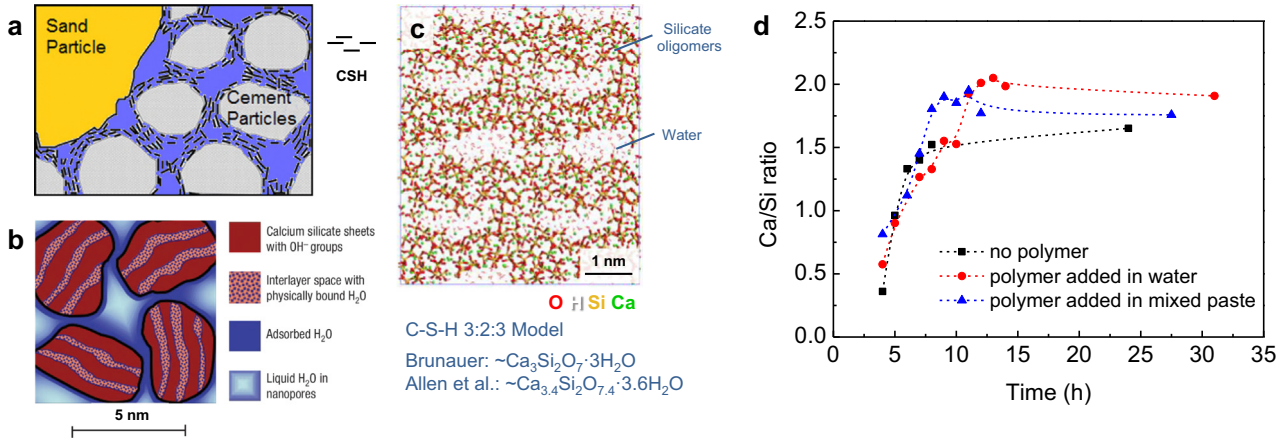

Fig. 54. The multiscale structure of cement and modification of C-S-H gel characteristics using polymers. (a) Schematic structure of concrete. Cement is the binder material and consists of particles of 1–100 mm size with a typical mean diameter of 10 mm. The particles form superficial calcium-silicate-hydrate (CSH) gel upon hydration (black rods), which consists of locally ordered layers of calcium silicate oligomers of 1–10 nm size. The agglomeration of these nanoparticles yields an amorphous material in a macroscopic point of view. (b) Schematic diagram of nanoscale C–S–H gel. The black lines indicate the interface between solid C–S–H particles and liquid water according to small-angle neutron scattering (SANS). The composition and the density of water was determined by SANS contrast variation and SAXS/SANS contrast comparison. The particle-size scale bar is based on SANS data. (c) An all-atom model of C-S-H with a typical C/S/H ratio of 3:2:3 according to the INTERFACE force field (Ref. [236]). (d) Evolution of the Ca/Si ratio in C-S-H during the first hours of hydration of pure tricalcium silicate, also known as C_3S, with and without comb-shaped copolymers as interfacial modifiers. The ratio is determined from the mass balance of the calcium between the amounts of dissolved C_3S and precipitated calcium hydroxide, which is the other product coming from the hydration of C_3S (measured and quantified by XRD and Rietveld refinement). In one case, the polymer is added in the water before mixing the C_3S with the water, in the other case the polymer is added after the mixing. The presence of organic modifiers also impacts viscosity, setting time, porosity, and ultimate strength of concrete. (Reproduced with permission from Refs. [440,450].)

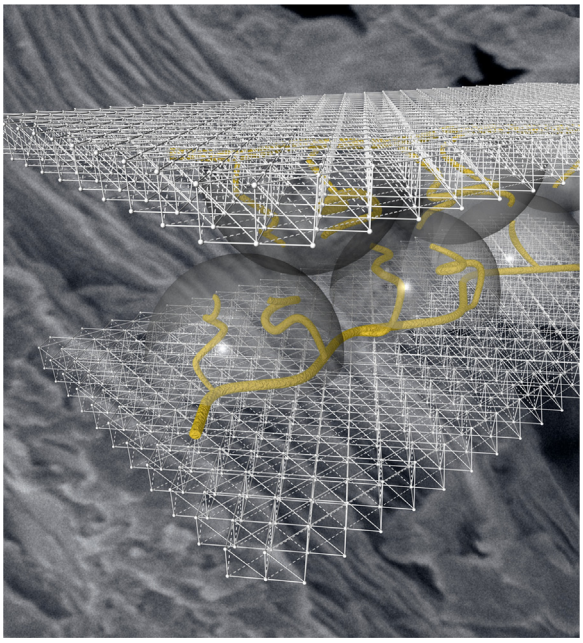

Fig. 55. Schematic representation of a layered double hydroxide (LDH) intercalated by comb copolymers. The conformation of the polymer involves adsorbed backbones carrying charged functional groups and coiled non-adsorbing side chains, which can be described by a scaling model of a 2D self-excluding chain of half spheres. (Cover image reproduced with permission from Ref. [460].)

proteins are highly pH sensitive, similar to silica and titania surfaces described in Section 4.

Calcium carbonate surfaces are mostly composed of calcium hydrogen carbonate at pH 6 to 10, and of calcium carbonate at pH values above 10 (Fig. 57a) [120,130]. Mechanisms of molecular recognition and crystal growth, though of interest for a long time, are still not well understood down to the atomic level [2,166,469–473]. The same is true for specific interactions of proteins with hydroxyapatite, mostly related to the wide range of interfacial chemistry that is related to the influence of changes in composition, pH, and hydration depth (Fig. 57b) [57,60,474–485]. The presence of interfacial regions with increased phosphate and calcium concentration spanning several nanometers complicates tracking by imaging and spectroscopy similar to hydrated cement minerals (Section 6.1). Recent developments of force fields allow insight into atomistic details on the small and large nanometer scale by molecular simulation, reproducing structures, surface chemistry, hydration energies, and binding energies of biomolecules as a function of pH [236,474]. The combination of imaging, modeling, in vitro and in vivo testing is an exciting research area for rational development of bone regeneration materials, drugs for osteoporosis, and control over biological calcification [62,474,486].

Compounds of current high promise also include perovskites as light-harvesting units in solar cells that have begun to replace dye-sensitized light-harvesting units [341,342]. In comparison to the archetypal, but photovoltaically less interesting $CaTiO_3$ perovskite, inorganic-organic perovskites such as methylammonium lead (II) iodide ($MAPbI_3$) and formamidinium lead (II) iodide ($FAPbI_3$), as well as the lead bromides $MAPbBr_3$ and $FAPbBr_3$ embedded in polyarylamine matrices have shown exceptional power conversion efficiencies [342]. Interactions with the polymer matrix and impacts on charge carrier mobility and transport mechanisms, however, are still not well understood to-date.

Monodisperse graphite particles of less than 10 nm diameter, termed carbon dots, have shown excellent catalytic properties in water splitting when dispersed in polymeric carbon nitride (C_3N_4) [434]. In this system, high photocatalytic activity of carbon nitride (C_3N_4) to oxidize water to H_2 and H_2O_2 is combined with the high activity of carbon dots for oxygen evolution from intermediately formed H_2O_2. Molecular-level details of carbon nitride, likely a polymeric form of aminoheptazine, and its relation to reaction mechanisms at the interface with the carbon dots also remain unclear to-date.

Numerous main group compounds, transition metal compounds, lanthanide compounds, and radioactive actinide compounds have been synthesized and exploited for various applications. Examples include Bi_2Te_3 in thermoelectrics [489], CeO_2 in catalysts [490], Na(Yb, Er, Ho)F_4 nanoparticles for near-infrared imaging [491], NdFeB alloys for miniature permanent magnets [492], ITO for transparent electrodes [303], and Ta/Ta_2O_5 in capacitors of mobile phones [493], Mechanistic insight into surfactant assembly and functions for these

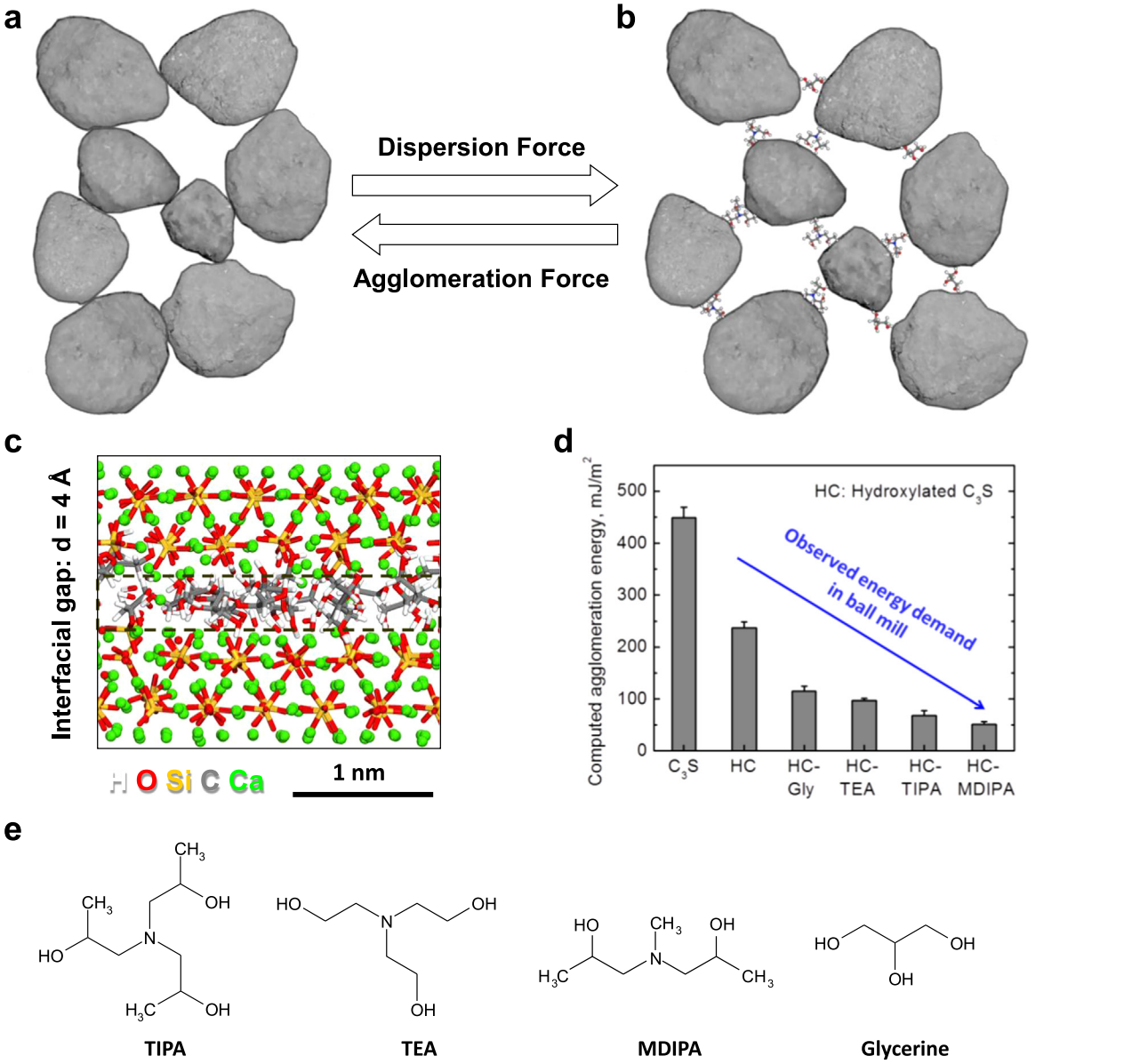

Fig. 56. Modification of particle agglomeration forces by organic additives (grinding aids) during comminution of cement clinker particles in industrial cement mills. (a, b) Conceptual representation of agglomeration of neat clinker particles and of the effect of grinding aids to aid in the dispersion of clinker particles. (c) Two tricalcium silicate (C_3S) surfaces with an intermediate monolayer of glycerine molecules. The presence of organic molecules creates an interfacial gap between tricalcium silicate surfaces that lowers agglomeration energies up to 90% in comparison to the neat mineral surfaces. (d) Computed agglomeration energy of C_3S, initially hydrated C_3S, and organically modified hydrated C_3S surfaces (0.20 mg/m^2 organic coverage). Flat surfaces were assumed in two states, separated, and together, to obtain the agglomeration energies shown. The trend correlates with the observed energy demand in ball mills. (e) Structure of common chemical additives to reduce the energy required for grinding of cement, including triisopropanolamine (TIPA), triethanolamine (TEA), N-methyl-diisopropanolamine (MDIPA), and glycerine. (Adapted with permission from Refs. [466,468].)

and infinite opportunities for other compounds may contribute to exciting discoveries in the future.

7. Modification of polymer nanoparticles with surfactants

Polymeric nanoparticles are used in many varieties to deliver drugs [52,53,494,495], in sensors [5,496], in labels for imaging [497,498], paints, and coatings [55,499,500]. Major techniques to accomplish these functions comprise covalent modification and noncovalent assembly with cargo, traceable entities, and recognition elements [142,496,497,501]. Such additions include drugs, fluorescent molecules, optically detectable and radioactive ions, enzymes, and targeting ligands, which are discussed for drug delivery and coatings in the following.

7.1. Surface modification of polymer nanoparticles for drug delivery

Polymer nanoparticles for drug delivery have been grouped into nanocapsules that contain a free-floating core of drug molecules within an outer polymer membrane (Fig. 58a), and into nanospheres consisting of a polymer matrix and embedded drug molecules without a specific surrounding shell (Fig. 58b and c) [502]. The therapeutic potential of polymeric nanoparticles generally depends on their size, shape, and surface chemistry (Fig. 59).

7.1.1. Types of polymers, particle size, shape, and cell targeting properties

The design of functional polymeric nanoparticles for drug delivery aims to improve the safety and efficacy of targeting and of

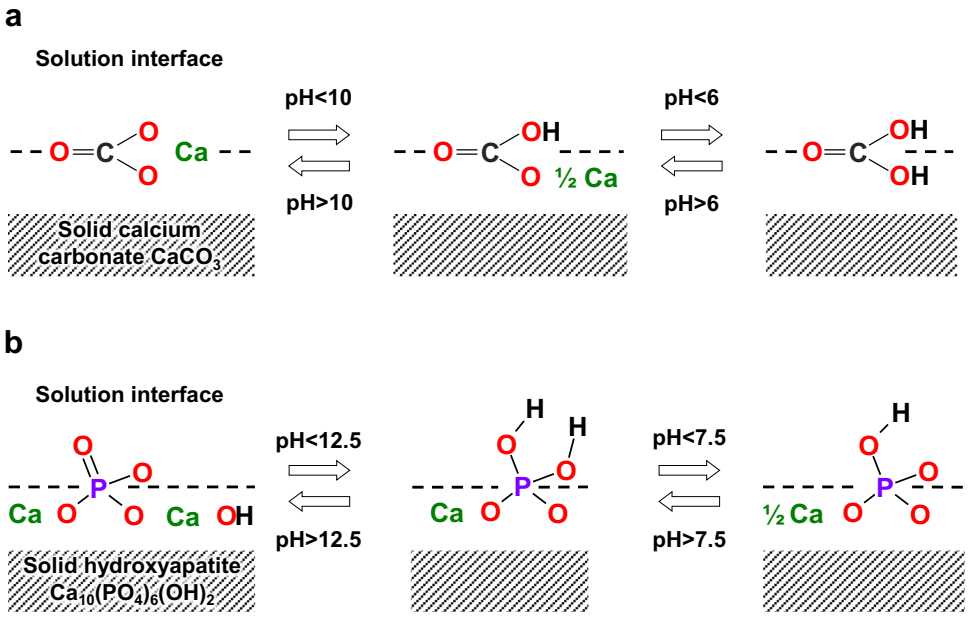

Fig. 57. Examples of pH sensitive carbonate and apatite surfaces according to experimental data from pK measurements and surface titration. Experiments and simulation have shown that the protonation state plays a major role in adsorption, often leading to the attraction of chemically different species when the pH value changes by one or more units. (a) Calcium carbonate, as found in shells of marine organisms. (b) Hydroxyapatite as found in bone, teeth, and calcified deposits in tissues (data from Refs. [183,474,487,488].)

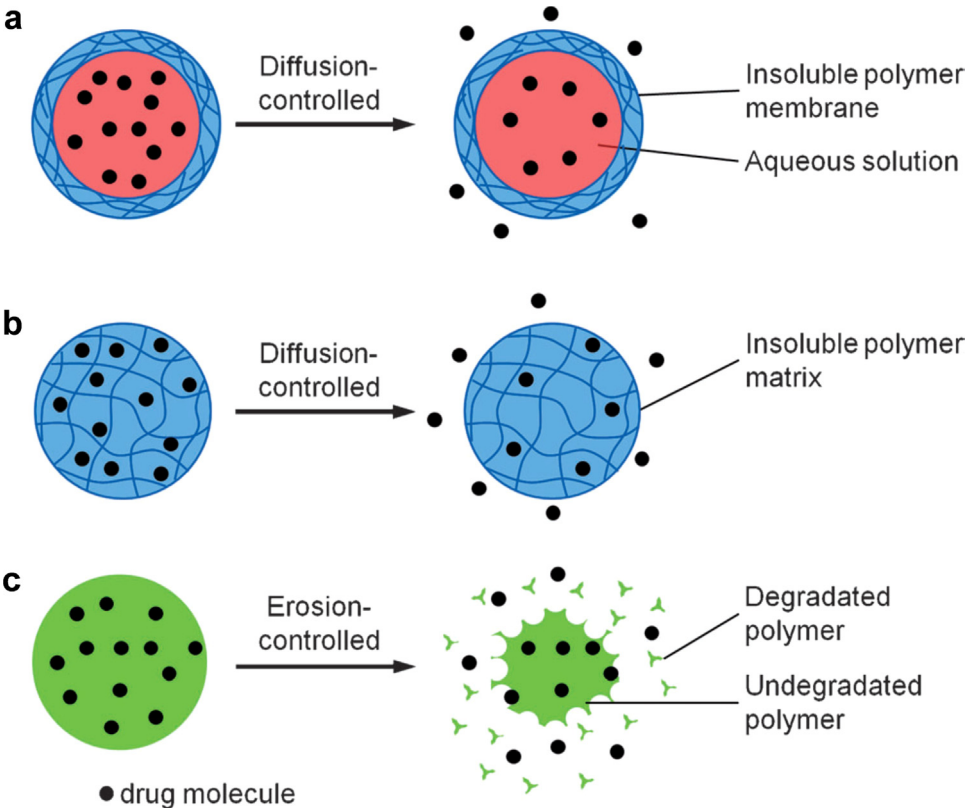

Fig. 58. Illustration of types of polymeric nanoparticles and three major mechanisms for achieving sustained drug release. (a) Diffusion through an insoluble polymer shell. (b) Diffusion through an insoluble polymer matrix. (c) Erosion of a polymer matrix. (Reproduced with permission from Ref. [52].)

the controlled release of diagnostics and therapeutic drugs. Depending on the polymer-drug compatibility, nanoparticles may have the ability to carry hydrophobic drugs to target sites at concentrations greater than their intrinsic water solubility [503]. Commonly used polymers include poly(ε-caprolactone), (PCL), poly(lactic acid), PLA, and poly(lactic-co-glycolic acid) copolymers, PLGA [504], which are proven to be biocompatible, biodegradable in controlled ways, and to possess good mechanical properties [505].

Control over size and shape of polymeric nanoparticles can help improve their performance in specific applications (Fig. 59). Surface charge, functional groups, hydrophilicity (PEGylation),

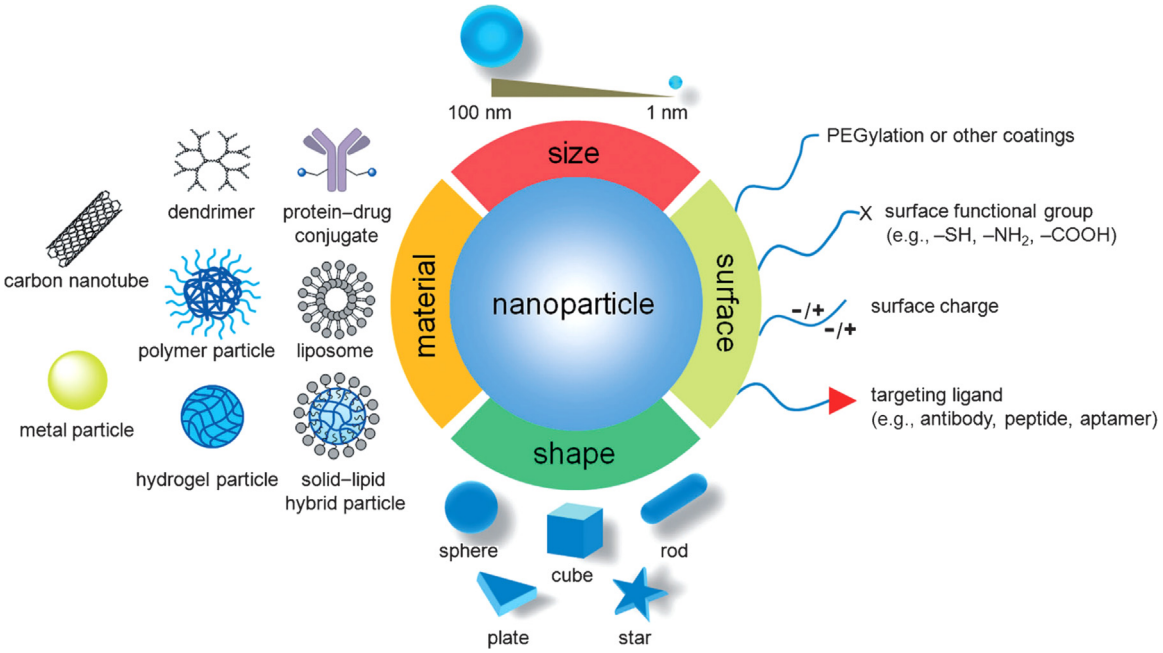

Fig. 59. A summary of nanoparticles that have been explored as carriers for drug delivery in cancer therapy, together with illustrations of biophysicochemical properties. Many systems consist of polymer and surfactant-based carriers with surface and interior modification, including dendrimers, polymer and hydrogel particles, liposomes, and hybrid particles. Size, shape, and surface properties play a major role for the release characteristics. (Reproduced with permission from Ref. [52].)

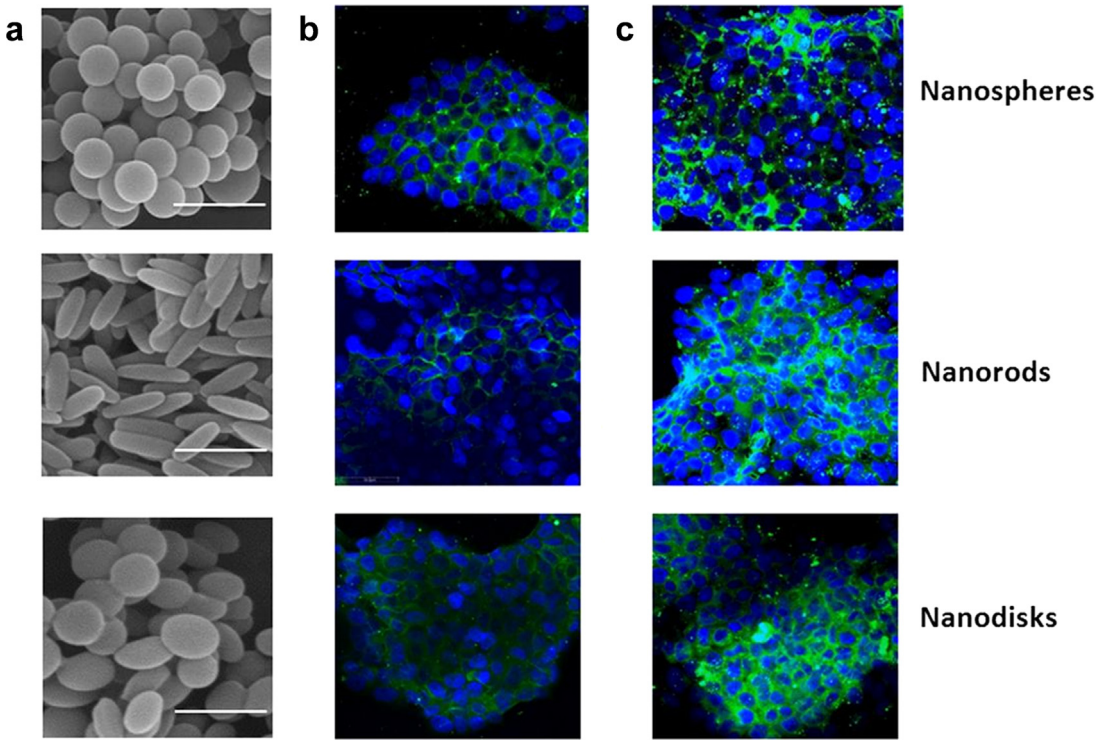

Fig. 60. Polymer nanoparticle shape and surface properties are critical parameters for drug release. Scanning electron micrograph of polystyrene particles and images of their uptake in breast cancer cells. (a) Nanospheres, rods, and discs (Scale bar: 500 nm). (b) Confocal micrographs of nanoparticle uptake in breast cancer cells without trastuzumab protein coating. (c) Increased nanoparticle uptake with trastuzumab protein coating. Microparticles of different size (above 1 μm) of the same shapes were also tested and found to exhibit different uptake characteristics. (Adapted with permission from Ref. [139].)

attachment of polysaccharides, and conjugation with targeting ligands are also essential parameters. Foremost, the ability to control the particle size is crucial as the effect of mean particle size on biodistribution varies non-linearly from organ to organ [506–508]. Once the particle reaches to a target cell, depending on the location for drug release, it can either be internalized or resist to internalization. Particle geometry (size and shape) plays an essential role for the internalization rate and the internalization mechanism. For example, nanoparticles >200 nm filtered by spleen beds cannot easily pass through interendothelial cell-slits to join the venous circulation [509]. On the other hand, quantum dots with a hydrodynamic diameters <5.5 nm were rapidly cleared from the body by renal filtration through the glomerular capillary wall and urinary excretion [510]. Particles in the 40 to 50 nm range exhibit

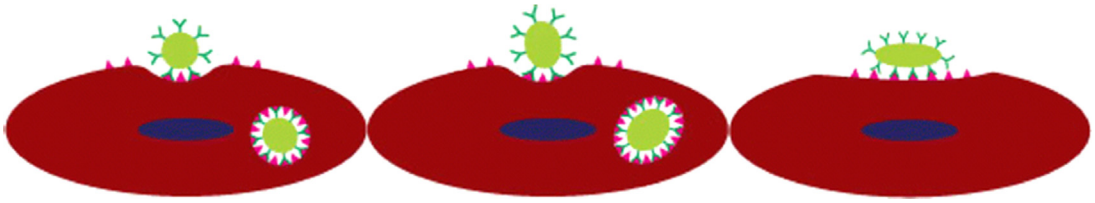

Fig. 61. Controlling cell uptake by using particles with different shape: spherical and ovoidal particles are more easily internalized compared to elongated particles that orient parallel to the cell membrane and are less easily internalized. (Reproduced with permission from Ref. [508].)

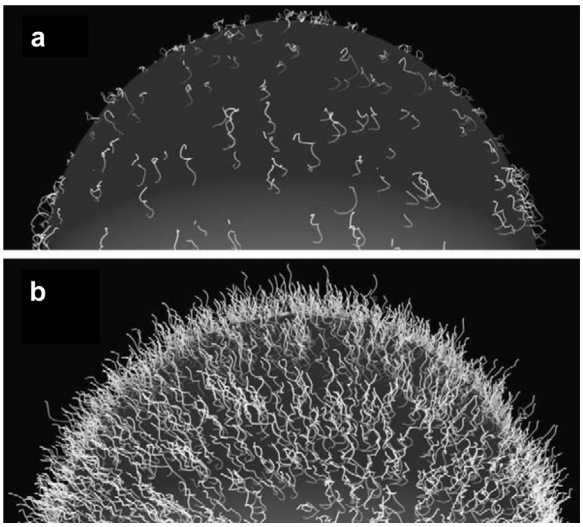

Fig. 62. Schematic of PEG grafting density and configuration on the upper hemisphere of a hydrophobic and a hydrophilic polymeric nanoparticle. (a) Low surface coverage of PEG chains (hydrophobic) leads to a "mushroom" configuration where most of the chains are located closer to the particle surface. (b) High surface coverage and lack of mobility of the PEG chains (hydrophilic) leads to a "brush" configuration where most of the chains are extended away from the surface. (Reproduced with permission from Ref. [516].)

the highest cell membrane receptor internalization. This critical cut-off range was attributed to the balance between multivalent crosslinking of membrane receptors and membrane wrapping, which are both involved in receptor-mediated endocytosis [511]. On the other hand, a recent study with surface-modified polystyrene nanoparticles by d-α-tocopheryl polyethylene glycol (1000) succinate demonstrated that 100 and 200 nm sized particles had higher cellular uptake efficiency across the gastrointestinal barrier and the blood-brain barrier than 20–100 nm sized particles [67]. These somewhat conflicting studies show that a case-by-case basis may still be preferable to gain fundamental understanding rather than the assumption of a general rule.

In addition to conventional spherical polymeric nanoparticles, recent studies have focused on the creation and exploration of the functions of non-spherical polymeric particles with at least one geometrical feature in the sub-micrometer range [512–514]. For example, the particle replication in non-wetting templates (PRINT) method allows to produce uniform polymeric nanoparticles of specific shape, size, and surface chemistry [512,514]. Tests have shown that polyethylene-glycol-based hydrogels of high-aspect ratio (sized 100 nm to 5 μm) were internalized by He-La cells ≈ 4 times faster than the more symmetric particles of aspect ratios near one.

The cellular uptake of uncoated and protein-coated polystyrene particles of different shape was tested in breast cancer cells (Fig. 60a) [139]. Similar to the results with PRINT particles above, trastuzumab (protein) coated polystyrene nanorods and nanodiscs showed higher uptake in comparison to coated nanospheres, which was attributed to the morphology-enhanced avidity and specificity of protein-coated PS particles towards protein-cell attachment (Fig. 60b and c). However, interestingly, in the absence of surface modification with trastuzumab, nanospheres exhibited higher cellular uptake than the nanorods and nanodiscs.

The change in cellular uptake depending on shape and coating is consistent with a mathematical model on receptor-mediated endocytosis (RME) of sub-micrometer particles in the presence of hydrophobic nonspecific binding interactions (Fig. 61) [508,515].

7.1.2. Tuning surface properties by surfactants

Another key property for cell targeting is the surface hydrophobicity, which can trigger opsonization, *i.e.*, the removal of polymer nanoparticle carriers from the body by the mononuclear phagocytic system [516]. Surface modification with polyethylene glycol, for example, can increase the hydrophilicity of the nanoparticle outer shell and diminish opsonization (Fig. 62). Binding of opsonins (plasma proteins and other blood components) onto the surface of polymeric nanoparticles otherwise leads to rapid uptake and clearance *in vivo*, and thus decreases the circulation time of the polymer nanoparticles in the blood stream. The adsorption of blood components onto the surface of polymer nanoparticles, therefore, affects the *in vivo* performance. It is determined by the surface characteristics and tunable by surface decoration [517–519].

Surface modification of long circulating, in other words "stealth", polymeric nanoparticles can be obtained either by coating the surface with hydrophilic polymers/surfactants or by the development of biodegradable copolymers with hydrophilic segments. As stated by Allen [516,519], if a drug carrier wants to be invisible to phagocytic cells, it needs to look like water. For long circulation times, polyethylene glycol (PEG) polymers have been extensively employed for the modification of polymer nanoparticle surfaces to make them "invisible" to phagocytic cells [520–522]. Density and configuration of PEG on the surface of polymeric nanoparticles also plays an important role in effective *in vivo* circulation and shielding of the immune system. Resistance to nonspecific protein adsorption (nonfouling characteristics) is dependent on the thickness of the surface coating that usually correlates to other factors such as PEG molecular weight, surface chain density and conformation (Fig. 62) [516]. As indicated by most researchers, chain molecular weights of 2000 g/mol or greater are required to attain sufficient chain flexibility [521].

The effect of surface chain density and interrelated chain confirmation is also seen in Fig. 62 [516]. "Mushroom" conformations are assumed at low surface coverage when PEG chains can freely move (Fig. 62a). At high surface coverage, PEG chains are in a rather extended, so-called "brush" configuration due to restricted mobility (Fig. 62b) [516]. Accordingly, for efficient shielding, PEG chains should reach far enough to achieve flexibility and remain close enough to avoid gaps on the particle surface so that the particle can be sterically protected by this conformational cloud even at low surface PEG density.

7.1.3. Release mechanism of drugs

Drug release, once polymeric nanoparticle have arrived at the destination, is governed by several possible mechanisms (Fig. 58)

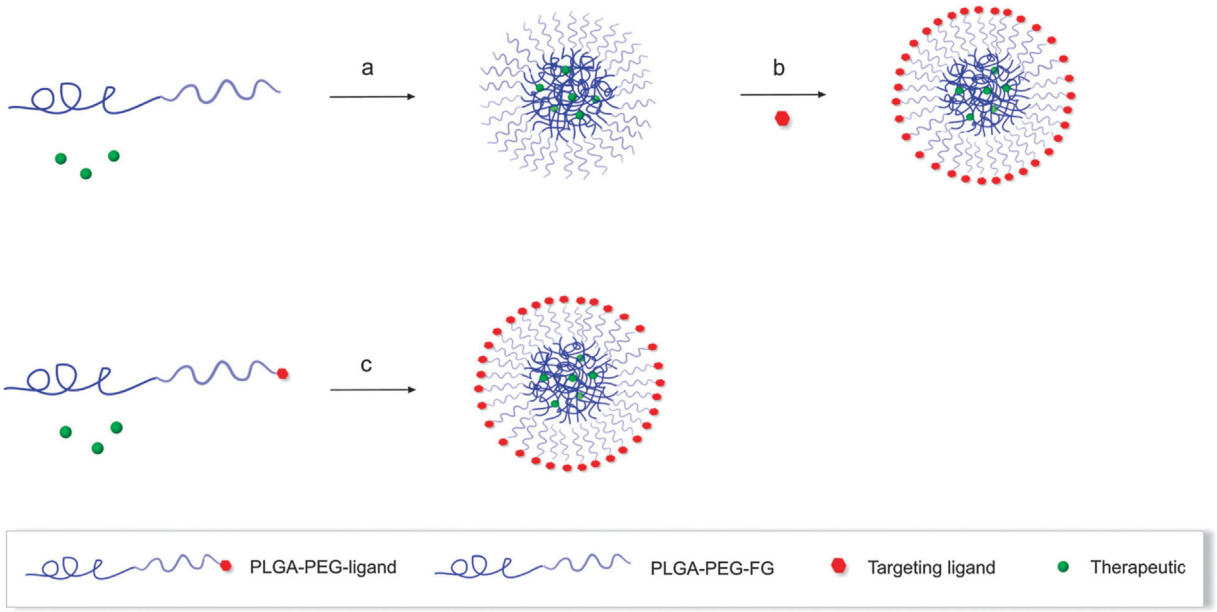

Fig. 63. Self-assembly of block-copolymers into decorated polymeric nanoparticles in aqueous solution for the example of triblock PLGA-b-PEG copolymers. (a) Polymeric NP formation via nanoprecipitation, FG = functional group. (b) Conjugation of targeting ligand to the surface of pre-formed polymeric NPs. (c) Pre-functionalized diblock polymer with hydrophilic targeting ligand. (Reproduced with permission from Ref. [520].)

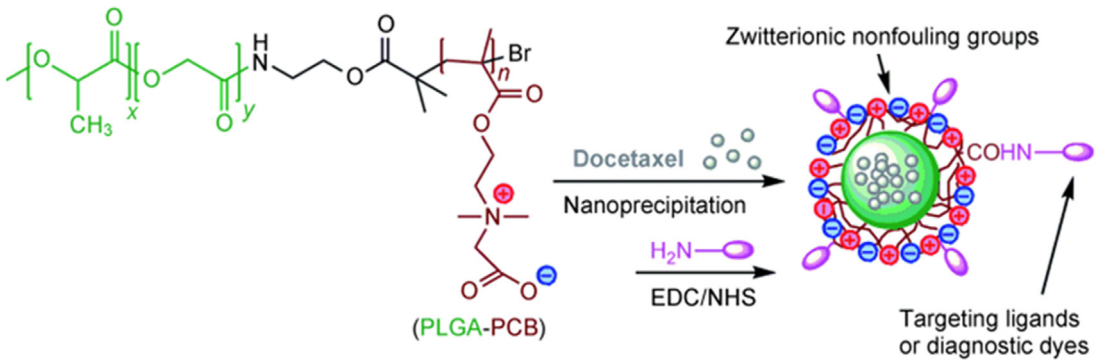

Fig. 64. Self-assembly of block copolymers with docetaxel payload and ionic surfactant end groups, which coat the PLGA core by ion pairing and attachment of targeting ligands. The PLGA core/PCB shell nanoparticles are prepared by nanoprecipitation (EDC: 1-ethyl-3-(3-dimethylaminopropyl)carbodiimide, NHS: N-hydroxysuccinimide). The design increases resistance to protein adsorption and allows specific targeting. (Adapted with permission from Ref. [527].)

[52]. These include diffusion of the drugs from nanocapsules through an insoluble polymer membrane, in which case the release is diffusion controlled (Fig. 58a). The drugs may alternatively diffuse through a polymer matrix in nanospheres (Fig. 58b). In both cases, diffusion can be controlled through polymer chemistry, chain length, and co-constituents in the membrane or matrix. Degradation of the polymer can also be chosen as a rate-determining process for drug release (Fig. 58c).

7.1.4. Synthesis and assembly for specific surface properties

The chosen method of synthesis and assembly usually depends on the physicochemical properties of the encapsulated material along with the requirements for the polymer system, particle size and target specific affinity [67,520]. Polymer nanoparticles can be prepared from preformed polymers by utilizing methods like nanoprecipitation, solvent evaporation, salting-out, dialysis and supercritical fluid technology or they can be directly synthesized by the polymerization of monomers by using techniques such as emulsion, mini-emulsion, micro-emulsion, controlled/living and interfacial polymerization [517,523].

Surface modification of the polymeric nanoparticles can be achieved through self-assembly of block copolymers that contain a segment forming the core of the polymer nanoparticle and a segment that forms the outer surfactant shell upon assembly (Fig. 63) [520]. For example, the inner segment can be PLGA and the outer segment PEG (Fig. 63a). A common technique is nanoprecipitation that involves the use of an organic solvent that is miscible with an aqueous phase. The polymer and the drug are dissolved in the organic solvent and this solution is then added dropwise to an aqueous (non-solvent) solution under stirring. Once in contact with water, the hydrophobic polymers and drug precipitate and self-assemble into core-shell like spherical structures in order to reduce the system's free energy. After self-assembly, the organic solvent is evaporated either by reduced-pressure evaporation, or simply by continuous mixing at atmospheric pressure if sufficiently volatile.

The instantaneous formation of particles via nanoprecipitation has been attributed to interfacial interactions between liquid phases, with water essentially displacing the organic solvent, also called the Marangoni effect [524]. Subsequently, targeting ligands may be attached to the surfactant shell of the polymer nanoparticles (Fig. 63b). Alternatively, pre-functionalized diblock copolymers containing hydrophilic targeting ligands at the outset can be used to directly assemble functionalized polymeric

nanoparticles via nanoprecipitation, salting out, or solvent evaporation (Fig. 63c). An alternative are also surface-modified polymer nanoparticles containing aptamers. Such structures were obtained, for example, by the self-assembly of an amphiphilic triblock copolymer composed of end-to-end linkage of poly(lactic-co-glycolic-acid) (PLGA), polyethyleneglycol (PEG), and the RNA A10 aptamer (Apt), which binds to the prostate-specific membrane antigen (PSMA) on the surface of prostate cancer (PCa) cells, enabling controlled drug release [525]. Also, the surface recognition tags RGD and folate have been grafted to PLGA-PEG nanoparticles using similar techniques [526]. By using neat PLGA-PEG and modified PLGA-PEG-RGD/PLGA-PEG-folate in different ratios, the density of active surface groups on the PLGA-PEG-RGD and PLGA-PEG-folate nanoparticles could be tuned in a range from 5% to over 50%. Modular assembly techniques can also be applied to produce multi-ligand targeting nanoparticles using longer peptide recognition sequences, RNA aptamers, DNA aptamers and antibodies [520].

Zwitterionic polymers such as poly(carboxybetaine) have also been recognized as a promising class of shell forming polymers owing to their higher chemical stability and weaker interactions with proteins over short and long time scales in comparison to polyethylene glycol (Fig. 64) [527–529]. Excellent stability to aggregation in serum with poly(carboxybetaine) (PCB) coating was attributed to an increase in the surface packing density of non-fouling groups, as well as steric repulsion from the flexible polymer brush surface [529]. Zwitterionic materials are highly resistant to protein adsorption because they form a strong hydration layer via electrostatic interactions and via hydrogen bonds [530] whereas hydrophilic and neutral PEG forms a hydration layer via hydrogen bonds only. Drug-containing PLGA-PCB nanoparticles could also be further modified so that each carboxylate anion is paired with a cationic ammonium group containing a cell-targeting ligand that attaches via an amide bond (Fig. 64) [527]. The use of block copolymers with sharp polarity differences for the preparation of PLGA-PCB nanoparticles provided extraordinary stability due to the strong hydration layer created by the PCB shells that stabilized the hydrophobic PLGA cores.

Molecular dynamics simulations also provided details of the structural and dynamic properties of water molecules near zwitterionic phosphorylcholine (PC) and nonionic (ethylene glycol)$_4$ self-assembled monolayers (SAMs) [531]. The results indicate that water molecules near zwitterionic SAMs bind to the surface stronger than near nonionic oligoethylene glycol SAMs, indicating a stronger repulsive force against protein adsorption. Water molecules near the zwitterionic SAMs have lower mobility and wider dipole orientation distribution than those near oligoethylene glycol SAMs [532].

Other options of cell-targeting nanostructures for drug delivery include core-shell nanoparticles [533], particle-supported lipid bilayer nanocapsules [148], as well as hierarchically ordered nanostructures [534,535].

7.1.5. *Surfactant modification and blood brain barrier*

Common features of many surface coating materials in nanomedicine are high flexibility and high hydrophilicity [520,536]. In addition to PEG and zwitterionic polymers, polysaccharides such as dextran, polysialic acid, hyaluronic acid, chitosan, heparin, polyethylene oxide (PEO), polyvinyl pyrrolidone (PVP), poly(vinyl) alcohol (PVA), polyacrylamide (Pam), and PEG-based copolymers such as poloxamer, poloxamine, polysorbate (Tween-80) and lauryl ethers (Brij-35) have been used as surface coating materials to deliver stealth properties to nanocarrier systems [517,536]. Recent studies also reported that the passage of the blood-brain barrier greatly depends on the type of surfactants rather than nanoparticle size and surface charge (Fig. 65) [537]. Polybutylcyanoacrylate (PBCA) nanoparticles of different size, surface charge, and surfactant modification were fluorescently labeled (Fig. 65a), injected into rats, and subsequent accumulation monitored in the retina of the eye to assess passage of the blood-brain barrier (Fig. 65b and c). The results demonstrate that neither size nor charge, but particle surface modification of PBCA nanoparticles

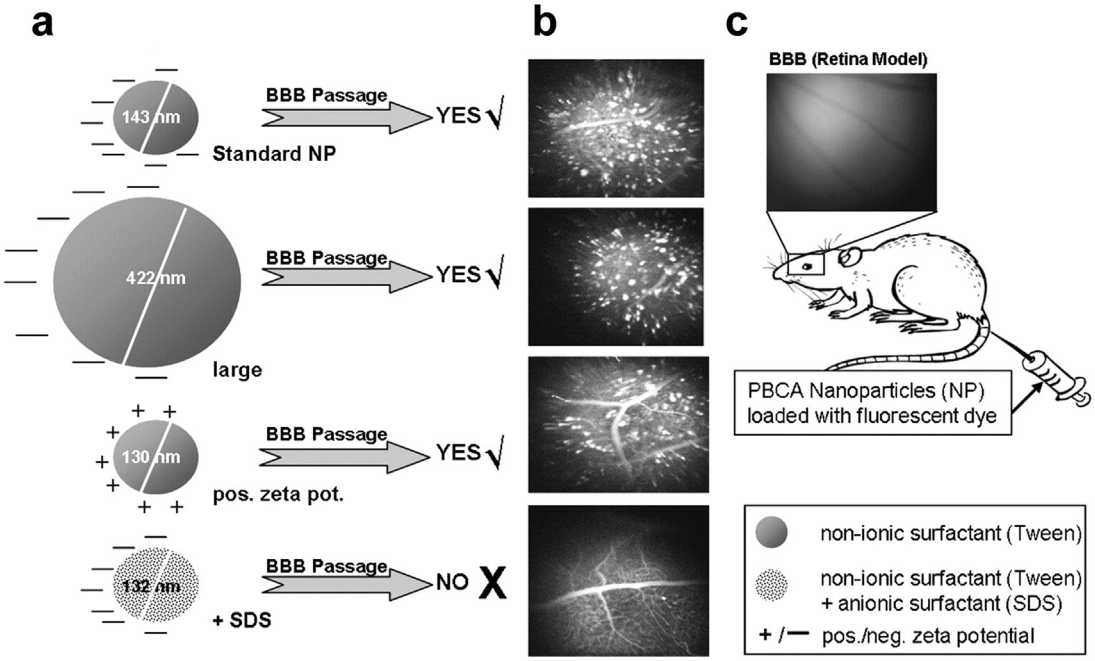

Fig. 65. The passage of the blood brain barrier (BBB) depends on surfactants applied to polymeric nanoparticles while the size and zeta-potential of the nanoparticles were found to play a lesser role. (a) Polybutylcyanoacrylate (PBCA) nanoparticles of different size with net positively charged, neutral, and net negatively charged surfactants were fluorescently labeled. (b) Passage through the BBB was monitored by accumulation in the retina of rats. Anionic surfactants (SDS) reduced passage of the BBB. (c) Method of injection of the fluorescent nanoparticles and monitoring accumulation in the retina for the assessment of the passage of the blood brain barrier. (Adapted with permission from Ref. [537].)

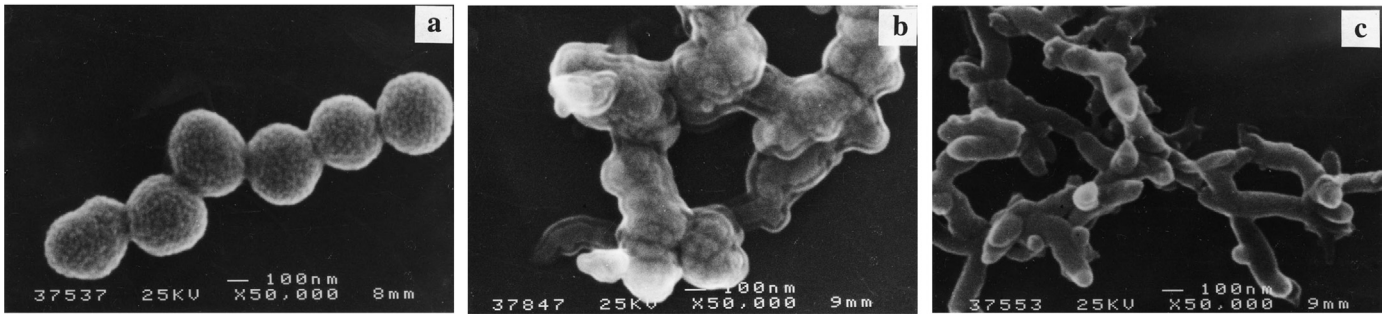

Fig. 66. Polyaniline particles formed upon dispersion polymerization of aniline hydrochloride at different temperatures. (a) 0 °C. (b) 20 °C. (c) 40 °C. (Adapted with permission from Ref. [544].)

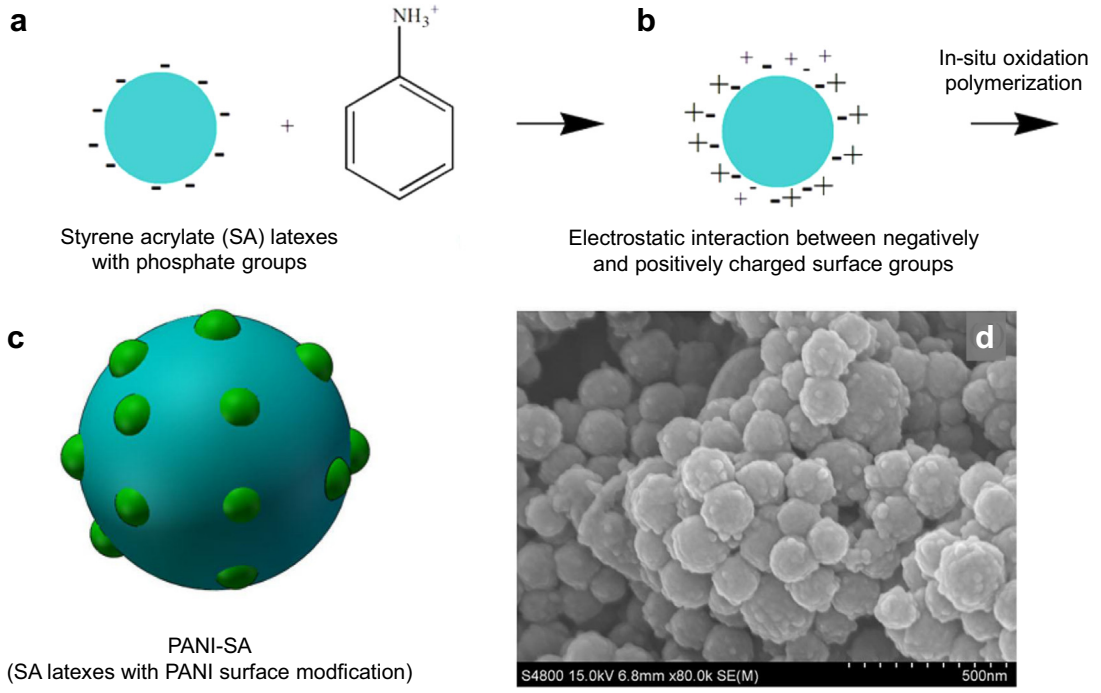

Fig. 67. Schematic synthesis and SEM images of polyaniline (PANI)-poly(styrene acrylate) (SA) latexes. (a) Poly(styrene-acrylate) particles with phosphate functional groups react with aniline hydrochloride. (b) Charged precursors with aniline cations attached to the SA particle surface are formed. (c) In-situ oxidation polymerization leads to the formation of PANI-SA composite latex particles of ~100 nm size. (d) SEM image of nanosized PANI-SA composite latex particles. The particles improve the consistency of PANI in polymer matrices and enable the application of PANI in water-based coatings for corrosion protection. (Adapted with permission from Ref. [266].)

was the major factor determining passage of the blood-brain barrier. Non-ionic surfactants (Tween80, utensolAT80, Tween20, Brij35) enhanced brain uptake while addition of anionic surfactants (sodium dodecylsulfate) reduced passage of the blood-brain barrier. Accordingly, polymeric nanoparticles can be designed to specifically enhance drug delivery to the brain or, alternatively, to prevent brain penetration to reduce unwanted effects of specific drugs, or to prevent environmental nanoparticles from entering tissue of the central nervous system.

7.2. *Polymeric nanoparticles in protective coatings*

Polymeric nanoparticles are extensively applied in paints and coatings [55,266,267,499,500,538]. A common function of coatings is corrosion protection, which is enhanced by electrically conducting polymer particles such as polyaniline (PANI) (Fig. 66) [54,539]. Passivation of stainless steel, for example, can be achieved by applying a potential of about 0.1 V versus a saturated calomel electrode in the presence of PANI particle and fiber coatings, leading to the formation of a more stable oxide layer consisting of α-Fe_2O_3 and Fe_3O_4 [54,540]. PANI has been extensively studied due to ease of preparation, environmental stability, and tunable electrical properties [540–542]. Like most other conducting polymers such as polypyrrole, polyphenylene vinylene, and polyacetylene, however, PANI is hard to process due to insolubility in water and conventional solvents, which limits its use in coating applications [543]. Dispersion polymerization of aniline in aqueous medium leads to PANI particles from well-defined spheres to coral-like objects by changing polymerization temperature and use of additives (Fig. 66) [544]. PANI nanoparticles as small as 2–3 nm were prepared by oxidative polymerization of aniline in dilute and semi-dilute solutions of sodium poly(styrene sulfonate) (PSSNa) [545], and nanospheres of 4 nm in diameter by microemulsion polymerization in the presence of the cationic surfactant octyltrimethyl ammonium bromide [546]. The size of the PANI nanoparticles is controllable through the chosen surfactant concentration, surfactant spacer length, and polymerization temperature. Furthermore, water-dispersible PANI-PSS nanoparticles with an average diameter of 30 nm have been reported and applied in the fabrication of ink-jet printed chemical sensors [547].

Recently, nanosized PANI-poly(styrene-acrylate) composite latexes have been prepared for water-based coatings (Fig. 67) [266].

Core styrene acrylate latexes with negatively charged phosphate surface groups were subjected to a solution of aniline hydrochloride to form a core-shell structure (Fig. 67a and b). The salts were then exposed to oxidation and polymerization (Fig. 67c), leading to styrene acrylate latexes with small PANI domains on the particle surface (Fig. 67d). The styrene acrylate-PANI composite particles improve the miscibility of PANI in polymer matrices in water-based anti-corrosion coatings.

8. Summary, challenges, and opportunities

Nanostructures with specific surface modifications are a pillar of today's nanoscience and bioscience. A wide chemical variety of nanoparticles including metals, chalcogenides, polymers, as well as complex multi-shell, multi-ligand nanostructures containing elements from across the periodic table play a major role in healthcare, biotechnology, energy sciences, catalysis, advanced materials, as well as in natural bio- and ecosystems. Fundamental techniques for grafting of ligands, functionalization of multiple ligand shells, and introduction of cell targeting properties are available and in principle understood. A variety of methods for adjusting surface polarity by use of ionic, hydrophilic (e.g. PEO), hydrophobic (alkyl), aromatic, and multi-block ligands has been extensively tested and is routinely applied. Chemical reactions at nanoparticle surfaces are known that enable remarkable control over surfactant architecture over multiple layers. Catalysis on surface modified nanoparticle can be highly efficient. However, atomic-level details of the grafting density, the dynamics of surfactants, their role in certain chemical reactions, as well as charge transfer remain difficult to explore. The controlled assembly of functionalized nanoparticles into superstructures and precisely guided interactions of nanoparticle-attached ligands with cell surface receptors rely heavily on trial-and-error studies to-date.

The mechanisms of non-covalent interactions of surfactants with inorganic substrates, including soft epitaxial interactions with metals as well as the strong dependence on surface chemistry and pH values on oxide surfaces have become known in molecular and atomic detail in the last decade. A long history of validated experimental data is thereby also available and can be utilized. In several instances, atomically resolved insights into surface binding and related properties are increasingly driven by advances in molecular simulation along with experimental techniques, spanning the range from below nanometer to the large nanometer scale. Nucleation and growth of nanomaterials supported by surfactants and other growth directing agents has been understood in atomic resolution in specific cases.

Intense experimental and computational studies using suitable existing techniques, however, are still required to explore the plethora of nanoparticle/surfactant interfaces that remain unknown in details. Open questions include insights into the kinetics of nanoparticle formation, surfactants specificity to higher index ($h\ k\ l$) facets, and the role of surfactants in interfacial processes over the course of shape evolution from seed crystal to final nanostructure and nanostructure assemblies. Thermodynamic properties of modified nanoparticles along such paths are often accessible from simulation, although they may not be the relevant driving factor to understand nanoparticle shape. Mechanistic hypotheses, the estimation of activation energies, and use of other suitable descriptors of competing processes plays a critical role. The prediction of nanoparticle formation, hydration reactions, dissolution, degradation, surface catalysis, and assembly of large numbers of surfactant-modified nanoparticles into spatially organized superstructures is a multi-scale problem. First attempts in chemical accuracy have typically been limited to the scale of nanometers and nanoseconds, and it is anticipated that highly resolved measurements and realistic modeling techniques from the nanometer scale to the micrometer scale will enable new breakthroughs in the synthesis of functional metals, alloys, chalcogenides, layered materials, cement, polymer nanoparticles, and naturally inspired materials (artificial bone, carbonates/nacre, and silica).

In particular, scarce information is currently available on nanoparticles and nanostructured substrates that exhibit dynamic surfaces and interfacial regions that can be easily assembled and disassembled by changes in pH or ionic strength such as apatites and carbonates. Understanding biological and biocatalytic control via proteins, enzymes, and components in the extracellular matrix at molecular and atomic level remains largely an enigma. Therefore, discoveries by advanced imaging techniques, bioassays, and simulation to control dynamic, reversible assembly and surface decoration processes of such nanostructures can have great payoffs to understand biological mineralization, calcification, skeletal diseases, and contribute fundamental medical insight.

The next years and decades may also see the emergence of new nanomaterials with exciting optical, electrical, mechanical and other functional properties, similar to the prior discovery of the various forms of carbon, the extensive use of self-assembled thiol monolayers on nanoparticles, and recent interest in semiconducting layered materials. The decoration of such novel nanostructures with surfactants to tune solubility, protect from degradation, introduce labels for imaging, attach cell-targeting ligands, and modulate the assembly into superstructures is likely to play an essential role. Available methods and understanding of known surface-modified nanostructures today is expected to accelerate such developments.

Acknowledgements

This work was supported by the National Science Foundation (DMREF-1623947, and CBET-1530790), AFOSR (FA9550-14-1-0194), ONR-MURI (N00014-14-1-0675), ACS-PRF (54135-ND10), Procter & Gamble, Corning, Inc., and the University of Colorado-Boulder.

References

[1] R.A. Schoonheydt, C.T. Johnston, in: M.F. Brigatti, A. Mottana (Eds.), The Surface Properties of Clay Minerals, The European Mineralogical Union, 2011.
[2] P.J.M. Smeets, K.R. Cho, R.G.E. Kempen, N. Sommerdijk, J.J. De Yoreo, Nat. Mater. 14 (2015) 394–399.
[3] J.R. Xavier, T. Thakur, P. Desai, M.K. Jaiswal, N. Sears, E. Cosgriff-Hernandez, R. Kaunas, A.K. Gaharwar, ACS Nano 9 (2015) 3109–3118.
[4] M. Folmsbee, G. Howard, M. McAlister, Biologicals 38 (2010) 214–217.
[5] P.D. Howes, R. Chandrawati, M.M. Stevens, Science 346 (2014) 1247390.
[6] J. Nicolas, S. Mura, D. Brambilla, N. Mackiewicz, P. Couvreur, Chem. Soc. Rev. 42 (2013) 1147–1235.
[7] Soaps and Detergents, The Soap and Detergent Association, Washington, DC, 1994.
[8] Oxford Dictionary of English, Oxford University Press, Oxford, 2010.
[9] ⟨http://www.dictionary.com/browse/surfactant⟩, 2016.
[10] M.S.H. Boutilier, J. Lee, V. Chambers, V. Venkatesh, R. Karnik, PLoS One 9 (2014) 0089934.
[11] A.B. Pandit, J.K. Kumar, in: J.M. Prausnitz (Ed.), Annual Review of Chemical and Biomolecular Engineering, Vol 6, 2015, pp. 217–246.
[12] F. Steiner, B. Scherer, Electrophoresis 26 (2005) 1996–2004.
[13] G. Karlsson, S. Winge, Protein Expr. Purif. 28 (2003) 196–201.
[14] A. Méndez, E. Bosch, M. Rosés, U.D. Neue, J. Chromatogr. A 986 (2003) 33–44.
[15] H. Heinz, Curr. Opin. Chem. Eng. 11 (2016) 34–41.
[16] G.P. Smith, T.R. Gingrich, Biotechniques 39 (2005) 879–884.
[17] K. Ohta, H. Monma, S. Takahashi, J. Biomed. Mater. Res. 55 (2001) 409–414.
[18] Tonminerale und Tone, Steinkopf, Darmstadt, Germany, 1992.
[19] H. Van Olphen, An Introduction to Clay Colloidal Chemistry, Wiley, New York, 1977.
[20] G. Sposito, The Chemistry of Soils, 2nd ed., Oxford University Press, USA, 2008.

[21] S. Mattson, J. Agric. Res. 33 (1926) 553–567.
[22] U. Hofmann, J. Endell, Angew. Chem. 52 (1939) 708–709.
[23] K. Vogt, H.M. Koster, Clay Miner. 13 (1978) 25–43.
[24] H. Suquet, C. De. La Calle, H. Pezerat, Clays Clay Miner. 23 (1975) 1–9.
[25] G. Lagaly, A. Weiss, Kolloid Z. Z. Polym., 243, 1971, pp. 48–55.
[26] K.P. Lee, The Flocculation of Veegum Suspension by Electrolytes (Ph.D. thesis), University of Utah, Salt Lake City, 1969.
[27] W. Pechhold, S. Blasenbrey, Kolloid Z. Z. Polym., 216/217, 1967, pp. 235–244.
[28] G.L. Gaines Jr., J. Phys. Chem. 61 (1957) 1408–1413.
[29] J.W. Jordan, B.J. Hook, C.M. Finlayson, J. Phys. Chem. 54 (1950) 1196–1208.
[30] G.W. Brindley, Clay Miner. 6 (1965) 91–96.
[31] G. Lagaly, A. Weiss, Kolloid Z. Z. Polym. 237 (1970) 364–368.
[32] W. Pechhold, S. Blasenbrey, Kolloid Z. Z. Polymere 241955-976, 1970.
[33] G. Lagaly (Ed.), Angew. Chem. Int. Ed., 15, 1976, pp. 575–586.
[34] G. Lagaly, I. Dekany, Adv. Colloid Interface Sci. 114-115 (2005) 189–204.
[35] C.D. Bain, E.B. Troughton, Y.T. Tao, J. Evall, G.M. Whitesides, R.G. Nuzzo, J. Am. Chem. Soc. 111 (1989) 321–335.
[36] P.E. Laibinis, G.M. Whitesides, D.L. Allara, Y.-T. Tao, A.N. Parikh, R.G. Nuzzo, J. Am. Chem. Soc. 113 (1991) 7152–7167.
[37] R.A. Vaia, R.K. Teukolsky, E.P. Giannelis, Chem. Mater. 6 (1994) 1017–1022.
[38] H. Heinz, H.J. Castelijns, U.W. Suter, J. Am. Chem. Soc. 125 (2003) 9500–9510.
[39] M.A. Osman, M. Ploetze, P. Skrabal, J. Phys. Chem. B 108 (2004) 2580–2588.
[40] J.L. Suter, D. Groen, P.V. Coveney, Adv. Mater. 27 (2015) 966–984.
[41] H. Heinz, Clay Miner. 47 (2012) 205–230.
[42] R. Dohrmann, et al., Clays Clay Miner. 60 (2012) 162–175.
[43] L.P. Meier, G. Kahr, Clays Clay Miner. 47 (1999) 386–388.
[44] I. Estrela-Lopis, S. Leporatti, S. Moya, A. Brandt, E. Donath, H. Mohwald, Langmuir 18 (2002) 7861–7866.
[45] B. Skolova, K. Hudska, P. Pullmannova, A. Kovacik, K. Palat, J. Roh, J. Fleddermann, I. Estrela-Lopis, K. Vavrova, J. Phys. Chem. B 118 (2014) 10460–10470.
[46] I. Estrela-Lopis, J.J.I. Ramos, E. Donath, S.E. Moya, J. Phys. Chem. B 114 (2010) 84–91.
[47] M. Fischlechner, et al., Soft Matter 4 (2008) 2245–2258.
[48] I. Estrela-Lopis, S. Leporatti, E. Typlt, D. Clemens, E. Donath, Langmuir 23 (2007) 7209–7215.
[49] J.C. Love, L.A. Estroff, J.K. Kriebel, R.G. Nuzzo, G.M. Whitesides, Chem. Rev. 105 (2005) 1103–1169.
[50] K. Ariga, Y. Yamauchi, G. Rydzek, Q.M. Ji, Y. Yonamine, K.C.W. Wu, J.P. Hill, Chem. Lett. 43 (2014) 36–68.
[51] D.A. Giljohann, D.S. Seferos, W.L. Daniel, M.D. Massich, P.C. Patel, C.A. Mirkin, Angew. Chem. Int. Ed. 49 (2010) 3280–3294.
[52] T. Sun, Y.S. Zhang, B. Pang, D.C. Hyun, M. Yang, Y. Xia, Angew. Chem. Int. Ed. 53 (2014) 12320–12364.
[53] R.A. Meyer, J.J. Green, Shaping the future of nanomedicine: anisotropy in polymeric nanoparticle design, (2016) WIREs Nanomed Nanobiotechnol 8, 2016, 191-207. http://dx.doi.org/10.1002/wnan.1348.
[54] N. Ahmad, A.G. MacDiarmid, Synth. Met. 78 (1996) 103–110.
[55] M. Sababi, J. Pan, P.-E. Augustsson, P.-E. Sundell, P.M. Claesson, Corros. Sci. 84 (2014) 189–197.
[56] S. Mann, Nature 332 (1988) 119–124.
[57] F. Nudelman, K. Pieterse, A. George, P.H.H. Bomans, H. Friedrich, L.J. Brylka, P.A.J. Hilbers, G. de With, N. Sommerdijk, Nat. Mater. 9 (2010) 1004–1009.
[58] L.M. Gordon, D. Joester, Nature 469 (2011) 194–197.
[59] S.J. Segvich, H.C. Smith, D.H. Kohn, Biomaterials 30 (2009) 1287–1298.
[60] G.H. Nancollas, R. Tang, R.J. Phipps, Z. Henneman, S. Gulde, W. Wu, A. Mangood, R.G.G. Russell, F.H. Ebetino, Bone 38 (2006) 617–627.
[61] H. Yazici, M.B. O'Neill, T. Kacar, B.R. Wilson, E.E. Oren, M. Sarikaya, C. Tamerler, ACS Appl. Mater. Interfaces 8 (2016) 5070–5081.
[62] U.G.K. Wegst, H. Bai, E. Saiz, A.P. Tomsia, R.O. Ritchie, Nat. Mater. 14 (2015) 23–36.
[63] D.A. Wang, S. Varghese, B. Sharma, I. Strehin, S. Fermanian, J. Gorham, D. H. Fairbrother, B. Cascio, J.H. Elisseeff, Nat. Mater. 6 (2007) 385–392.
[64] G.G. d'Ayala, A. De Rosa, P. Laurienzo, M. Malinconico, J. Biomed. Mater. Res. A 81 (2007) 811–820.
[65] S.A. Mackowiak, A. Schmidt, V. Weiss, C. Argyo, C. von Schirnding, T. Bein, C. Bräuchle, Nano Lett. 13 (2013) 2576–2583.
[66] I.I. Slowing, B.G. Trewyn, S. Giri, V.S.Y. Lin, Adv. Funct. Mater. 17 (2007) 1225–1236.
[67] S.A. Kulkarni, S.-S. Feng, Pharm. Res. 30 (2013) 2512–2522.
[68] L.E. Ibarra, L. Tarres, S. Bongiovanni, C.A. Barbero, M.J. Kogan, V.A. Rivarola, M.L. Bertuzzi, E.I. Yslas, Ecotoxicol. Environ. Saf. 114 (2015) 84–92.
[69] M. Paranjpe, C.C. Muller-Goymann, Int. J. Mol. Sci. 15 (2014) 5852–5873.
[70] F. Gai, T. Zhou, G. Chu, Y. Li, Y. Liu, Q. Huo, F. Akhtar, Dalton Trans. 45 (2016) 508–514.
[71] Y. Li, B.P. Bastakoti, M. Imura, J. Tang, A. Aldalbahi, N.L. Torad, Y. Yamauchi, Chem. Eur. J 21 (2015) 6375–6380.
[72] J.N. Israelachvili, D.J. Mitchell, B.W. Ninham, J. Chem. Soc. Faraday Trans. II 72 (1976) 1525–1568.
[73] N. Kröger, R. Deutzmann, M. Sumper, Science 286 (1999) 1129–1132.
[74] S.R. Whaley, D.S. English, E.L. Hu, P.F. Barbara, A.M. Belcher, Nature 405 (2000) 665–668.
[75] R.R. Naik, L.L. Brott, S.J. Clarson, M.O. Stone, J. Nanosci. Nanotechnol. 2 (2002) 95–100.
[76] U.O.S. Seker, B. Wilson, S. Dincer, I.W. Kim, E.E. Oren, J.S. Evans, C. Tamerler, M. Sarikaya, Langmuir 23 (2007) 7895–7900.
[77] E. Auyeung, T. Li, A.J. Senesi, A.L. Schmucker, B.C. Pals, M.O. de la Cruz, C. A. Mirkin, Nature 505 (2014) 73–77.
[78] Y. Xia, Y. Xiong, B. Lim, S.E. Skrabalak, Angew. Chem. Int. Ed. 48 (2009) 60–103.
[79] N.L. Rosi, D.A. Giljohann, C.S. Thaxton, A.K. Lytton-Jean, M.S. Han, C.A. Mirkin, Science 312 (2006) 1027–1030.
[80] N.M. Bedford, H. Ramezani-Dakhel, J.M. Slocik, B.D. Briggs, Y. Ren, A. I. Frenkel, V. Petkov, H. Heinz, R.R. Naik, M.R. Knecht, ACS Nano 9 (2015) 5082–5092.
[81] C.Y. Chiu, Y.J. Li, L.Y. Ruan, X.C. Ye, C.B. Murray, Y. Huang, Nat. Chem. 3 (2011) 393–399.
[82] S. Kango, S. Kalia, A. Celli, J. Njuguna, Y. Habibi, R. Kumar, Prog. Polym. Sci. 38 (2013) 1232–1261.
[83] W.J. Parak, D. Gerion, T. Pellegrino, D. Zanchet, C. Micheel, S.C. Williams, R. Boudreau, M.A. Le Gros, C.A. Larabell, A.P. Alivisatos, Nanotechnology 14 (2003) R15–R27.
[84] R.J. Flatt, N. Roussel, C.R. Cheeseman, J. Eur. Ceram. Soc. 32 (2012) 2787–2798.
[85] P.D. Jadzinsky, G. Calero, C.J. Ackerson, D.A. Bushnell, R.D. Kornberg, Science 318 (2007) 430–433.
[86] J.W. Miao, F. Forster, O. Levi, Phys. Rev. B 72 (2005) 052103.
[87] M.C. Scott, C.C. Chen, M. Mecklenburg, C. Zhu, R. Xu, P. Ercius, U. Dahmen, B.C. Regan, J.W. Miao, Nature 483 (2012) 444–447.
[88] R. Xu, et al., Nat. Mater. 14 (2015) 1099–1103.
[89] M.R. Langille, J. Zhang, M.L. Personick, S.Y. Li, C.A. Mirkin, Science 337 (2012) 954–957.
[90] I. Langmuir, J. Am. Ceram. Soc. 40 (1918) 1361–1403.
[91] S. Brunauer, P.H. Emmett, E. Teller, J. Am. Chem. Soc. 60 (1938) 309–319.
[92] J.N. Israelachvili, G.E. Adams, J. Chem. Soc. Faraday Trans. I 74 (1978) 975 (&).
[93] R.M. Pashley, J.N. Israelachvili, Colloids Surfaces 2 (1981) 169–187.
[94] H. Heinz, H. Koerner, K.L. Anderson, R.A. Vaia, B.L. Farmer, Chem. Mater. 17 (2005) 5658–5669.
[95] H. Heinz, R.A. Vaia, B.L. Farmer, Langmuir 24 (2008) 3727–3733.
[96] M.A. Osman, G. Seyfang, U.W. Suter, J. Phys. Chem. B 104 (2000) 4433–4439.
[97] H. Heinz, R.A. Vaia, R. Krishnamoorti, B.L. Farmer, Chem. Mater. 19 (2007) 59–68.
[98] L.H. Dubois, R.G. Nuzzo, Ann. Rev. Phys. Chem. 43 (1992) 437–463.
[99] G.D. Barmparis, K. Honkala, I.N. Remediakis, J. Chem. Phys. 138 (2013) 064702.
[100] O. Alexiadis, V.A. Harmandaris, V.G. Mavrantzas, L. Delle Site, J. Phys. Chem. C 111 (2007) 6380–6391.
[101] J.B. Schlenoff, M. Li, H. Ly, J. Am. Chem. Soc. 117 (1995) 12528–12536.
[102] G. Hahner, R. Hofer, I. Klingenfuss, Langmuir 17 (2001) 7047–7052.
[103] Y.T. Tao, J. Am. Chem. Soc. 115 (1993) 4350–4358.
[104] W.A. Hayes, D.K. Schwartz, Langmuir 14 (1998) 5913–5917.
[105] H. Heinz, U.W. Suter, Angew. Chem. Int. Ed. 43 (2004) 2239–2243.
[106] A. Badia, L. Cuccia, L. Demers, F. Morin, R.B. Lennox, J. Am. Chem. Soc. 119 (1997) 2682–2692.
[107] C. Weeraman, A.K. Yatawara, A.N. Bordenyuk, A.V. Benderskii, J. Am. Chem. Soc. 128 (2006) 14244–14245.
[108] A.N. Bordenyuk, C. Weeraman, A.K. Yatawara, H.D. Jayathilake, I. Stiopkin, Y. Liu, A.V. Benderskii, J. Phys. Chem. C 111 (2007) 8925–8933.
[109] C.A. Mirkin, R.L. Letsinger, R.C. Mucic, J.J. Storhoff, Nature 382 (1996) 607–609.
[110] R.J. Macfarlane, B. Lee, M.R. Jones, N. Harris, G.C. Schatz, C.A. Mirkin, Science 334 (2011) 204–208.
[111] J.I. Cutler, E. Auyeung, C.A. Mirkin, J. Am. Chem. Soc. 134 (2012) 1376–1391.
[112] R.J. Macfarlane, M.R. Jones, B. Lee, E. Auyeung, C.A. Mirkin, Science 341 (2013) 1222–1225.
[113] E. Auyeung, W. Morris, J.E. Mondloch, J.T. Hupp, O.K. Farha, C.A. Mirkin, J. Am. Chem. Soc. 137 (2015) 1658–1662.
[114] J.W. Park, Y.J. Park, C.H. Jun, Chem. Commun. 47 (2011) 4860–4871.
[115] S.P. Pujari, L. Scheres, A.T.M. Marcelis, H. Zuilhof, Angew. Chem. Int. Ed. 53 (2014) 6322–6356.
[116] H.C. Kolb, M.G. Finn, K.B. Sharpless, Angew. Chem. Int. Ed. 40 (2001) 2004–2021.
[117] J.E. Moses, A.D. Moorhouse, Chem. Soc. Rev. 36 (2007) 1249–1262.
[118] G. Decher, Science 277 (1997) 1232–1237.
[119] M.J. Rosen, J. Am. Oil Chem. Soc. 52 (1975) 431–435.
[120] H. Heinz, J. Phys.: Condens. Matter 26 (2014) 244105.
[121] H. Heinz, B.L. Farmer, R.B. Pandey, J.M. Slocik, S.S. Patnaik, R. Pachter, R.R. Naik, J. Am. Chem. Soc. 131 (2009) 9704–9714.
[122] J. Feng, R.B. Pandey, R.J. Berry, B.L. Farmer, R.R. Naik, H. Heinz, Soft Matter 7 (2011) 2113–2120.
[123] H. Ramezani-Dakhel, L.Y. Ruan, Y. Huang, H. Heinz, Adv. Funct. Mater. 25 (2015) 1374–1384.
[124] J.C. Ma, D.A. Dougherty, Chem. Rev. 97 (1997) 1303–1324.
[125] S.S. Kim, Z.F. Kuang, Y.H. Ngo, B.L. Farmer, R.R. Naik, ACS Appl. Mater. Interfaces 7 (2015) 20447–20453.
[126] S.V. Patwardhan, F.S. Emami, R.J. Berry, S.E. Jones, R.R. Naik, O. Deschaume, H. Heinz, C.C. Perry, J. Am. Chem. Soc. 134 (2012) 6244–6256.
[127] V. Puddu, C.C. Perry, ACS Nano 6 (2012) 6356–6363.
[128] K. Vanommeslaeghe, et al., J. Comput. Chem. 31 (2010) 671–690.
[129] H. Sun, S.J. Mumby, J.R. Maple, A.T. Hagler, J. Am. Chem. Soc. 116 (1994) 2978–2987.
[130] H. Heinz, H. Ramezani-Dakhel, Chem. Soc. Rev. 45 (2016) 412–448.

[131] E.M. Hotze, T. Phenrat, G.V. Lowry, J. Environ. Qual. 39 (2010) 1909–1924.
[132] Y.G. Sun, Y.N. Xia, Science 298 (2002) 2176–2179.
[133] B. Briggs, N. Bedford, S. Seifert, H. Koerner, H. Ramezani-Dakhel, H. Heinz, R. R. Naik, A. Frenkel, M.R. Knecht, Chem. Sci. 6 (2015) 6413–6419.
[134] Cd.M. Donega, Chem. Soc. Rev. 40 (2011) 1512–1546.
[135] L.Q. Jiang, L. Gao, J. Sun, J. Colloid Interface Sci. 260 (2003) 89–94.
[136] L. Dai, Acc. Chem. Res 46 (2013) 31–42.
[137] V. Nicolosi, M. Chhowalla, M.G. Kanatzidis, M.S. Strano, J.N. Coleman, Science 340 (2013) 1226419.
[138] Q. Wang, D. O'Hare, Chem. Rev. 112 (2012) 4124–4155.
[139] S. Barua, J.-W. Yoo, P. Kolhar, A. Wakankar, Y.R. Gokarn, S. Mitragotri, Proc. Natl. Acad. Sci. USA 110 (2013) 3270–3275.
[140] X.H. Gao, Y.Y. Cui, R.M. Levenson, L.W.K. Chung, S.M. Nie, Nat. Biotechnol. 22 (2004) 969–976.
[141] A. Kaushik, R. Kumar, S.K. Arya, M. Nair, B.D. Malhotra, S. Bhansali, Chem. Rev. 115 (2015) 4571–4606.
[142] Y. Liu, et al., J. Am. Chem. Soc. 137 (2015) 14952–14958.
[143] L. Zhu, Y. Cao, G. Cao, Biosens. Bioelectron. 54 (2014) 258–261.
[144] M. Zhang, B.-C. Yin, W. Tan, B.-C. Ye, Biosens. Bioelectron. 26 (2011) 3260–3265.
[145] K. Saha, S.S. Agasti, C. Kim, X.N. Li, V.M. Rotello, Chem. Rev. 112 (2012) 2739–2779.
[146] H. Ow, D.R. Larson, M. Srivastava, B.A. Baird, W.W. Webb, U. Wiesner, Nano Lett. 5 (2005) 113–117.
[147] J. Yao, M. Yang, Y. Duan, Chem. Rev. 114 (2014) 6130–6178.
[148] C.E. Ashley, et al., Nat. Mater. 10 (2011) 389–397.
[149] J. Llop, et al., J. Mater. Chem. B 3 (2015) 6293–6300.
[150] A. R. Collins, B. Annangi, L. Rubio, R. Marcos, M. Dorn, C. Merker, I. Estrela-Lopis, M. R. Cimpan, M. Ibrahim, E. Cimpan, M. Ostermann, A. Sauter, N. El Yamani, S. Shaposhnikov, S. Chevillard, V. Paget, R. Grall, J. Delic, F. Goñi- de-Cerio, B. Suarez-Merino, V. Fessard, K.N. Hogeveen, L.M. Fjellsbø, E. Runden Pran, T. Brzicova, J. Topinka, M. João Silva, P.E. Leite, A.R. Ribeiro, J.M. Granjeiro, R. Grafström, A. Prina-Mello, M. Dusinska, et al., High throughput toxicity screening and intracellular detection of nanomaterials, WIREs Nanomed Nanobiotechnol 9, 2017, e1413. http://dx.doi.org/10.1002/wnan.1413.
[151] X.Y. Zhou, M. Dorn, J. Vogt, D. Spemann, W. Yu, Z.W. Mao, I. Estrela-Lopis, E. Donath, C.Y. Gao, Nanoscale 6 (2014) 8535–8542.
[152] J. Llop, et al., Part. Part. Syst. Charact. 31 (2014) 24–35.
[153] C. Matthaus, T. Chernenko, J.A. Newmark, C.M. Warner, M. Diem, Biophys. J 93 (2007) 668–673.
[154] K. Klein, A.M. Gigler, T. Aschenbrenner, R. Monetti, W. Bunk, F. Jamitzky, G. Morfill, R.W. Stark, J. Schlegel, Biophys. J. 102 (2012) 360–368.
[155] C. Matthaus, A. Kale, T. Chernenko, V. Torchilin, M. Diem, Mol. Pharm. 5 (2008) 287–293.
[156] G. Romero, I. Estrela-Lopis, J. Zhou, E. Rojas, A. Franco, C.S. Espinel, A. G. Fernandez, C. Gao, E. Donath, S.E. Moya, Biomacromolecules 11 (2010) 2993–2999.
[157] G. Romero, O. Ochoteco, D.J. Sanz, I. Estrela-Lopis, E. Donath, S.E. Moya, Macromol. Biosci. 13 (2013) 903–912.
[158] A. Haase, et al., ACS Nano 5 (2011) 3059–3068.
[159] G. Romero, I. Estrela-Lopis, P. Castro-Hartmann, E. Rojas, I. Llarena, D. Sanz, E. Donath, S.E. Moya, Soft Matter 7 (2011) 6883–6890.
[160] I. Estrela-Lopis, G. Romero, E. Rojas, S.E. Moya, E. Donath, J. Phys.: Conf. Ser. 304 (2011) 012017.
[161] S.R. Euston, Curr. Opin. Colloid Interface Sci. 9 (2004) 321–327.
[162] I.-C. Yeh, J.L. Lenhart, B.C. Rinderspacher, J. Phys. Chem. C 119 (2015) 7721–7731.
[163] S.K. Ramakrishnan, M. Martin, T. Cloitre, L. Firlej, C. Gergely, J. Chem. Inf. Model 54 (2014) 2117–2126.
[164] F.S. Emami, V. Puddu, R.J. Berry, V. Varshney, S.V. Patwardhan, C.C. Perry, H. Heinz, Chem. Mater. 26 (2014) 5725–5734.
[165] Z.H. Tang, J.P. Palafox-Hernandez, W.C. Law, Z.E. Hughes, M.T. Swihart, P. N. Prasad, M.R. Knecht, T.R. Walsh, ACS Nano 7 (2013) 9632–9646.
[166] J.W. Shen, C.L. Li, N.F.A. van der Vegt, C. Peter, J. Phys. Chem. C 117 (2013) 6904–6913.
[167] T. Mori, R.J. Hamers, J.A. Pedersen, Q. Cui, J. Chem. Theor. Comput. 9 (2013) 5059–5069.
[168] K.C. Jha, H. Liu, M.R. Bockstaller, H. Heinz, J. Phys. Chem. C 117 (2013) 25969–25981.
[169] Y. Sha, T.H. Yu, B.V. Merinov, P. Shirvanian, W.A. Goddard, J. Phys. Chem. C 116 (2012) 21334–21342.
[170] R.B. Pandey, H. Heinz, J. Feng, B.L. Farmer, J.M. Slocik, L.F. Drummy, R.R. Naik, Phys. Chem. Chem. Phys. 11 (2009) 1989–2001.
[171] L. Mazeina, A. Navrotsky, Chem. Mater. 19 (2007) 825–833.
[172] Z. Li, F. Calaza, F. Gao, W.T. Tysoe, Surf. Sci. 601 (2007) 1351–1357.
[173] C. Tamerler, E.E. Oren, M. Duman, E. Venkatasubramanian, M. Sarikaya, Langmuir 22 (2006) 7712–7718.
[174] A. Muller, G. Wenz, Chem. Eur. J. 13 (2007) 2218–2223.
[175] G. Rakhmatkariev, Clays Clay Miner. 54 (2006) 402–407.
[176] H. Heinz, J. Comput. Chem. 31 (2010) 1564–1568.
[177] J. Feng, J.M. Slocik, M. Sarikaya, R.R. Naik, B.L. Farmer, H. Heinz, Small 8 (2012) 1049–1059.
[178] J.P. Allen, W. Gren, M. Molinari, C. Arrouvel, F. Maglia, S.C. Parker, Mol. Simul. 35 (2009) 584–608.
[179] S. Gomez-Grana, et al., J. Phys. Chem. Lett. 4 (2013) 2209–2216.
[180] N. Almora-Barrios, G. Novell-Leruth, P. Whiting, L.M. Liz-Marzán, N. López, Nano Lett. 14 (2014) 871–875.
[181] D. Frenkel, B. Smit, Understanding Molecular Simulation from Algorithms to Applications, Academic Press, San Diego, 2002.
[182] J. Comer, J.C. Gumbart, J. Henin, T. Lelievre, A. Pohorille, C. Chipot, J. Phys. Chem. B 119 (2015) 1129–1151.
[183] CRC Handbook of Chemistry and Physics CRC Press, Boca Raton, FL, 2015.
[184] C.T. Campbell, J.R.V. Sellers, J. Am. Chem. Soc. 134 (2012) 18109–18115.
[185] J. Schlitter, Chem. Phys. Lett. 215 (1993) 617–621.
[186] F.S. Emami, V. Puddu, R.J. Berry, V. Varshney, S.V. Patwardhan, C.C. Perry, H. Heinz, Chem. Mater. 28 (2016) 406–407.
[187] S. Corni, M. Hnilova, C. Tamerler, M. Sarikaya, J. Phys. Chem. C 117 (2013) 16990–17003.
[188] S.H.D. Lacerda, J.J. Park, C. Meuse, D. Pristinski, M.L. Becker, A. Karim, J.F. Douglas, ACS Nano 4 (2010) 365–379.
[189] S.K. Kumar, N. Jouault, B. Benicewicz, T. Neely, Macromolecules 46 (2013) 3199–3214.
[190] J. Chen, et al., Nano Lett. 5 (2005) 473–477.
[191] J.Y. Chen, B. Wiley, Z.Y. Li, D. Campbell, F. Saeki, H. Cang, L. Au, J. Lee, X.D. Li, Y.N. Xia, Adv. Mater. 17 (2005) 2255–2261.
[192] J.L. Elechiguerra, J. Reyes-Gasga, M.J. Yacaman, J. Mater. Chem. 16 (2006) 3906–3919.
[193] B. Lim, Y.J. Xiong, Y.N. Xia, Angew. Chem. Int. Ed. 46 (2007) 9279–9282.
[194] J.Z. Zhang, C. Noguez, Plasmonics 3 (2008) 127–150.
[195] G.Y. Hong, H. Heinz, R.R. Naik, B.L. Farmer, R. Pachter, ACS Appl. Mater. Interfaces 1 (2009) 388–392.
[196] C. Walkey, E.A. Sykes, W.C.W. Chan, Am. Soc. Hematol. Educ. Program Book 2009 (2009) 701–707.
[197] W.X. Niu, L. Zhang, G.B. Xu, ACS Nano 4 (2010) 1987–1996.
[198] Y.N. Tan, J.Y. Lee, D.I.C. Wang, J. Am. Chem. Soc. 132 (2010) 5677–5686.
[199] A. Kuzyk, R. Schreiber, Z.Y. Fan, G. Pardatscher, E.M. Roller, A. Hogele, F.C. Simmel, A.O. Govorov, T. Liedl, Nature 483 (2012) 311–314.
[200] K.J. Savage, M.M. Hawkeye, R. Esteban, A.G. Borisov, J. Aizpurua, J.J. Baumberg, Nature 491 (2012) 574–577.
[201] X. Ye, et al., ACS Nano 6 (2012) 2804–2817.
[202] H. Ramezani-Dakhel, P.A. Mirau, R.R. Naik, M.R. Knecht, H. Heinz, Phys. Chem. Chem. Phys. 15 (2013) 5488–5492.
[203] L.Y. Ruan, H. Ramezani-Dakhel, C. Lee, Y.J. Li, X.F. Duan, H. Heinz, Y. Huang, ACS Nano 8 (2014) 6934–6944.
[204] S. Tadepalli, Z. Kuang, Q. Jiang, K.-K. Liu, M.A. Fisher, J.J. Morrissey, E.D. Kharasch, J.M. Slocik, R.R. Naik, S. Singamaneni, Sci. Rep. 5 (2015) 16206.
[205] Q. Yue, Y. Zhang, C. Wang, X. Wang, Z. Sun, X.-F. Hou, D. Zhao, Y. Deng, J. Mater. Chem. A 3 (2015) 4586–4594.
[206] C.L. Lu, K.S. Prasad, H.L. Wu, J.A.A. Ho, M.H. Huang, J. Am. Chem. Soc. 132 (2010) 14546–14553.
[207] M.L. Personick, M.R. Langille, J. Zhang, C.A. Mirkin, Nano Lett. 11 (2011) 3394–3398.
[208] L.H. Dubois, B.R. Zegarski, R.G. Nuzzo, J. Am. Chem. Soc. 112 (1990) 570–579.
[209] L. Ruan, H. Ramezani-Dakhel, C.-Y. Chiu, E. Zhu, Y. Li, H. Heinz, Y. Huang, Nano Lett. 13 (2013) 840–846.
[210] W.R. Tyson, W.A. Miller, Surf. Sci. 62 (1977) 267–276.
[211] L.E. Firment, G.A. Somorjai, J. Chem. Phys. 66 (1977) 2901–2913.
[212] L.L. Atanasoska, J.C. Buchholz, G.A. Somorjai, Surf. Sci. 72 (1978) 189–207.
[213] A. Gupta, B. Boekfa, H. Sakurai, M. Ehara, U.D. Priyakumar, J. Phys. Chem. C 120 (2016) 17454–17464.
[214] H. Heinz, R.A. Vaia, B.L. Farmer, R.R. Naik, J. Phys. Chem. C 112 (2008) 17281–17290.
[215] M. Hnilova, E.E. Oren, U.O. Seker, B.R. Wilson, S. Collino, J.S. Evans, C. Tamerler, M. Sarikaya, Langmuir 24 (2008) 12440–12445.
[216] V. Humblot, C. Methivier, R. Raval, C.-M. Pradier, Surf. Sci. 601 (2007) 4189–4194.
[217] R.R. Naik, S.E. Jones, C.J. Murray, J.C. McAuliffe, R.A. Vaia, M.O. Stone, Adv. Funct. Mater. 14 (2004) 25–30.
[218] J.M. Slocik, M.O. Stone, R.R. Naik, Small 1 (2005) 1048–1052.
[219] J.M. Slocik, R.R. Naik, Adv. Mater. 18 (2006) 1988–1992.
[220] X. Fu, Y. Wang, L. Huang, Y. Sha, L. Gui, L. Lai, Y. Tang, Adv. Mater. 15 (2003) 902–906.
[221] R. Bhandari, M.R. Knecht, ACS Catal. 1 (2011) 89–98.
[222] M. Sarikaya, C. Tamerler, D.T. Schwartz, F. Baneyx, Ann. Rev. Mater. Res. 34 (2004) 373–408.
[223] M.A. Van Hove, R.J. Koestner, P.C. Stair, J.P. Biberian, L.L. Kesmodel, I. Bartos, G.A. Somorjai, Surf. Sci. 103 (1981) 218–238.
[224] M.A. Van Hove, R.J. Koestner, P.C. Stair, J.P. Biberian, L.L. Kesmodel, I. Bartos, G.A. Somorjai, Surf. Sci. 103 (1981) 189–217.
[225] B. Goris, S. Bals, W. Van den Broek, E. Carbo-Argibay, S. Gomez-Grana, L.M. Liz-Marzan, G. Van Tendeloo, Nat. Mater. 11 (2012) 930–935.
[226] E. Carbo-Argibay, B. Rodriguez-Gonzalez, S. Gomez-Grana, A. Guerrero-Martinez, I. Pastoriza-Santos, J. Perez-Juste, L.M. Liz-Marzan, Angew. Chem. Int. Ed. 49 (2010) 9397–9400.
[227] S.K. Meena, M. Sulpizi, Langmuir 29 (2013) 14954–14961.
[228] C.Y. Chiu, L. Ruan, Y. Huang, Chem. Soc. Rev. 42 (2013) 2512–2527.
[229] M.R. Langille, M.L. Personick, J. Zhang, C.A. Mirkin, J. Am. Chem. Soc. 134 (2012) 14542–14554.
[230] J.E. Millstone, W. Wei, M.R. Jones, H. Yoo, C.A. Mirkin, Nano Lett. 8 (2008) 2526–2529.
[231] S.K. Meena, S. Celiksoy, P. Schafer, A. Henkel, C. Sonnichsen, M. Sulpizi, Phys. Chem. Chem. Phys. 18 (2016) 13246–13254.

[232] Z.W. Quan, Y.X. Wang, J.Y. Fang, Acc. Chem. Res 46 (2013) 191–202.
[233] Y. Xiong, J.M. McLellan, Y. Yin, Y. Xia, Angew. Chem. Int. Ed. 46 (2007) 790–794.
[234] Y.J. Li, Z.W. Wang, C.Y. Chiu, L.Y. Ruan, W.B. Yang, Y. Yang, R.E. Palmer, Y. Huang, Nanoscale 4 (2012) 845–851.
[235] L.Y. Ruan, C.Y. Chiu, Y.J. Li, Y. Huang, Nano Lett. 11 (2011) 3040–3046.
[236] H. Heinz, T.-J. Lin, R.K. Mishra, F.S. Emami, Langmuir 29 (2013) 1754–1765.
[237] A.R. Roosen, R.P. McCormack, W.C. Carter, Comput. Mater. Sci. 11 (1998) 16–26.
[238] G.D. Barmparis, Z. Lodziana, N. Lopez, I.N. Remediakis, Beilstein J. Nanotechnol. 6 (2015) 361–368.
[239] G.D. Barmparis, I.N. Remediakis, Phys. Rev. B 86 (2012) 085457.
[240] K. Honkala, Z. Lodziana, I.N. Remediakis, N. Lopez, Top. Catal. 57 (2014) 14–24.
[241] G. Vile, D. Baudouin, I.N. Remediakis, C. Coperet, N. Lopez, J. Perez-Ramirez, ChemCatChem 5 (2013) 3750–3759.
[242] G. Vile, D. Albani, N. Almora-Barrios, N. Lopez, J. Perez-Ramirez, ChemCatChem 8 (2016) 21–33.
[243] E.C. Dreaden, A.M. Alkilany, X.H. Huang, C.J. Murphy, M.A. El-Sayed, Chem. Soc. Rev. 41 (2012) 2740–2779.
[244] D.L. Wang, H.L.L. Xin, R. Hovden, H.S. Wang, Y.C. Yu, D.A. Muller, F.J. DiSalvo, H.D. Abruna, Nat. Mater. 12 (2013) 81–87.
[245] F. Tournus, K. Sato, T. Epicier, T.J. Konno, V. Dupuis, Phys. Rev. Lett. 110 (2013) 055501.
[246] S. Siahrostami, et al., Nat. Mater. 12 (2013) 1137–1143.
[247] S. Kirklin, B. Meredig, C. Wolverton, Adv. Energy Mater. 3 (2013) 252–262.
[248] X.Q. Huang, E.B. Zhu, Y. Chen, Y.J. Li, C.Y. Chiu, Y.X. Xu, Z.Y. Lin, X.F. Duan, Y. Huang, Adv. Mater. 25 (2013) 2974–2979.
[249] D.L. Wang, et al., Nano Lett. 12 (2012) 5230–5238.
[250] C. Wang, N.M. Markovic, V.R. Stamenkovic, ACS Catal. 2 (2012) 891–898.
[251] R. Coppage, J.M. Slocik, B.D. Briggs, A.I. Frenkel, R.R. Naik, M.R. Knecht, ACS Nano 6 (2012) 1625–1636.
[252] R. Coppage, J.M. Slocik, B.D. Briggs, A.I. Frenkel, H. Heinz, R.R. Naik, M. R. Knecht, J. Am. Chem. Soc. 133 (2011) 12346–12349.
[253] G. Vile, N. Almora-Barrios, S. Mitchell, N. Lopez, J. Perez-Ramirez, Chem. Eur. J 20 (2014) 5926–5937.
[254] D. Albani, G. Vile, S. Mitchell, P.T. Witte, N. Almora-Barrios, R. Verel, N. Lopez, J. Perez-Ramirez, Catal. Sci. Technol. 6 (2016) 1621–1631.
[255] C.C. Chen, C. Zhu, E.R. White, C.Y. Chiu, M.C. Scott, B.C. Regan, L.D. Marks, Y. Huang, J.W. Miao, Nature 496 (2013) 74–77.
[256] C.L. Farrow, P. Juhas, J.W. Liu, D. Bryndin, E.S. Bozin, J. Bloch, T. Proffen, S.J. L. Billinge, J. Phys.-Condens. Matter 19 (2007) 335219.
[257] N.M. Bedford, Solid State Commun. 150 (2010) 1505–1508.
[258] J.-N. Zheng, S.-S. Li, X. Ma, F.-Y. Chen, A.-J. Wang, J.-R. Chen, J.-J. Feng, J. Power Sources 262 (2014) 270–278.
[259] L.Y.T. Chou, K. Zagorovsky, W.C.W. Chan, Nat. Nanotechnol. 9 (2014) 148–155.
[260] C. Ayala-Orozco, et al., ACS Nano 8 (2014) 6372–6381.
[261] C.J. Murphy, A.M. Gole, S.E. Hunyadi, J.W. Stone, P.N. Sisco, A. Alkilany, B. E. Kinard, P. Hankins, Chem. Commun. (2008) 544–557.
[262] R. Cortez, J.M. Slocik, J.E. Van Nostrand, N.J. Halas, R.R. Naik, J. Appl. Phys. 111 (2012) 124311.
[263] J.M. Slocik, J.S. Zabinski, D.M. Phillips, R.R. Naik, Small 4 (2008) 548–551.
[264] J.N. Anker, W.P. Hall, O. Lyandres, N.C. Shah, J. Zhao, R.P. Van Duyne, Nat. Mater. 7 (2008) 442–453.
[265] Y. Matsumura, H. Maeda, Cancer Res. 46 (1986) 6387–6392.
[266] F.F. Yang, A.P. Zhu, Polym. Bull. 72 (2015) 2503–2518.
[267] R.S. Jadhav, K.J. Patil, D.G. Hundiwale, P.P. Mahulikar, Polym. Adv. Technol. 22 (2011) 1620–1627.
[268] G. Gece, Corros. Sci. 50 (2008) 2981–2992.
[269] M. Sohmiya, K. Saito, M. Ogawa, Sci. Technol. Adv. Mater. 16 (2015) 054201.
[270] Y. Qiao, Q. Sun, J. Xi, H. Cui, Y. Tang, X. Wang, J. Alloy. Compd. 660 (2016) 416–422.
[271] L. Shen, Q. Che, H. Li, X. Zhang, Adv. Funct. Mater. 24 (2014) 2630–2637.
[272] B. Kang, G. Ceder, Nature 458 (2009) 190–193.
[273] Z. Luo, A.S. Poyraz, C.-H. Kuo, R. Miao, Y. Meng, S.-Y. Chen, T. Jiang, C. Wenos, S.L. Suib, Chem. Mater. 27 (2015) 6–17.
[274] V. Renugopalakrishnan, et al., J. Phys. Chem. C 118 (2014) 16710–16717.
[275] H. Li, P. Winget, J.-L. Brédas, Chem. Mater. 26 (2014) 631–646.
[276] S. Haracz, M. Hilgendorff, J.D. Rybka, M. Giersig, Nucl. Instrum. Methods Phys. Res. B 364 (2015) 120–126.
[277] D. Niu, Z. Liu, Y. Li, X. Luo, J. Zhang, J. Gong, J. Shi, Adv. Mater. 26 (2014) 4947–4953.
[278] S. Mehan, V.K. Aswal, J. Kohlbrecher, Langmuir 30 (2014) 9941–9950.
[279] Z.X. Li, J.C. Barnes, A. Bosoy, J.F. Stoddart, J.I. Zink, Chem. Soc. Rev. 41 (2012) 2590–2605.
[280] M. Ghosh, S.C. Jana, RSC Adv. 5 (2015) 105313–105318.
[281] L.T. Zhuravlev, Langmuir 3 (1987) 316–318.
[282] L.T. Zhuravlev, Colloids Surf. A 74 (1993) 71–90.
[283] L.T. Zhuravlev, Colloids Surf. A 173 (2000) 1–38.
[284] F.S. Emami, V. Puddu, R.J. Berry, V. Varshney, S.V. Patwardhan, C.C. Perry, H. Heinz, Chem. Mater. 26 (2014) 2647–2658.
[285] G.H. Bolt, J. Phys. Chem. 61 (1957) 1166–1169.
[286] J.A.G. Taylor, J.A. Hockey, J. Phys. Chem. 70 (1966) 2169–2172.
[287] T.F. Tadros, J. Lyklema, J. Electroanal. Chem. Interfacial Electrochem 17 (1968) 267–275.
[288] D.E. Yates, T.W. Healy, J. Colloid Interface Sci. 55 (1976) 9–19.
[289] S.K. Milonjić, Colloids Surf. 23 (1987) 301–312.
[290] R. Zerrouk, A. Foissy, R. Mercier, Y. Chevallier, J.-C. Morawski, J. Colloid Interface Sci. 139 (1990) 20–29.
[291] W.A. House, D.R. Orr, J. Chem. Soc. Faraday Trans. 88 (1992) 233–241.
[292] C. Dorémieux-Morin, L. Heeribout, C. Dumousseaux, J. Fraissard, H. Hommel, A.P. Legrand, J. Am. Ceram. Soc. 118 (1996) 13040–13045.
[293] J. Sonnefeld, J. Colloid Interface Sci. 183 (1996) 597–599.
[294] T.H. Muster, C.A. Prestidge, R.A. Hayes, Colloids Surf. A 176 (2001) 253–266.
[295] J.-B. Donnet, H. Balard, N. Nedjari, B. Hamdi, H. Barthel, T. Gottschalk-Gaudig, J. Colloid Interface Sci. 328 (2008) 15–19.
[296] V. Puddu, C.C. Perry, Langmuir 30 (2014) 227–233.
[297] W. Li, D. Zhao, Adv. Mater. 25 (2013) 142–149.
[298] C.A.R. Costa, C.A.P. Leite, F. Galembeck, J. Phys. Chem. B 107 (2003) 4747–4755.
[299] W. Stober, A. Fink, E. Bohn, J. Colloid Interface Sci. 26 (1968) 62–69.
[300] U. Diebold, Surf. Sci. Rep. 48 (2003) 53–229.
[301] M.L. Machesky, et al., Langmuir 24 (2008) 12331–12339.
[302] J. Schneider, L.C. Ciacchi, J. Am. Chem. Soc. 134 (2012) 2407–2413.
[303] P.J. Hotchkiss, S.C. Jones, S.A. Paniagua, A. Sharma, B. Kippelen, N. R. Armstrong, S.R. Marder, Acc. Chem. Res 45 (2012) 337–346.
[304] A.F. Holleman, E. Wiberg, Inorganic Chemistry, Academic Press, New York, 1995.
[305] P.F. Roach, D. Perry, C. C, J. Am. Chem. Soc. 128 (2006) 3939–3945.
[306] K. Moritsugu, T. Terada, A. Kidera, J. Am. Chem. Soc. 134 (2012) 7094–7101.
[307] K. Ostermeir, M. Zacharias, Biochim. Biophys. Acta-Prot. Proteom. 1834 (2013) 847–853.
[308] S.V. Patwardhan, S.J. Clarson, C.C. Perry, Chem. Commun. (2005) 1113–1121.
[309] W.E.G. Muller, H.C. Schroder, Z. Burghard, D. Pisignano, X.H. Wang, Chem. Eur. J 19 (2013) 5790–5804.
[310] E.E. Oren, R. Notman, I.W. Kim, E.J. Spencer, T.R. Walsh, R. Samudrala, C. Tamerler, M. Sarikaya, Langmuir 26 (2010) 11003–11009.
[311] E.E. Oren, C. Tamerler, D. Sahin, M. Hnilova, U.O.S. Seker, M. Sarikaya, R. Samudrala, Bioinformatics 23 (2007) 2816–2822.
[312] E. Eteshola, L.J. Brillson, S.C. Lee, Biomol. Eng. 22 (2005) 201–204.
[313] R.R. Naik, S.J. Stringer, G. Agarwal, S.E. Jones, M.O. Stone, Nat. Mater. 1 (2002) 169–172.
[314] C. Tamerler, M. Sarikaya, Acta Biomater. 3 (2007) 289–299.
[315] U.-Y. Jung, J.-W. Park, E.-H. Han, S.-G. Kang, S. Lee, C.-H. Jun, Chem. Asian J. 6 (2011) 638–645.
[316] Y. Li, L. Schadler, B. Benicewicz, in: C. Barner-Kowollik (Ed.), Handbook of RAFT Polymerization, Wiley-VCH, Weinheim, Germany, 2008, pp. 423–453.
[317] J. Lee, et al., Small 4 (2008) 143–152.
[318] J. Lee, et al., Small 1 (2005) 744–753.
[319] X.F. Ding, J.Z. Zhao, Y.H. Liu, H.B. Zhang, Z.C. Wang, Mater. Lett. 58 (2004) 3126–3130.
[320] P.D. Cozzoli, A. Kornowski, H. Weller, J. Am. Chem. Soc. 125 (2003) 14539–14548.
[321] Y. Xie, et al., ACS Nano 7 (2013) 7352–7369.
[322] S. Guragain, B.P. Bastakoti, V. Malgras, K. Nakashima, Y. Yamauchi, Chem. Eur. J. 21 (2015) 13164–13174.
[323] V. Malgras, Q.M. Ji, Y. Kamachi, T. Mori, F.K. Shieh, K.C.W. Wu, K. Ariga, Y. Yamauchi, Bull. Chem. Soc. Jpn. 88 (2015) 1171–1200.
[324] B.P. Bastakoti, S. Ishihara, S.-Y. Leo, K. Ariga, K.C.W. Wu, Y. Yamauchi, Langmuir 30 (2014) 651–659.
[325] S.H. Ko, D. Lee, H.W. Kang, K.H. Nam, J.Y. Yeo, S.J. Hong, C.P. Grigoropoulos, H. J. Sung, Nano Lett. 11 (2011) 666–671.
[326] Y.F. Lu, H.Y. Fan, A. Stump, T.L. Ward, T. Rieker, C.J. Brinker, Nature 398 (1999) 223–226.
[327] D.Y. Zhao, J.L. Feng, Q.S. Huo, N. Melosh, G.H. Fredrickson, B.F. Chmelka, G. D. Stucky, Science 279 (1998) 548–552.
[328] G.S. Attard, J.C. Glyde, C.G. Goltner, Nature 378 (1995) 366–368.
[329] S. Che, Z. Liu, T. Ohsuna, K. Sakamoto, O. Terasaki, T. Tatsumi, Nature 429 (2004) 281–284.
[330] S.-H. Wu, Y. Hung, C.-Y. Mou, Chem. Commun. 47 (2011) 9972–9985.
[331] Q. He, Y. Gao, L. Zhang, Z. Zhang, F. Gao, X. Ji, Y. Li, J. Shi, Biomaterials 32 (2011) 7711–7720.
[332] B. Sun, J. Horvat, H.S. Kim, W.S. Kim, J. Ahn, G.X. Wang, J. Phys. Chem. C 114 (2010) 18753–18761.
[333] K.M.L. Taylor, J.S. Kim, W.J. Rieter, H. An, W.L. Lin, W.B. Lin, J. Am. Chem. Soc. 130 (2008) 2154–2155.
[334] F. Hoffmann, M. Cornelius, J. Morell, M. Froba, Angew. Chem. Int. Ed. 45 (2006) 3216–3251.
[335] L.Y. Jiang, X.L. Wu, Y.G. Guo, L.J. Wan, J. Phys. Chem. C 113 (2009) 14213–14219.
[336] Y. Sun, J.H. Seo, C.J. Takacs, J. Seifter, A.J. Heeger, Adv. Mater. 23 (2011) 1679–1683.
[337] C.E. Small, S. Chen, J. Subbiah, C.M. Amb, S.-W. Tsang, T.-H. Lai, J.R. Reynolds, F. So, Nat. Photonics 6 (2012) 115–120.
[338] M. Gratzel, Inorg. Chem. 44 (2005) 6841–6851.
[339] F. De Angelis, S. Fantacci, A. Selloni, M. Gratzel, M.K. Nazeeruddin, Nano Lett. 7 (2007) 3189–3195.
[340] A. Hagfeldt, G. Boschloo, L.C. Sun, L. Kloo, H. Pettersson, Chem. Rev. 110 (2010) 6595–6663.
[341] S.N. Habisreutinger, T. Leijtens, G.E. Eperon, S.D. Stranks, R.J. Nicholas, H.J. Snaith, Nano Lett. 14 (2014) 5561–5568.
[342] N.J. Jeon, J.H. Noh, W.S. Yang, Y.C. Kim, S. Ryu, J. Seo, S.I. Seok, Nature 517

(2015) 476–480.
[343] A.L. Rodarte, B.H. Cao, H. Panesar, R.J. Pandolfi, M. Quint, L. Edwards, S. Ghosh, J.E. Hein, L.S. Hirst, Soft Matter 11 (2015) 1701–1707.
[344] Z.B. Zhuang, X.T. Lu, Q. Peng, Y.D. Li, J. Am. Chem. Soc. 132 (2010) 1819–1821.
[345] A.J. Morris-Cohen, M. Malicki, M.D. Peterson, J.W.J. Slavin, E.A. Weiss, Chem. Mater. 25 (2013) 1155–1165.
[346] J.H. Bang, P.V. Kamat, ACS Nano 3 (2009) 1467–1476.
[347] M.O. Abdalla, P. Karna, H.K. Sajja, H. Mao, C. Yates, T. Turner, R. Aneja, J. Control. Release 149 (2011) 314–322.
[348] A. Jordan, et al., J. Magn. Magn. Mater. 225 (2001) 118–126.
[349] H.A. Meng, M. Liong, T.A. Xia, Z.X. Li, Z.X. Ji, J.I. Zink, A.E. Nel, ACS Nano 4 (2010) 4539–4550.
[350] J. Andersson, J. Rosenholm, S. Areva, M. Linden, Chem. Mater. 16 (2004) 4160–4167.
[351] J.M. Tarascon, M. Armand, Nat. Biotechnol. 414 (2001) 359–367.
[352] J. Xu, J. Wu, L. Luo, X. Chen, H. Qin, V. Dravid, S. Mi, C. Jia, J. Power Sources 274 (2015) 816–822.
[353] T. Kuila, S. Bose, P. Khanra, A.K. Mishra, N.H. Kim, J.H. Lee, Biosens. Bioelectron. 26 (2011) 4637–4648.
[354] M. Osada, T. Sasaki, Adv. Mater. 24 (2012) 210–228.
[355] R.Z. Ma, T. Sasaki, Adv. Mater. 22 (2010) 5082–5104.
[356] M. Liu, Y. Ishida, Y. Ebina, T. Sasaki, T. Hikima, M. Takata, T. Aida, Nature 517 (2015) 68–72.
[357] P. Podsiadlo, et al., Science 318 (2007) 80–83.
[358] D.R. Paul, L.M. Robeson, Polymer 49 (2008) 3187–3204.
[359] T. Ramanathan, et al., Nat. Nanotechnol. 3 (2008) 327–331.
[360] C. Zhu, X. Liu, X. Yu, N. Zhao, J. Liu, J. Xu, Carbon 50 (2012) 235–243.
[361] W.-W. Xiong, J. Miao, K. Ye, Y. Wang, B. Liu, Q. Zhang, Angew. Chem. Int. Ed. 54 (2015) 546–550.
[362] C.N.R. Rao, K. Biswas, K.S. Subrahmanyam, A. Govindaraj, J. Mater. Chem. 19 (2009) 2457–2469.
[363] G. Wu, Z. Li, X. Zhang, G. Lu, J. Phys. Chem. Lett. 5 (2014) 2649–2656.
[364] L. Guan, K. Suenaga, S. Iijima, Nano Lett. 8 (2008) 459–462.
[365] M.F.L. De Volder, S.H. Tawfick, R.H. Baughman, A.J. Hart, Science 339 (2013) 535–539.
[366] Y. Xue, D. Yu, L. Dai, R. Wang, D. Li, A. Roy, F. Lu, H. Chen, Y. Liu, J. Qu, Phys. Chem. Chem. Phys. 15 (2013) 12220–12226.
[367] Y. Xue, J. Liu, H. Chen, R. Wang, D. Li, J. Qu, L. Dai, Angew. Chem.-Int. 51 (2012) 12124–12127.
[368] S. Park, R.S. Ruoff, Nat. Nanotechnol. 4 (2009) 217–224.
[369] I.-Y. Jeon, H.-J. Choi, S.-M. Jung, J.-M. Seo, M.-J. Kim, L. Dai, J.-B. Baek, J. Am. Chem. Soc. 135 (2013) 1386–1393.
[370] G. Huang, T. Chen, W. Chen, Z. Wang, K. Chang, L. Ma, F. Huang, D. Chen, J.Y. Lee, Small 9 (2013) 3693–3703.
[371] Y.J. Li, E.B. Zhu, T. McLouth, C.Y. Chiu, X.Q. Huang, Y. Huang, J. Am. Chem. Soc. 134 (2012) 12326–12329.
[372] D. Chen, H. Zhu, T. Liu, ACS Appl. Mater. Interfaces 2 (2010) 3702–3708.
[373] Y. Li, X.B. Fan, J.J. Qi, J.Y. Ji, S.L. Wang, G.L. Zhang, F.B. Zhang, Nano Res. 3 (2010) 429–437.
[374] B. Wu, D. Geng, Z. Xu, Y. Guo, L. Huang, Y. Xue, J. Chen, G. Yu, Y. Liu, Nat. Asia Mater. 5 (2013) e36.
[375] Y. Cui, S.N. Kim, S.E. Jones, L.L. Wissler, R.R. Naik, M.C. McAlpine, Nano Lett. 10 (2010) 4559–4565.
[376] S.N. Kim, Z. Kuang, J.M. Slocik, S.E. Jones, Y. Cui, B.L. Farmer, M.C. McAlpine, R. R. Naik, J. Am. Chem. Soc. 133 (2011) 14480–14483.
[377] M.J. Pender, L.A. Sowards, J.D. Hartgerink, M.O. Stone, R.R. Naik, Nano Lett. 6 (2006) 40–44.
[378] G.P. Smith, V.A. Petrenko, Chem. Rev. 97 (1997) 391–410.
[379] J.K. Scott, G.P. Smith, Science 249 (1990) 386–390.
[380] B. Akdim, R. Pachter, S.S. Kim, R.R. Naik, T.R. Walsh, S. Trohalaki, G. Hong, Z. Kuang, B.L. Farmer, ACS Appl. Mater. Interfaces 5 (2013) 7470–7477.
[381] Z.F. Kuang, S.N. Kim, W.J. Crookes-Goodson, B.L. Farmer, R.R. Naik, ACS Nano 4 (2010) 452–458.
[382] C.M. Welch, A.N. Camden, S.A. Barr, G.M. Leuty, G.S. Kedziora, R.J. Berry, J. Chem. Phys. 143 (2015) 045104.
[383] A.C. Hunter, J.K.M. Sanders, J. Am. Chem. Soc. 112 (1990) 5525–5534.
[384] Z.X. Yang, Z.G. Wang, X.L. Tian, P. Xiu, R.H. Zhou, J. Chem. Phys. 136 (2012) 025103.
[385] H.C. Schniepp, J.L. Li, M.J. McAllister, H. Sai, M. Herrera-Alonso, D. H. Adamson, R.K. Prud'homme, R. Car, D.A. Saville, I.A. Aksay, J. Phys. Chem. B 110 (2006) 8535–8539.
[386] T. Vy, R. Soklaski, Y. Liang, L. Yang, Phys. Rev. B 89 (2014) 235319.
[387] B. Radisavljevic, A. Radenovic, J. Brivio, V. Giacometti, A. Kis, Nat. Nanotechnol. 6 (2011) 147–150.
[388] Q.H. Wang, K. Kalantar-Zadeh, A. Kis, J.N. Coleman, M.S. Strano, Nat. Nanotechnol. 7 (2012) 699–712.
[389] M. Chhowalla, H.S. Shin, G. Eda, L.-J. Li, K.P. Loh, H. Zhang, Nat. Chem. 5 (2013) 263–275.
[390] D. Jariwala, V.K. Sangwan, L.J. Lauhon, T.J. Marks, M.C. Hersam, ACS Nano 8 (2014) 1102–1120.
[391] P. Afanasiev, G.F. Xia, G. Berhault, B. Jouguet, M. Lacroix, Chem. Mater. 11 (1999) 3216–3219.
[392] R.J. Smith, et al., Adv. Mater. 23 (2011) 3944–3948.
[393] P. Sun, W. Zhang, X. Hu, L. Yuan, Y. Huang, J. Mater. Chem. A 2 (2014) 3498–3504.
[394] K. Chang, W. Chen, ACS Nano 5 (2011) 4720–4728.
[395] H.I. Karunadasa, E. Montalvo, Y. Sun, M. Majda, J.R. Long, C.J. Chang, Science 335 (2012) 698–702.
[396] T. Wang, H. Zhu, J. Zhuo, Z. Zhu, P. Papakonstantinou, G. Lubarsky, J. Lin, M. Li, Anal. Chem. 85 (2013) 10289–10295.
[397] M.A. Bizeto, A.L. Shiguihara, V.R.L. Constantino, J. Mater. Chem. 19 (2009) 2512–2525.
[398] F. Geng, R. Ma, A. Nakamura, K. Akatsuka, Y. Ebina, Y. Yamauchi, N. Miyamoto, Y. Tateyama, T. Sasaki, Nat. Commun. 4 (2013) 1632.
[399] F. Geng, R. Ma, T. Sasaki, Acc. Chem. Res 43 (2010) 1177–1185.
[400] T. Sasaki, M. Watanabe, J. Am. Chem. Soc. 120 (1998) 4682–4689.
[401] T. Sasaki, F. Kooli, M. Iida, Y. Michiue, S. Takenouchi, Y. Yajima, F. Izumi, B. C. Chakoumakos, M. Watanabe, Chem. Mater. 10 (1998) 4123–4128.
[402] Hydrous Phyllosilicates Mineralogical Society of America, Chelsea, MI, 1988.
[403] M.A. Osman, Jr.E.P. Rupp, U.W. Suter, J. Mater. Chem. 15 (2005) 1298–1304.
[404] P. Bordes, E. Pollet, L. Averous, Prog. Polym. Sci. 34 (2009) 125–155.
[405] P. Kanmani, J.-W. Rhim, Food Hydrocoll. 35 (2014) 644–652.
[406] V.K. Thakur, M.R. Kessler, Polymer 69 (2015) 369–383.
[407] H. Heinz, U.W. Suter, J. Phys. Chem. B 108 (2004) 18341–18352.
[408] D.L. Bish, Clays Clay Miner. 41 (1993) 738–744.
[409] D.A. Sverjensky, N. Sahai, Geochim. Cosmochim. Acta 60 (1996) 3773–3797.
[410] L.O. Benetoli, C.M. de Souza, K.L. da Silva, I.G. de Souza Jr., H. de Santana, A. Paesano Jr, A.C. da Costa, C.T. Zaia, D.A. Zaia, Orig. Life Evol. Biosph. 37 (2007) 479–493.
[411] P. Yuan, P.D. Southon, Z. Liu, M.E.R. Green, J.M. Hook, S.J. Antill, C.J. Kepert, J. Phys. Chem. C 112 (2008) 15742–15751.
[412] M. Liu, Z. Jia, D. Jia, C. Zhou, Prog. Polym. Sci. 39 (2014) 1498–1525.
[413] B.K.G. Theng, Clays Clay Miner. 30 (1982) 1–10.
[414] M.A. Osman, M. Ernst, B.H. Meier, U.W. Suter, J. Phys. Chem. B 106 (2002) 653–662.
[415] M.A. Osman, J. Colloid Interface Sci. 214 (1999) 400–406.
[416] Y.T. Fu, H. Heinz, Philos. Mag. 90 (2010) 2415–2424.
[417] H. Heinz, R.A. Vaia, B.L. Farmer, J. Chem. Phys. 124 (2006) 224713.
[418] Y.T. Fu, H. Heinz, Chem. Mater. 22 (2010) 1595–1605.
[419] G.R. Gao, G.L. Du, Y.J. Cheng, J. Fu, J. Mater. Chem. B 2 (2014) 1539–1548.
[420] C. Yao, Z. Liu, C. Yang, W. Wang, X.J. Ju, R. Xie, L.Y. Chu, Adv. Funct. Mater. 25 (2015) 2980–2991.
[421] F. Cousin, V. Cabuil, P. Levitz, Langmuir 18 (2002) 1466–1473.
[422] F. Cavani, F. Trifiro, A. Vaccari, Catal. Today 11 (1991) 173–301.
[423] H. Chen, L. Hu, M. Chen, Y. Yan, L. Wu, Adv. Funct. Mater. 24 (2014) 934–942.
[424] G. Fan, F. Li, D.G. Evans, X. Duan, Chem. Soc. Rev. 43 (2014) 7040–7066.
[425] F. Song, X. Hu, Nat. Commun. 5 (2014) 4477.
[426] F. Song, X. Hu, J. Am. Chem. Soc. 136 (2014) 16481–16484.
[427] P.P. Kumar, A.G. Kalinichev, R.J. Kirkpatrick, J. Phys. Chem. C 111 (2007) 13517–13523.
[428] A.G. Kalinichev, P.P. Kumar, R.J. Kirkpatrick, Philos. Mag. 90 (2010) 2475–2488.
[429] V. Rives, M. del Arco, C. Martin, Appl. Clay Sci. 88–89 (2014) 239–269.
[430] S. Aisawa, N. Higashiyama, S. Takahashi, H. Hirahara, D. Ikematsu, I. Kondo, H. Nakayama, E. Narita, Appl. Clay Sci. 35 (2007) 146–154.
[431] Z. Hu, G. Chen, Adv. Mater. 26 (2014) 5950–5956.
[432] T. Subramanian, A. Dhakshinamoorthy, K. Pitchumani, Tetrahedron Lett. 54 (2013) 7167–7170.
[433] F. Bonaccorso, L. Colombo, G. Yu, M. Stoller, V. Tozzini, A.C. Ferrari, R.S. Ruoff, V. Pellegrini, Science 347 (2015).
[434] J. Liu, Y. Liu, N. Liu, Y. Han, X. Zhang, H. Huang, Y. Lifshitz, S.-T. Lee, J. Zhong, Z. Kang, Science 347 (2015) 970–974.
[435] Science and Technology of Concrete Admixtures, Woodhead Publishing, Amsterdam, 2015.
[436] H.F.W. Taylor, Cement Chemistry, Academic Press, London, 1997.
[437] A. Nonat, Cem. Concr. Res. 34 (2004) 1521–1528.
[438] E. Gartner, Potential Improv. Cem. Sustain. (2011) 1–13.
[439] J.J. Thomas, H.M. Jennings, A.J. Allen, Concr. Sci. Eng. 1 (1999) 45–64.
[440] A.J. Allen, J.J. Thomas, H.M. Jennings, Nat. Mater. 6 (2007) 311–316.
[441] P.A. Bonnaud, C. Labbez, R. Miura, A. Suzuki, N. Miyamoto, N. Hatakeyama, A. Miyamoto, K.J. Van Vliet, Nanoscale 8 (2016) 4160–4172.
[442] E. Masoero, E. Del Gado, R.J.M. Pellenq, F.J. Ulm, S. Yip, Phys. Rev. Lett. 109 (2012) 155503.
[443] L.B. Skinner, S.R. Chae, C.J. Benmore, H.R. Wenk, P.J.M. Monteiro, Phys. Rev. Lett. 104 (2010) 195502.
[444] I.G. Richardson, Cem. Concr. Res. 38 (2008) 137–158.
[445] R.J. Pellenq, A. Kushima, R. Shahsavari, K.J. Van Vliet, M.J. Buehler, S. Yip, F.J. Ulm, Proc. Natl. Acad. Sci. USA 106 (2009) 16102–16107.
[446] D.A. Kulik, Cem. Concr. Res. 41 (2011) 477–495.
[447] B. Lothenbach, A. Nonat, Cem. Concr. Res. 78 (2015) 57–70.
[448] K. Ioannidou, K.J. Krakowiak, M. Bauchy, C.G. Hoover, E. Masoero, S. Yip, F.J. Ulm, P. Levitz, R.J.M. Pellenq, E. Del Gado, Proc. Natl. Acad. Sci. USA 113 (2016) 2029–2034.
[449] R. Nadiv, M. Shtein, A. Peled, O. Regev, Constr. Build. Mater. 98 (2015) 112–118.
[450] D. Marchon, Controlling Cement Hydration Through the Molecular Structure of Comb Copolymer Superplasticizers (Ph.D. thesis), ETH Zürich, Zurich, Switzerland, 2016.
[451] N. Jongen, P. Bowen, J. Lemaitre, J.C. Valmalette, H. Hofmann, J. Colloid Interface Sci. 226 (2000) 189–198.
[452] L.C. Soare, P. Bowen, J. Lemaitre, H. Hofmann, J. Phys. Chem. B 110 (2006) 17763–17771.

[453] F. Ridi, E. Fratini, P. Luciani, F. Winnefeld, P. Baglioni, J. Phys. Chem. C 116 (2012) 10887–10895.
[454] E. Cappelletto, S. Borsacchi, M. Geppi, F. Ridi, E. Fratini, P. Baglioni, J. Phys. Chem. C 117 (2013) 22947–22953.
[455] N. Tenoutasse, The Hydratation Mechanism of C3A and C3S in the Presence of Calcium Chloride and Calcium Sulphate, Centre National de Recherches Scientifiques et Techniques pour l'Industrie Cimetiere, France, 1969.
[456] J. Plank, Z. Dai, P.R. Andres, Mater. Lett. 60 (2006) 3614–3617.
[457] A. Habbaba, Z. Dai, J. Plank, Cem. Concr. Res. 59 (2014) 112–117.
[458] R.J. Flatt, Y.F. Houst, Cem. Concr. Res. 31 (2001) 1169–1176.
[459] J. Plank, D. Zhimin, H. Keller, F. von Hossle, W. Seidl, Cem. Concr. Res. 40 (2010) 45–57.
[460] C. Giraudeau, J.B.D. de Lacaillerie, Z. Souguir, A. Nonat, R.J. Flatt, J. Am. Ceram. Soc. 92 (2009) 2471–2488.
[461] J. Cheung, A. Jeknavorian, L. Roberts, D. Silva, Cem. Concr. Res. 41 (2011) 1289–1309.
[462] D. Marchon, P. Juilland, E. Gallucci, L. Frunz, R.J. Flatt, J. Am. Ceram. Soc. (2017), accepted.
[463] D. Marchon, U. Sulser, A. Eberhardt, R.J. Flatt, Soft Matter 9 (2013) 10719–10728.
[464] A.M. Kjeldsen, R.J. Flatt, L. Bergstrom, Cem. Concr. Res. 36 (2006) 1231–1239.
[465] R.K. Mishra, D. Geissbuhler, H.A. Carmona, F.K. Wittel, M.L. Sawley, M. Weibel, E. Gallucci, H.J. Herrmann, H. Heinz, R.J. Flatt, Adv. Appl. Ceram. 114 (2015) 393–401.
[466] M. Weibel, R.K. Mishra, ZKG Int. 67 (2014) 28–39.
[467] R.K. Mishra, L. Fernández-Carrasco, R.J. Flatt, H. Heinz, Dalton Trans. 43 (2014) 10602–10616.
[468] R.K. Mishra, R.J. Flatt, H. Heinz, J. Phys. Chem. C 117 (2013) 10417–10432.
[469] A.M. Bano, P.M. Rodger, D. Quigley, Langmuir 30 (2014) 7513–7521.
[470] Q. Hu, et al., Faraday Discuss. 159 (2012) 509–523.
[471] S.B. Schrier, M.K. Sayeg, J.J. Gray, Langmuir 27 (2011) 11520–11527.
[472] D. Quigley, P.M. Rodger, C.L. Freeman, J.H. Harding, D.M. Duffy, J. Chem. Phys. 131 (2009) 094703.
[473] C.L. Freeman, I. Asteriadis, M. Yang, J.H. Harding, J. Phys. Chem. C 113 (2009) 3666–3673.
[474] T.Z. Lin, H. Heinz, J. Phys. Chem. C 120 (2016) 4975–4992.
[475] F.S. Utku, E. Seckin, G. Goller, C. Tamerler, M. Urgen, Appl. Surf. Sci. 350 (2015) 62–68.
[476] R.W. Friddle, K. Battle, V. Trubetskoy, J. Tao, E.A. Salter, J. Moradian-Oldak, J.J. De Yoreo, A. Wierzbicki, Angew. Chem. Int. Ed. 50 (2011) 7541–7545.
[477] M.C. Weiger, J.J. Park, M.D. Roy, C.M. Stafford, A. Karim, M.L. Becker, Biomaterials 31 (2010) 2955–2963.
[478] S.V. Dorozhkin, Acta Biomater. 6 (2010) 715–734.
[479] A. Dey, P.H.H. Bomans, F.A. Muller, J. Will, P.M. Frederik, G. de With, N. Sommerdijk, Nat. Mater. 9 (2010) 1010–1014.
[480] K. Teshima, S. Lee, M. Sakurai, Y. Kameno, K. Yubuta, T. Suzuki, T. Shishido, M. Endo, S. Oishi, Cryst. Growth Des. 9 (2009) 2937–2940.
[481] M.D. Roy, S.K. Stanley, E.J. Amis, M.L. Becker, Adv. Mater. 20 (2008) 1830–1836.
[482] I.S. Harding, N. Rashid, K.A. Hing, Biomaterials 26 (2005) 6818–6826.
[483] C. Du, G. Falini, S. Fermani, C. Abbott, J. Moradian-Oldak, Science 307 (2005) 1450–1454.
[484] R.Z. Legeros, O.R. Trautz, J.P. Legeros, E. Klein, W.P. Shirra, Science 155 (1967) 1409–1411.
[485] M.I. Kay, R.A. Young, A.S. Posner, Nature 204 (1964) 1050–1052.
[486] K. Lindorff-Larsen, S. Piana, R.O. Dror, D.E. Shaw, Science 334 (2011) 517–520.
[487] T. Ishikawa, M. Wakamura, S. Kondo, Langmuir 5 (1989) 140–144.
[488] H. Tanaka, M. Chikazawa, K. Kandori, T. Ishikawa, Phys. Chem. Chem. Phys. 2 (2000) 2647–2650.
[489] S. Il Kim, et al., Science 348 (2015) 109–114.
[490] R.D. Mullins, Surf. Sci. Rep. 70 (2015) 42–85.
[491] H. Dong, S.-R. Du, X.-Y. Zheng, G.-M. Lyu, L.-D. Sun, L.-D. Li, P.-Z. Zhang, C. Zhang, C.-H. Yan, Chem. Rev. 115 (2015) 10725–10815.
[492] D. Dupont, K. Binnemans, Green Chem. 17 (2015) 2150–2163.
[493] Y. Freeman, G.F. Alapatt, W.R. Harrell, P. Lessner, J. Electrochem. Soc. 159 (2012) A1646–A1651.
[494] S. Łukasiewicz, K. Szczepanowicz, E. Błasiak, M. Dziedzicka-Wasylewska, Langmuir 31 (2015) 6415–6425.
[495] E. Lepeltier, C. Bourgaux, P. Couvreur, Adv. Drug Deliv. Rev. 71 (2014) 86–97.
[496] J. Wackerlig, P.A. Lieberzeit, Sens. Actuators B-Chem. 207 (2015) 144–157.
[497] M.P. Robin, R.K. O'Reilly, Polym. Int. 64 (2015) 174–182.
[498] K. Li, B. Liu, Chem. Soc. Rev. 43 (2014) 6570–6597.
[499] T. Szabo, J. Mihaly, I. Sajo, J. Telegdi, L. Nyikos, Prog. Org. Coat. 77 (2014) 1226–1232.
[500] A. Hofland, Prog. Org. Coat. 73 (2012) 274–282.
[501] F. Canfarotta, M.J. Whitcombe, S.A. Piletsky, Biotechnol. Adv. 31 (2013) 1585–1599.
[502] D. Bei, J.N. Meng, B.B.C. Youan, Nanomedicine 5 (2010) 1385–1399.
[503] J. Liu, Y. Xiao, C. Allen, J. Pharm. Sci. 93 (2004) 132–143.
[504] S. Acharya, S.K. Sahoo, Adv. Drug Deliv. Rev. 63 (2011) 170–183.
[505] G. Gyulai, C.B. Pénzes, M. Mohai, F. Csempesz, É. Kiss, Eur. Polym. J. 49 (2013) 2495–2503.
[506] J.-C. Olivier, NeuroRx 2 (2005) 108–119.
[507] S.M. Moghimi, S.S. Davis, Crit. Rev. Ther. Drug Carr. Syst. 11 (1994) 31–59.
[508] P. Decuzzi, R. Pasqualini, W. Arap, M. Ferrari, Pharm. Res. 26 (2008) 235–243.
[509] S.M. Moghimi, C.J.H. Porter, I.S. Muir, L. Illum, S.S. Davis, Biochem. Biophys. Res. Commun. 177 (1991) 861–866.
[510] H. Soo Choi, W. Liu, P. Misra, E. Tanaka, J.P. Zimmer, B. Itty Ipe, M.G. Bawendi, J.V. Frangioni, Nat. Biotechnol. 25 (2007) 1165–1170.
[511] W. Jiang, B.Y. Kim, J.T. Rutka, W.C. Chan, Nat. Nanotechnol. 3 (2008) 145–150.
[512] J. Wang, J.D. Byrne, M.E. Napier, J.M. DeSimone, Small 7 (2011) 1919–1931.
[513] J.A. Champion, Y.K. Katare, S. Mitragotri, Proc. Natl. Acad. Sci. USA 104 (2007) 11901–11904.
[514] S.E.A. Gratton, P.A. Ropp, P.D. Pohlhaus, J.C. Luft, V.J. Madden, M.E. Napier, J.M. DeSimone, Proc. Natl. Acad. Sci. USA 105 (2008) 11613–11618.
[515] P. Decuzzi, M. Ferrari, Biophys. J 94 (2008) 3790–3797.
[516] D.E. Owens, N.A. Peppas, Int. J. Pharm. 307 (2006) 93–102.
[517] K.S. Soppimath, T.M. Aminabhavi, A.R. Kulkarni, W.E. Rudzinski, J. Control. Release 70 (2001) 1–20.
[518] T.M. Allen, A. Chonn, FEBS Lett. 223 (1987) 42–46.
[519] T.M. Allen, Adv. Drug Deliv. Rev. 13 (1994) 285–309.
[520] N. Kamaly, Z.Y. Xiao, P.M. Valencia, A.F. Radovic-Moreno, O.C. Farokhzad, Chem. Soc. Rev. 41 (2012) 2971–3010.
[521] R. Gref, A. Domb, P. Quellec, T. Blunk, R.H. Müller, J.M. Verbavatz, R. Langer, Adv. Drug Deliv. Rev. 16 (1995) 215–233.
[522] R. Gref, Y. Minamitake, M. Peracchia, V. Trubetskoy, V. Torchilin, R. Langer, Science 263 (1994) 1600–1603.
[523] J.P. Rao, K.E. Geckeler, Prog. Polym. Sci. 36 (2011) 887–913.
[524] H. Fessi, F. Puisieux, J.P. Devissaguet, N. Ammoury, S. Benita, Int. J. Pharm. 55 (1989) R1–R4.
[525] F. Gu, L. Zhang, B.A. Teply, N. Mann, A. Wang, A.F. Radovic-Moreno, R. Langer, O.C. Farokhzad, Proc. Natl. Acad. Sci. USA 105 (2008) 2586–2591.
[526] P.M. Valencia, M.H. Hanewich-Hollatz, W. Gao, F. Karim, R. Langer, R. Karnik, O.C. Farokhzad, Biomaterials 32 (2011) 6226–6233.
[527] Z.Q. Cao, Q.M. Yu, H. Xue, G. Cheng, S.Y. Jiang, Angew. Chem. Int. Ed. 49 (2010) 3771–3776.
[528] Z.G. Estephan, J.A. Jaber, J.B. Schlenoff, Langmuir 26 (2010) 16884–16889.
[529] J. Ladd, Z. Zhang, S. Chen, J.C. Hower, S. Jiang, Biomacromolecules 9 (2008) 1357–1361.
[530] S. Chen, J. Zheng, L. Li, S. Jiang, J. Am. Chem. Soc. 127 (2005) 14473–14478.
[531] Y. He, J. Hower, S. Chen, M.T. Bernards, Y. Chang, S. Jiang, Langmuir 24 (2008) 10358–10364.
[532] Q. Shao, S. Jiang, Adv. Mater. 27 (2015) 15–26.
[533] R.G. Chaudhuri, S. Paria, Chem. Rev. 112 (2012) 2373–2433.
[534] Y. Liu, T. Pauloehrl, S.I. Presolski, L. Albertazzi, A.R.A. Palmans, E.W. Meijer, J. Am. Chem. Soc. 137 (2015) 13096–13105.
[535] Q. Liu, Z. Sun, Y. Dou, J.H. Kim, S.X. Dou, J. Mater. Chem. A 3 (2015) 11688–11699.
[536] S. Salmaso, P. Caliceti, J. Drug Deliv. 2013 (2013) 374252.
[537] N. Voigt, P. Henrich-Noack, S. Kockentiedt, W. Hintz, J. Tomas, B.A. Sabel, Eur. J. Pharm. Biopharm. 87 (2014) 19–29.
[538] J. Deng, B. Chen, X. Luo, W. Yang, Macromolecules 42 (2009) 933–938.
[539] J. Pecher, S. Mecking, Chem. Rev. 110 (2010) 6260–6279.
[540] B. Yao, G. Wang, J. Ye, X. Li, Mater. Lett. 62 (2008) 1775–1778.
[541] N. Gospodinova, L. Terlemezyan, Prog. Polym. Sci. 23 (1998) 1443–1484.
[542] R.B. Kaner, A.G. Macdiarmid, Sci. Am. 258 (1988) 106.
[543] P. Chandrasekhar, Conducting Polymers, Fundamentals and Applications: a Practical Approach, Kluwer Academic Publishers, London, 1999.
[544] J. Stejskal, M. Spirkova, A. Riede, M. Helmstedt, P. Mokreva, J. Prokes, Polymer 40 (1999) 2487–2492.
[545] S. Dorey, C. Vasilev, L. Vidal, C. Labbe, N. Gospodinova, Polymer 46 (2005) 1309–1315.
[546] J. Jang, J. Ha, S. Kim, Macromol. Res. 15 (2007) 154–159.
[547] J. Jang, J. Ha, J. Cho, Adv. Mater. 19 (2007) 1772–1775.